

HARVARD UNIVERSITY
Graduate School of Arts and Sciences



DISSERTATION ACCEPTANCE CERTIFICATE

The undersigned, appointed by the
Department of Physics
have examined a dissertation entitled

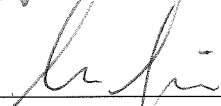
Small Diatomic Alkali Molecules at Ultracold Temperatures

presented by Tout Taotao Wang

candidate for the degree of Doctor of Philosophy and hereby
certify that it is worthy of acceptance.

Signature  _____

Typed name: Professor John Doyle, Chair

Signature  _____

Typed name: Professor Markus Greiner

Signature  _____

Typed name: Professor Wolfgang Ketterle

Signature  _____

Typed name: Professor Susanne Yelin

Date: October 17, 2014

Small Diatomic Alkali Molecules at Ultracold Temperatures

A dissertation presented
by

TOUT TAOTAO WANG

to

The Department of Physics

in partial fulfillment of the requirements
for the degree of

Doctor of Philosophy
in the subject of
Physics

Harvard University
Cambridge, Massachusetts

October 2014

© 2014 - Tout Taotao Wang
All rights reserved.

Small Diatomic Alkali Molecules at Ultracold Temperatures

ABSTRACT

This dissertation describes experimental work done with two of the smallest diatomic alkali molecules, ${}^6\text{Li}_2$ and ${}^{23}\text{Na}{}^6\text{Li}$, each formed out of its constituent atoms at ultracold temperatures. The ${}^{23}\text{Na}{}^6\text{Li}$ molecule was formed for the first time at ultracold temperatures, after previous attempts failed due to an incorrect assignment of Feshbach resonances in the ${}^6\text{Li}+{}^{23}\text{Na}$ system. The experiment represents successful molecule formation around the most difficult Feshbach resonance ever used, and opens up the possibility of transferring NaLi to its spin-triplet ground state, which has both magnetic and electric dipole moments and is expected to be long-lived. For ${}^6\text{Li}_2$, the experimental efforts in this thesis have solved a long-standing puzzle of apparently long lifetimes of closed-channel fermion pairs around a narrow Feshbach resonance, finding that the lifetime is in fact short, as expected in the absence of Pauli suppression of collisions. Moreover, measurements of collisions of Li_2 with free Li atoms demonstrates a striking first example of collisions involving molecules at ultracold temperatures described by physics beyond universal long-range van der Waals interactions.

Table of Contents

Abstract	iii
Acknowledgements	ix
1 Introduction	1
2 Essentials of Diatomic Molecules	3
2.1 Long-Range van der Waals Interactions	4
2.2 Full Molecular Potentials	8
2.3 Vibrations and Rotations	11
2.4 Angular Momentum Quantum Numbers Λ , Σ , and Ω	13
2.5 Inversion Symmetries $+/-$ and g/u	16
2.6 Electric Dipole Moment	20
2.7 Electric Dipole Selection Rules	23
2.8 Spin-Orbit Coupling	26
3 Feshbach Resonances and Molecule Formation	28
3.1 Scattering at Ultracold Temperatures	29
3.2 The Radial Square Well Potential and Scattering Resonances	31
3.3 Feshbach Resonances	35
3.4 The Asymptotic Bound-State Model	39
3.5 Molecule Formation around a Feshbach Resonance	42
3.6 The BEC-BCS Crossover	46

4	Formation of $^{23}\text{Na}^6\text{Li}$ Molecules	48
4.1	Revised Assignment of Feshbach Resonances	48
4.2	Experimental Machinery	52
4.3	Molecule Formation	53
4.4	Optimizing Decay Lifetime	57
5	Molecules of $^6\text{Li}_2$ Around a Narrow Feshbach Resonance	59
5.1	A Long-Standing Puzzle in ^6Li	59
5.2	Molecule Formation Around the 543 G Narrow Resonance	61
5.3	Collisions of $^6\text{Li}_2$ with Li and Na atoms	64
5.4	The Quantum Langevin Model for Collisional Loss	66
5.5	Quantum Depletion and Deviation from Universality	69
6	Future Directions	71
6.1	A Long-Lived $^{23}\text{Na}^6\text{Li}$ Spin-Triplet Ground State	71
6.2	Photoassociation Spectroscopy of $^{23}\text{Na}^6\text{Li}$	73
6.3	New Possibilities with Triplet Ground-State Molecules	79
A	Asymptotic Bound State Model	81
B	Temperature and Density Measurements	88
C	The Breit-Rabi Formula	91
	References	96

List of Figures

2.1	Van der Waals interactions between atom pairs	5
2.2	Two-atom energy levels coupled by the van der Waals interaction	7
2.3	The Lennard-Jones potential	9
2.4	Lowest ten electronic potentials of the NaLi molecule	10
2.5	Vibrations and rotations of a diatomic molecule	12
2.6	Hund's cases for electron angular momentum coupling to the molecular axis	14
2.7	Molecular potential curves for Li ₂	19
2.8	Dipole-dipole interactions between a pair of heteronuclear molecules	21
3.1	Scattering from a spherically symmetric potential	30
3.2	Scattering from a radial square well	32
3.3	Resonant enhancement of scattering length in a radial square well	33
3.4	Two-channel coupling model for a Feshbach resonance	35
3.5	Scattering length enhancement and bound-state behaviour	38
3.6	Open vs. closed-channel dominated Feshbach resonances	39
3.7	Asymptotic bound-state model for Feshbach resonances	41
3.8	Two-level Landau-Zener crossing	43
3.9	The BEC-BCS crossover in an ultracold gas of fermions	47
4.1	Revised assignment of ⁶ Li+ ²³ Na Feshbach resonances	50
4.2	Determination of Feshbach resonance location	54
4.3	Experimental sequence for molecule formation	55

4.4	Absorption imaging of molecular clouds using dissociated Na and Li atoms	55
4.5	Separation of atoms and molecules in a magnetic field gradient	56
4.6	Lifetime of trapped NaLi molecules	58
5.1	Feshbach resonances in ${}^6\text{Li}_2$	60
5.2	Experimental sequence for ${}^6\text{Li}_2$ molecule formation	62
5.3	Absorption images of ${}^6\text{Li}_2$ molecules	63
5.4	Lifetime of a pure sample of ${}^6\text{Li}_2$ molecules	64
5.5	Lifetime of Li_2 in the presence of free atoms	65
5.6	Quantum Langevin model for collisions involving ultracold molecules	67
5.7	Quantum depletion of vibrational decay in molecules	70
6.1	Spin-triplet and singlet ground states of NaLi	72
6.2	Stimulated Raman adiabatic passage for molecular state transfer	74
B.1	Temperature measurement of a ${}^6\text{Li}$ cloud	89

List of Tables

2.1	C_6 coefficients and near-dissociation bound-state spacings	6
2.2	Key properties of various heteronuclear diatomic alkali molecules	23
3.1	Landau-Zener parameters from various molecule formation experiments . .	45
5.1	Two-body decay coefficients for Li_2 with different collision partners	67

Acknowledgments

Someone once said, “There is no better place to spend your twenties than still in school.” I can confirm that this has indeed been true of my graduate school years, and there are many individuals to whom I am grateful for making things so. Foremost on the list is Wolfgang Ketterle, whose infectious enthusiasm about science, gift for distilling complex concepts down to simple explanations, and endless patience with his students make him a rare breed of research mentor indeed. At times he prefaces the aforementioned explanations by saying, “Let me explain this to you in a way you will never forget.” I expect that, having had the privilege of doing research alongside Wolfgang, that there will be elements from the physics of ultracold atoms that I will remember for the rest of my life. I will also cherish the experience of pacing him for the first nine miles of a sub-eighty-minute half marathon, before fading and finishing over a minute slower than his time.

It takes the endorsement of several faculty members to complete a dissertation, and I am grateful to my committee members John Doyle, Susanne Yelin and Markus Greiner for serving in their respective capacities. John, in addition to being a leading expert on everything having to do with cold molecules, was also my academic advisor, meaning that my progress through graduate school was directly related to his willingness to sign various pieces of paper. Susanne is one of the most cheerful physicists I know, and moreover was responsible for coordinating the grant that supported most of the work in this dissertation. Markus, meanwhile, is someone who leaves you with a dozen different ideas for how to upgrade your machinery each time you have an extended conversation with him. Research at an institution of higher learning also cannot happen without the support of administrators,

and in my time at the Center for Ultracold Atoms I have received a great deal of assistance from Joanna Keseberg, David Fitzgerald, Paula Sack, and Jan Ragusa in areas ranging from bizarre travel reimbursement requests to ordering something other than sandwiches for student lunch seminars. In addition, Lisa Cacciabauda has been a source of encouragement in the last months of completing this dissertation, and typifies the department’s genuine commitment to the well-being of its graduate students.

Although in principle I could have completed all of my research work alone, in practice it was simply easier to have someone else shout: “Back,” “Keep going,” or “Next axis” across the room while I adjusted the knobs on some mirror mount. In this regard, Myoung-Sun Heo was a critical knob-tweaking partner for all of my most fruitful months of research in graduate school. I will always be amazed at his capacity to do a full day of research work, go home to dinner with his wife and two beautiful daughters, and then return to the laboratory again for more! Without his diligence and persevering attitude, the two main scientific accomplishments of this dissertation would not have been possible. Timur Rvachov has a healthy desire to challenge the status quo and ask hard questions, which are valuable traits for a younger graduate student to have. Timur has become the resident expert on our Cicero computer control system, and in addition led the charge to rebuild a large part of our atom cooling hardware. I am happy to be leaving the laboratory in the hands of a superior experimentalist. Dylan Cotta joined our team as the first Masters student under my watch, and set a high bar for all such students to follow—most notably providing a timely suggestion that we try to obtain our first molecule signal via a radio-frequency spin-flip to exclude free atoms from the image. Pascal Notz more than met the high standard that Dylan set, making impressive contributions during a difficult stretch of experiment repair. Colin Kennedy spent only a brief stint with us before trading the challenge of making real molecules for the allure of generating artificial magnetic fields in the next building over, but even in that short time, his eagerness and future potential were apparent. I specifically acknowledge Timur, Colin, and Dylan for an unforgettable trip to a certain dancing establishment inn Anaheim during the 2012 DAMOP meeting.

It took three full years before I absorbed enough knowledge from the more experienced members of the team to take complete charge of the experimental work. In that time, I learned from Gyu-boong Jo how to climb into awkward positions to do vacuum repairs, from Jae-Hoon Choi how to sufficiently tighten screws, from Ye-ryoung Lee how to give our diode lasers the magic touch, from Tony Kim how to build electronics to meet the sometimes unusual needs of our laboratory, and from Caleb Christensen how growing up working in the family hardware store is sometimes more important for doing research in experimental physics than anything in the standard curriculum. To Caleb I owe a particular debt for his heroic but ultimately unsuccessful first efforts towards molecule formation. Several younger students have suffered through my Socratic method of explaining physics over the years. For their perseverance, I thank Chenchen Luo, Derek Kita, Yijun Jiang, Li Jing and Gregory Lau. Alan Jamison was persuaded enough by the promise of ultracold molecules to join us as the new postdoctoral fellow. I wish him all the best for the coming months and years. I have often joked that one can probably find every item in the Thorlabs catalogue somewhere within the Center for Ultracold Atoms. In this and other ways, the collective presence of the groups at Harvard and MIT is a real asset to atomic physics research, and I am grateful for the friends in the various groups who have given away optics or lent out expensive equipment over the years.

Several chance encounters with senior researchers ended up leading to the breakthroughs described in this dissertation. An extended discussion with Jook Walraven at the Les Houches Summer School left me understanding the details of Feshbach resonances and how to form molecules around extraordinarily narrow ones. Tobias Tiecke moved to Harvard at just the right time for me to bombard him with questions about his Asymptotic Bound State Model. Paul Julienne graciously sat down with me one day at lunch at a DAMOP meeting and spent the next hour explaining to me a great deal about ultracold collisions. Goulven Quéméner astonished all of us when we reached out to him about our observed deviation from universality, by replying that he had already written a paper explaining what we had found.

Having spent my undergraduate years at the University of Toronto, it was great to have other alumni within the physics community at Harvard and MIT. Arghavan Safavi and Michael Yee, in particular, have been dear friends over the years. Joseph Thywissen at the University of Toronto offered me the first chance to do experimental work in an ultracold atoms laboratory. He has been a generous source of insight at DAMOP meetings in the years since, including when he took a group of us out to dinner in Québec City. My path towards a doctorate in physics started long before I entered university, and for giving me the initial spark to pursue physics I thank Vida Ghaem-Maghani from Don Mills Collegiate Institute.

In addition to publishing two journal papers during graduate school, I also had the chance to participate in the creation of two entertaining videos about my research work. I am grateful to Tom Levenson and the team from the MIT Science Writing Program, as well as Eric Ruleman and his team of expert filmmakers, for helping me tell the story of this dissertation on film.

Graduate school life is more than just turning knobs and aligning lasers, and Harvard in particular places an important emphasis on fostering a flourishing sense of community among its graduate students. I spent two memorable years as a member of the Graduate School of Arts and Sciences Resident Advisor team, and also relished being part of the Dudley House community—everything from attending Senior Common Room dinners to getting a pair of top five finishes in the Charles River Run to score major points for Dudley during its Straus Cup-winning season of 2013-2014. The Harvard Graduate Christian Community was an anchor for my life on campus for more than six years, and there I was reminded that “worship and scholarship are not just two ships passing in the night.” In Hope Fellowship Church, I found a home where the Gospel was preached with an authentic sense of gladness, and where there existed a real, sacrificial commitment to serving those in need. Training with Cambridge Running Club instilled in me a masochistic enjoyment of half-mile repeats. The mighty men of 21 Mellen kept me honest about all my bad habits and were ideal companions for hiking adventures on both coasts.

The most important part of graduate school is perhaps figuring out what to do afterwards. I thank Graeme Malcolm, John Nicholls, and Nils Hempler at M Squared Lasers for the chance to join an impressive small company that is at the very cutting edge of photonics and quantum technologies. David Kemp, the Boston-based sales representative for M Squared, facilitated the key introductions that resulted in me accepting a position that was never publicized, and that I never formally applied for. In the research world, people tend to treat sales representatives with everything ranging from apathy to contempt. Perhaps my experience discovering an exciting opportunity at M Squared through Dave will highlight the value of really engaging with people on the sales end of things.

My parents, Xiaoyong Tao and Chunying Wang, were the first investors in the enterprise of my education, and without their insistence on the value of advanced schooling, I might never have had the chance to consider doing doctoral work. While at Harvard I have also been generously supported by a Postgraduate Scholarship from the Natural Sciences and Engineering Research Council of Canada.

I will end by noting that my biggest discovery during graduate school is not described anywhere else in this dissertation. This discovery is not any fragment of scientific understanding, but a person. I am grateful for all the ways that Karlen Ruleman has become part of my life.

Chapter 1

Introduction

The preparation and control of atoms at temperatures millions of times colder than that of outer space has opened up numerous exciting scientific frontiers in the nearly two decades since the dawn of Bose-Einstein condensation of alkali quantum gases. Ultracold atoms trapped in optical lattices have been used to demonstrate textbook phase transitions as well as to probe novel states of matter [Bloch *et al.*, 2008]. Quantum-degenerate fermions with strong interactions realized via Feshbach resonances have turned into high temperature superfluids with transition temperatures that are sizeable fractions of the Fermi temperature [Ketterle and Zwierlein, 2008]. Synthetic gauge fields produced by off-resonant laser beams have managed to coax neutral atoms into behaving like charged particles in a magnetic field [Dalibard *et al.*, 2011]. Rydberg atoms, whose valence electrons are nearly as far away from their corresponding nuclei as possible, are becoming systems with unique potential in quantum information [Saffman *et al.*, 2010] and in many-body physics [Weimer *et al.*, 2010]. Even exotic, many-valence-electron atoms like dysprosium [Lu *et al.*, 2011] and erbium [Aikawa *et al.*, 2012] have been cooled to quantum-degenerate temperatures.

However, matter in our universe does not exist solely in the form of dilute atomic gases, but as more complex molecules. Thus, one active frontier in the growing field of ultracold quantum matter is to extend the capabilities we have with atoms to the next more complex object, diatomic molecules. The preparation of quantum-degenerate samples

of molecules will open up a range of new scientific directions [Krems *et al.*, 2009], including precision measurements, quantum computation, many-body physics with anisotropic long-range interactions, and ultracold chemistry. It is in this context that the experimental work in this dissertation has been done.

Specifically, I have worked with two of the smallest possible diatomic molecules built out of alkali atoms, ${}^6\text{Li}_2$ and ${}^{23}\text{Na}{}^6\text{Li}$. For each molecule, the outcome of the experimental work turned out to be very much related to it being composed of the smallest of alkali atoms. In the case of ${}^{23}\text{Na}{}^6\text{Li}$, Chapter 4 will describe how this molecule was finally successfully formed around perhaps the most difficult Feshbach resonance ever used for molecule formation, while Chapter 6 will try to anticipate the future scientific possibilities opened up by the creation of this new molecule. For ${}^6\text{Li}_2$, the experimental efforts described in Chapter 5 have solved a long-standing puzzle of apparently long lifetimes of closed-channel fermion pairs around a narrow Feshbach resonance, and also demonstrated a striking first example of collisions involving molecules at ultracold temperatures described by physics beyond universal long-range van der Waals interactions. However, this dissertation will first start in Chapter 2 with introducing some of the concepts essential for understanding the physics of diatomic molecules at ultracold temperatures. This will be followed in Chapter 3 by an in-depth treatment of Feshbach resonances between pairs of ultracold atoms, and how they allow almost arbitrary tuning of the strength of inter-atomic interactions as well as the adiabatic conversion of free atom pairs into bound molecules in a specific internal quantum state.

Chapter 2

Essentials of Diatomic Molecules

Molecular physics is a very old field, and our current body of knowledge about the physics of diatomic molecules traces back to work done in the earliest days of quantum theory [Demtröder, 2005]. However, to experimentalists in the field of ultracold atoms, the appearance of near-quantum-degenerate molecules on the scientific landscape is something recent [Ni *et al.*, 2008]. Thus, many of the essential concepts needed for understanding ultracold molecules are still strange to younger researchers, and moreover, molecules are just simply more complex and confusing objects to understand compared with atoms. They have, in addition to electronic transitions, rotational and vibrational level structure. Moreover, these states are labelled by dizzying combinations of quantum numbers, and selection rules for transitions between them become more elaborate.

Thankfully, one does not have to absorb all of molecular physics in order to have a working knowledge for ultracold molecules. The goal of this chapter is to explain what the essential concepts are, at a level that will be accessible to someone with a good grasp of traditional atomic physics concepts like angular momentum coupling, perturbation theory, two-level systems, etc. The chapter begins in Section 2.1 by discussing attractive van der Waals interactions between atom pairs. Section 2.2 introduces model potentials for atom pairs as well as realistic molecular potentials, and ends with the Born-Oppenheimer approximation for solving the molecular Hamiltonian. The different electronic, vibrational

and rotational states in a molecule are covered in Section 2.3, and the following two sections, 2.4 and 2.5, explain all the different angular momentum and parity quantum numbers that are important for identifying molecular states. Section 2.6 focuses on the useful property of an electric dipole moment for diatomic molecules consisting of different atoms, and Section 2.7 returns to considering molecular states by deriving selection rules for possible electric dipole transitions. The chapter ends with Section 2.8, which describes the effect of spin-orbit coupling on molecules.

2.1 Long-Range van der Waals Interactions

Even in the limit of infinite separation, there are already attractive forces between atom pairs that bring them together to form molecules. This is due to a simple theorem in quantum mechanics, which asserts that the van der Waals interaction between any two ground-state atoms is always attractive. To see why the theorem is true, one can write down the form of the dipole-dipole interaction energy between a pair of neutral atoms a and b (see for example [Griffiths, 1999], or [Jones *et al.*, 2006])

$$H_{dd} = \frac{1}{4\pi\epsilon_0} \frac{\vec{d}_a \cdot \vec{d}_b - 3(\vec{d}_a \cdot \hat{R})(\vec{d}_b \cdot \hat{R})}{R^3} \quad (2.1)$$

where ϵ_0 is the permittivity of free space, $\vec{d} = e\vec{r}$ is the dipole of each atom, and \vec{R} is the vector pointing from atom a to b (Fig. 2.1). In the semi-classical picture, neither atom a nor b has a permanent electric dipole moment, but within each atom the orbiting electrons produce a fluctuating dipole moment. The instantaneous dipole in one atom will induce a small polarization in the partner atom, and the resulting interaction between fluctuating, induced dipoles is responsible for the van der Waals interaction.

In the quantum picture, if each atom is in its ground state $|g_a g_b\rangle$, then the first order perturbation theory term for the interaction energy $E_g^{(1)} = \langle g_a g_b | H_{dd} | g_a g_b \rangle = 0$ because of the parity of \vec{d}_a and \vec{d}_b , which is the quantum way of saying that the atoms do not possess permanent electric dipole moments. The leading order interaction term is then second-order

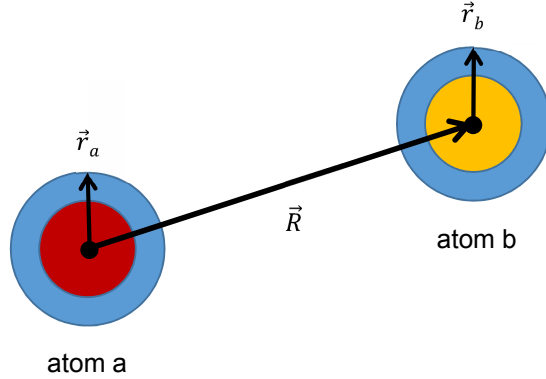


Figure 2.1: Van der Waals interactions between atom pairs arise from dipole-dipole coupling between fluctuating dipoles in each atom. \vec{r}_a and \vec{r}_b are the electron position operators for each atom centered on the corresponding nuclei. \vec{R} is the vector going from one atom to the other

in perturbation theory

$$E_g^{(2)} = \sum_{|i_a i_b\rangle \neq |g_a g_b\rangle} \frac{|\langle i_a i_b | H_{dd} | g_a g_b \rangle|^2}{E_{|g_a g_b\rangle} - E_{|i_a i_b\rangle}} \equiv -C_6/R^6 \quad (2.2)$$

where $|i_a i_b\rangle$ are all the possible states of the two-atom system. Since the denominator $E_{|g_a g_b\rangle} - E_{|i_a i_b\rangle}$ is always negative if $|g_a g_b\rangle$ is the ground state, this implies that the leading order interaction is of the van der Waals form $-C_6/R^6$. The expression for C_6 given by Eq. 2.1 and 2.2 resembles the single-atom static polarizability $\alpha = 2e^2 \sum_{m \neq n} \frac{|\langle m | z | n \rangle|^2}{(E_n - E_m)}$, reflecting how the van der Waals interaction arises from induced dipoles.

In practice, a realistic calculation of C_6 must be done numerically, accounting for not just the valence electrons but also factoring in the core electrons, as well as valence-core coupling. The latter two effects are small even in the heavier alkalis [Derevianko *et al.*, 1999], and numerical results are usually accurate at the few percent level when compared to experiments [Derevianko *et al.*, 2001]. In addition to sources giving C_6 for ground state alkalis [Derevianko *et al.*, 1999, 2001; Mitroy and Bromley, 2003], there are references for the excited states of heteronuclear alkali atom pairs [Bussery *et al.*, 1987], as well for alkaline-earth atoms [Mitroy and Bromley, 2003].

Atom Pair	C_6 (a.u.)	$E_b(2)-E_b(1)$ (GHz)
${}^6\text{Li}(2s)+{}^{23}\text{Na}(3s)$	1472	60
${}^6\text{Li}(2p)+{}^{23}\text{Na}(3s)$	17314	17
${}^{40}\text{K}(4s)+{}^{87}\text{Rb}(5s)$	4253	2.5
${}^{40}\text{K}(4s)+{}^{87}\text{Rb}(5p)$	305850	0.3

Table 2.1: Near-dissociation bound state energy spacings of different alkali atom pairs. The left-most column specifies the electronic state of each atom in the pair. C_6 coefficients are obtained from [Mitroy and Bromley, 2003] for both atoms in their electronic ground states, and from [Bussery *et al.*, 1987] for the lowest energy state with one electronic excitation. Spacings $E_b(2)-E_b(1)$ are derived from the LeRoy-Bernstein formula, assuming a zero offset ν_0 .

The C_6 coefficient determines the spacing of near-dissociation bound states of an atom pair, up to an adjustable parameter that accounts for the deviation from van der Waals behaviour at short-range. The relationship is parameterized by an analytical expression known as the LeRoy-Bernstein formula [LeRoy and Bernstein, 1970] for the binding energy

$$E_b(\nu) = (\nu + \nu_0)^3 \frac{h^3}{C_6^{1/2} \mu^{3/2}} \left(\frac{\Gamma(7/6)}{\Gamma(2/3)} \right)^3 \left(\frac{2}{\pi} \right)^{3/2} \quad (2.3)$$

where ν is an integer corresponding to the number of levels from dissociation, ν_0 is the adjustable parameter, h is Planck's constant, μ is the reduced mass of the two-atom system, and Γ is the Gamma function (a generalization of the factorial). From Eq. 2.3 it is clear that the binding energies grow rapidly with the cube of ν . Experimentally, one can determine the C_6 coefficient for an atom pair by measuring this characteristic fingerprint of near-dissociation bound states and plotting $E_b^{1/3}$ vs. ν [Ni, 2009].

Table 2.1 compares the spacing between the first two bound states of NaLi vs. RbK, assuming $\nu_0 = 0$ (potential almost deep enough to allow a new bound state at zero dissociation energy). Note that C_6 is given in Table 2.1 in atomic units. To convert to S.I. units, one should multiply by $(1 \text{ Hartree}) \times (a_0)^6 = 9.57 \times 10^{-80} \text{ J m}^6$, where a_0 is the Bohr radius and $1 \text{ Hartree} = 4.36 \times 10^{-19} \text{ J} = 27.2 \text{ eV}$.

As a general rule of thumb, C_6 gets larger for the heavier alkalis,¹ because these atoms

¹See values tabulated in [Bussery *et al.*, 1987], [Derevianko *et al.*, 1999], [Derevianko *et al.*, 2001], and

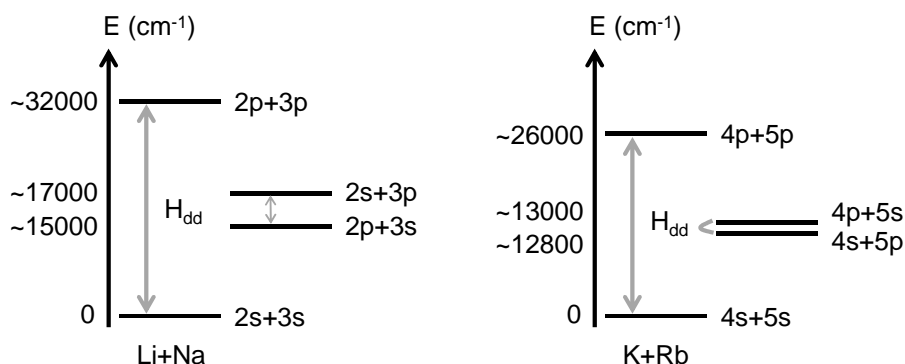


Figure 2.2: Two-atom energy levels coupled by the van der Waals interaction. The main contribution to the van der Waals interaction in the $n_a s + n_b s$ ground state comes from coupling to $n_a p + n_b p$. For $n_a p + n_b s$, the dominant coupling is to $n_a s + n_b p$, and vice versa.

are more polarizable. Their dipole matrix elements are larger, and the spacings between electronic ground and excited states tend to be smaller. Fig. 2.2 shows an example comparison between Li+Na and K+Rb, where the van der Waals interaction in the $n_a s + n_b s$ ground state comes primarily from coupling to $n_a p + n_b p$. The $\vec{d}_a \cdot \vec{d}_b$ form of H_{dd} means that it does not couple $n_a s + n_b s$ to the lower lying states $n_a p + n_b s$ or $n_a s + n_b p$. These states are instead coupled only to one another by H_{dd} .

Compared to Li+Na, K+Rb has larger dipole matrix elements $\langle n_{a(b)} s | d_{a(b)} | n_{a(b)} p \rangle$ and a smaller $n_a s + n_b s$ to $n_a p + n_b p$ energy spacing, which accounts for the larger C_6 coefficient for atoms interacting in their electronic ground states. Moreover, since the dominant contribution to the van der Waals interaction in the electronically excited $n_a p + n_b s$ state comes from coupling to $n_a s + n_a p$, and vice versa, the corresponding C_6 coefficients will be much larger, since this energy splitting is much smaller compared to the spacings between $n_a s + n_b s$ and $n_a p + n_b p$. For Li+Na the ratio of energy splittings is 15, while for K+Rb it is 130, which qualitatively explains the magnitudes of their first-excited-state C_6 coefficients compared to those of the ground state. It is also apparent from Fig. 2.2 that $n_a p + n_b s$ and $n_a s + n_b p$ will have van der Waals interactions of opposite sign. The lower-energy state will always have an attractive $-C_6/R^6$ interaction, while for the higher-energy state the interaction will be

[Mitroy and Bromley, 2003]

repulsive, because from Eq. 2.2, their energy-difference denominators have opposite signs.

Finally, it is important to note that the leading order long-range interaction may not be the van der Waals term for electronically excited states. For homonuclear (identical) atom pairs, like Li+Li or Na+Na, the leading term is in fact the first-order $1/R^3$ dipole term. This is because electronic excitations for homonuclear pairs must be (anti)symmetrized with respect to exchange of the identical nuclei, so the proper wavefunction for a state with one electronic excitation shared between two indistinguishable atoms is $|\Psi^\pm\rangle = (|g_a e_b\rangle \pm |e_a g_b\rangle)/\sqrt{2}$. Now, $\langle\Psi|H_{dd}|\Psi\rangle \neq 0$, making the first non-zero term in the perturbation expansion of H_{dd} from Eq. 2.1 a $-C_3/R^3$ dipole interaction. One consequence of this scaling is that the near-dissociation bound states of electronically excited homonuclear molecules have much larger spatial extent compared to those of the electronic ground state.

2.2 Full Molecular Potentials

At shorter atomic separations R , the long-range $1/R^6$ van der Waals potential gives way to more complex interactions. In particular, at short-range the overlapping electron clouds of the two atoms produce a strong repulsive force. The Lennard-Jones potential (Fig. 2.3) is one simplified way to qualitatively describe the full inter-atomic interaction. It takes the form

$$U_{LJ}(R) = \frac{C_{12}}{R^{12}} - \frac{C_6}{R^6} \quad (2.4)$$

where the repulsive term C_{12}/R^{12} is not physical, but is chosen for convenience of calculation [Israelachvili, 2011]. The location of the potential minimum is a simple expression $R_{min} = (2C_{12}/C_6)^{1/6}$, and similarly the potential depth is $U_{min} = -C_6^2/(4C_{12})$. For a molecular potential of the Lennard-Jones form, a measurement of the near-dissociation energy level spacing completely determines C_6 , while knowing the offset of the first bound state fixes C_{12} .

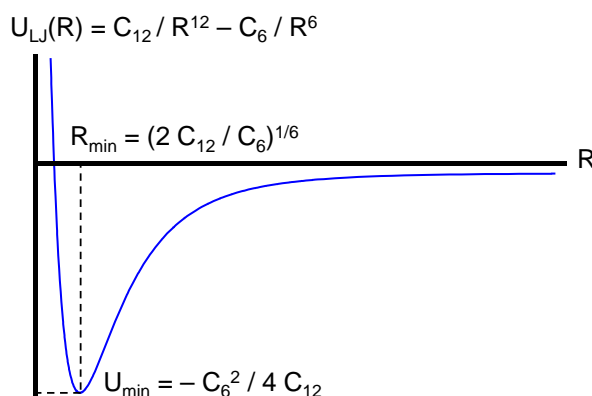


Figure 2.3: The Lennard-Jones potential is one of the simplest qualitative ways of representing interatomic interactions.

Another simple analytical potential is the Morse potential

$$U_M(R) = U_0(1 - e^{-a(R-R_0)})^2 \quad (2.5)$$

which has three parameters U_0 , a and R_0 instead of two in the case of the Lennard-Jones potential. The energy level structure of the Morse potential is especially simple, with $E(\nu) = \hbar\omega_0(\nu + 1/2) - \hbar^2\omega^2(\nu + 1/2)^2/(4U_0)$, where the effective harmonic oscillator frequency $\omega_0 = a\sqrt{2U_0/\mu}$, and μ is the reduced mass [Demtröder, 2005]. However, the Morse potential is also not physical, because in the limit $R \rightarrow \infty$, $U_M(R) \rightarrow U_0/e^{2aR}$ and not $-C_6/R^6$.

Obviously, realistic potentials for molecules have many more adjustable parameters than either the Lennard-Jones or the Morse potentials. An example of realistic potentials for NaLi are shown in Fig. 2.4. A single potential curve from such a plot can be described by more than thirty different parameters [Steinke *et al.*, 2012].

The ten potential curves in Fig. 2.4 all connect to one of three $R \rightarrow \infty$ asymptotes, corresponding to Li(2s)+Na(3s), Li(2p)+Na(3s) and Li(3s)+Na(3p), in order of increasing energy. As explained in Section 2.1, potential curves asymptotic to the first two of these separated atom states scale as $-1/R^6$ for $R \rightarrow \infty$, while curves asymptotic to the third state scale as $1/R^6$. This difference between attractive and repulsive tails of the van der

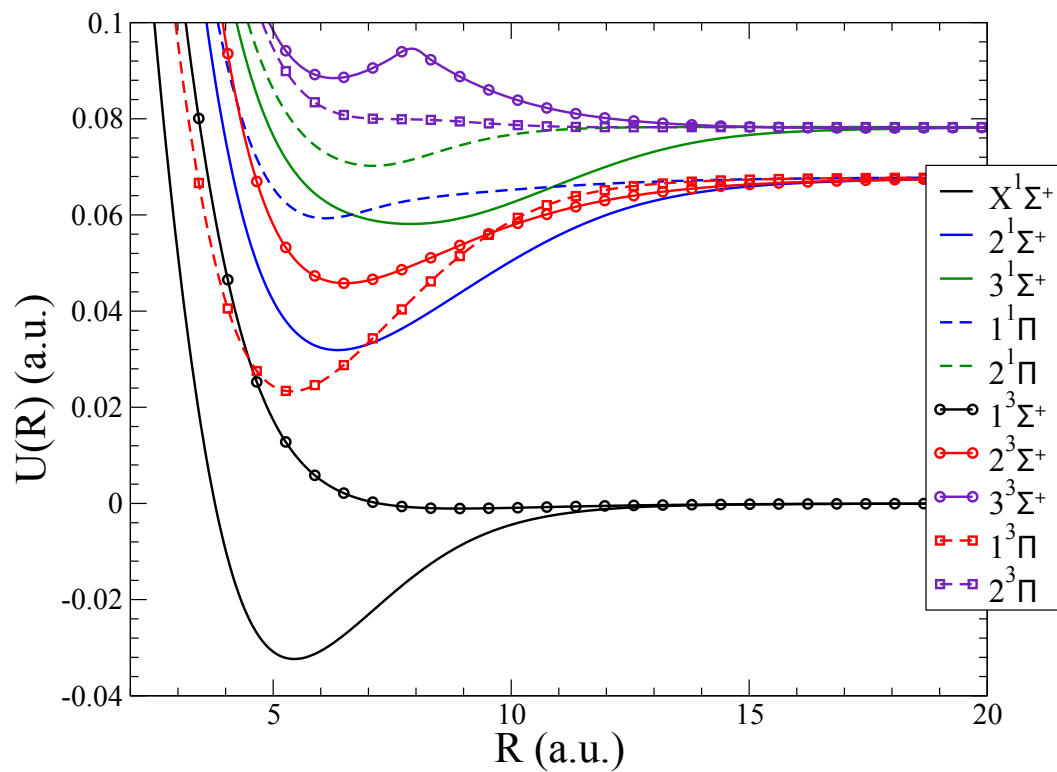


Figure 2.4: Lowest ten electronic potentials of the $^{23}\text{Na}^6\text{Li}$ molecule. The axes are in atomic units (a.u.) with R in units of $a_0 = 5.29 \times 10^{-11}$ m and E in units of Hartrees. (Courtesy of Robin Côté and collaborators)

Waals interaction is vanishing on the scale plotted in Fig. 2.4, and both can still result in bound states in the radial potential.

As the atoms approach one another, their original atomic orbitals s, p, d, etc. are no longer the eigenstates of the total Hamiltonian

$$H = \sum_j \frac{p_j^2}{2m_j} + \sum_k \frac{P_k^2}{2M_k} + V(\vec{r}, \vec{R}) \quad (2.6)$$

where the index j refers to the electrons, k refers to the nuclei, and $V(\vec{r}, \vec{R})$ is the total Coulomb interaction potential that depends on the electron and nuclei positions, $\vec{r} = \{\vec{r}_j\}$ and $\vec{R} = \{\vec{R}_k\}$ respectively, and is in general not separable. The Born-Oppenheimer approximation simplifies the solution to this Hamiltonian by assuming that, due to the more than three-orders-of-magnitude difference in mass, electronic motion is much faster than nuclear motion, meaning one can treat electronic motion with the nuclear coordinates essentially fixed. Thus, the Hamiltonian for electronic motion becomes $H_{el} = \sum_j p_j^2 / (2m_j) + V(\vec{r}, \vec{R})$, with corresponding eigenstates $|\psi_{el}(\vec{R})\rangle$ and energies $U(\vec{R})$, all of which are functions of the instantaneous positions of the nuclei $\vec{R} = \{\vec{R}_k\}$. The electronic eigenstates determine the potential $U(\vec{R})$ in which the nuclei move, and the Hamiltonian for nuclear motion becomes $H_{nuc} = \sum_k P_k^2 / (2M_k) + U(\vec{R})$. The curves in Fig. 2.4 correspond to the different electronic potentials $U(R)$ for the nuclei, produced by electrons in the different states described by the right-hand-side labels (e.g. $X^1\Sigma^+$). These potentials only depend on the separation R between nuclei, and the notation for their labelling will be explained in more detail later, in Sections 2.4 and 2.5.

2.3 Vibrations and Rotations

A diatomic molecule has three main degrees of freedom: electronic, vibrational, and rotational. The separations between electronic states form the largest energy scale in a molecule, with a typical order of magnitude of $\sim 10000 \text{ cm}^{-1}$. A given electronic potential includes a set of vibrational bound states (Fig. 2.5b), and these are the next largest energy scale in a

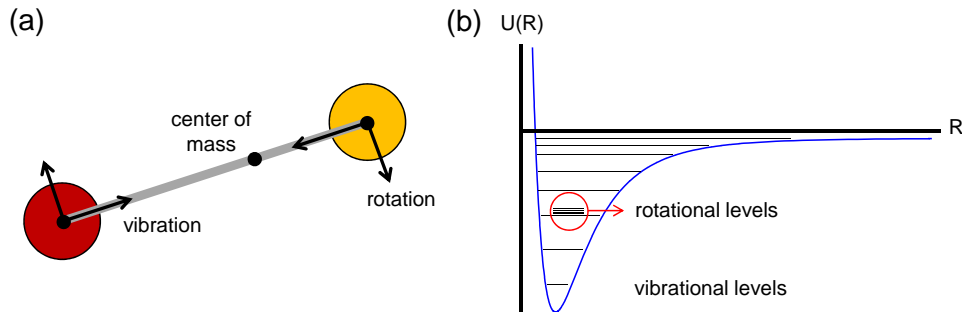


Figure 2.5: Vibrations and rotations of a diatomic molecule. A given electronic potential includes vibrational bound states with separations ranging from $\sim 1000 \text{ cm}^{-1}$ to $\sim 0.1 \text{ cm}^{-1}$ as one goes from the lowest to the highest states. A given vibrational bound state likewise contains a ladder of rotational states, with typical spacings in the $\sim 0.01\text{-}0.1 \text{ cm}^{-1}$ range for low-lying vibrational states, and getting smaller for higher vibrational states.

molecule, ranging from $\sim 1000 \text{ cm}^{-1}$ near the bottom of the potential to $\sim 0.1 \text{ cm}^{-1}$ near dissociation [Demtröder, 2005]. Finally, a given vibrational bound state contains a ladder of rotational states of the molecule. These have typical spacings in the $\sim 0.01\text{-}0.1 \text{ cm}^{-1}$ range for low-lying vibrational states, getting smaller for higher vibrational states. For reference, $0.1 \text{ cm}^{-1} = 30 \text{ GHz}$.

Since the typical energy scale of vibrational levels is much larger than that of rotational levels, this means vibrational motion happens on much faster time-scales compared to those of rotational motion. Except in the extreme case of near-dissociation vibrational bound states with large rotational excitation, a molecule will undergo many vibrational oscillations in the time it takes to make one rotation (see Fig. 2.5a for illustrations of these motions). Thus, we can first consider vibrational motion in the relative radial coordinate R in a given electronic potential $U(R)$ without including any rotational effects, and then simply add rotation as a perturbation afterwards. For a perfectly harmonic potential, the vibrational energy levels would be quantized according to $G(\nu) = \hbar\omega_e(\nu+1/2)$, where ω_e is the harmonic oscillation frequency of the electronic potential. In practice, electronic potentials such as those in Fig. 2.4 are approximately harmonic only near their minima, and quickly become anharmonic as one moves away. There is no analytic expression for the resulting energy

spectrum, and vibrational energy levels for real electronic potentials are instead described by a power series in $\nu+1/2$ [Lefebvre-Brion and Field, 2004]. The spacings between adjacent levels grow bigger with smaller reduced mass μ of the system, analogous the case of the harmonic oscillator, where $\omega_e \propto m^{-1/2}$.

The inclusion of molecular rotations to this picture can be greatly simplified by assuming that the molecule is a rigid rotor. Then the rotational energy becomes quantized according to $H_{rot} = J^2/2I$ where J is the rotational angular momentum operator and I is the moment of inertia, which in the semiclassical picture is $I = \mu R_0^2$ with R_0 being the separation of the atoms. However, since in reality a molecule undergoes many vibrational oscillations during a single rotation, R_0 is in fact some weighted separation, such as the equilibrium internuclear distance R_e , that depends on the vibrational bound state in question [Lefebvre-Brion and Field, 2004], and becomes larger as the vibrational quantum number ν increases. In this framework, the rotational energy eigenvalues are

$$F(J) = B_\nu J(J+1) \quad (2.7)$$

where $B_\nu = \hbar^2/2I = \hbar^2/2\mu R_\nu^2$ is the rotational constant that changes with the spatial extent of the ν -th vibrational bound state. Note that Eq. 2.7 does not account for the additional centrifugal distortions to the vibrational motion that comes with increasing rotation. A more general expression is $F(J) = B_\nu J(J+1) + D_\nu (J(J+1))^2$, where D_ν is the centrifugal distortion term, and is typically a small correction on the order of $10^{-6}B_\nu$ [Lefebvre-Brion and Field, 2004]. The rotational eigenstates that define the molecular axis are simply spherical harmonics $Y_{JM}(\theta, \phi)$.

2.4 Angular Momentum Quantum Numbers Λ , Σ , and Ω

The electronic states of individual, separated atoms are given, in spectroscopic notation, as $^{2S+1}L_J$. In the Born-Oppenheimer approximation from Section 2.2, when two such atoms approach one another, the $R \rightarrow \infty$ electronic states evolve adiabatically to connect to their

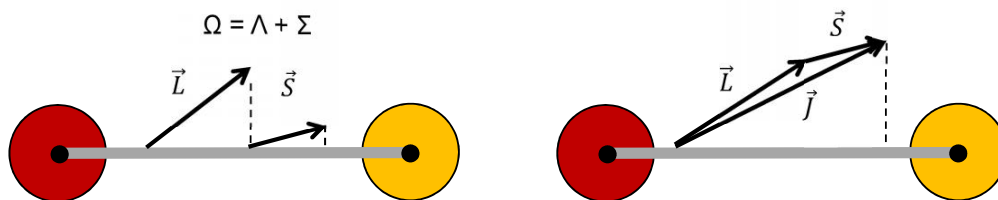


Figure 2.6: Hund's cases for electron angular momentum coupling to the molecular axis. (a) Quantum states are labelled by the projections of the electron orbital and spin angular momentum on the molecular axis, Λ and Σ , along with their sum Ω . This is referred to as Hund's coupling case (a), and is the main case that is valid for the molecules described in this dissertation. (b) In this case, states are labelled by first adding the electron orbital and spin angular momenta, $\vec{J} = \vec{L} + \vec{S}$, according to the rules of quantum mechanics, and then specifying the projection on the molecular axis $\Omega = |m_J|$. This is known as Hund's case (c), and applies to very weakly bound molecules, as well as molecules to with large constituent atoms and consequently strong spin-orbit coupling.

short-range counterparts. As shown in the labels on the right-hand-side of Fig. 2.4, the resulting electronic potentials $U(R)$ are identified by the appropriate quantum numbers at short-range ${}^{2S+1}\Lambda_{\Omega}$. This expression is known as a term symbol, and is the molecular counterpart of spectroscopic notation for atoms. The change in quantum numbers is due to the fact that the Hamiltonian of the system (Eq. 2.6) is no longer spherically symmetric. Ignoring rotations, there remains only one axis of symmetry along the line connecting the two atoms, and electronic angular momenta must therefore be quantized along this molecular axis (Fig. 2.6). The electronic wave function solutions to Eq. 2.6 for instantaneous nuclei positions \vec{R} thus become identified by their angular momentum projections along this molecular axis, with different projections leading to different potentials $U(R)$ for the much slower vibrational motion of the nuclei.

The absolute value of the electronic orbital angular momentum along the molecular axis is denoted Λ . As a historical artefact, $\Lambda = 0, 1,$ and 2 are written as $\Sigma, \Pi,$ and Δ respectively, and were chosen to be the Greek letter counterparts to atomic angular momentum quantum numbers s, p, d, etc. The electronic ground state of separated atoms, e. g. $\text{Li}(2s)+\text{Na}(3s)$, produces only Σ molecular potentials, while $\text{Li}(2p)+\text{Na}(3s)$ connects

to both Σ and Π potentials because the one unit of electronic orbital angular momentum available in Li(2p) can have projection 0 or 1 along the molecular axis. In this case, Σ and Π correspond to different potentials because they produce different electron distributions around the molecular axis. Note, however, that there is no distinction made for negative values of Λ , because this corresponds in the semi-classical picture to an electron orbiting the molecular axis with opposite circulation, which does not change the energy of the system. This means that each state Λ is doubly degenerate, and this degeneracy is only broken by the rotation of the molecule in an effect called Λ -doubling.

The quantum number S corresponds to the sum of the two valence electron spins in a diatomic alkali molecule, and takes on the values 0 or 1. The projection of S along the molecular axis is denoted by Σ (Fig. 2.6), which is confusing since the same symbol is also used to represent $\Lambda = 0$ in the molecular term symbol. However, this notation conflict is inextricably part of the standard notation in molecular physics.

Different values of S lead to different potentials because of the effect of quantum statistics. In the $S = 0$ singlet state, the two-electron spatial wave function must be symmetric under exchange, while in the $S = 1$ triplet states the wave function must be antisymmetric. This implies that, compared to singlet electrons, triplet electrons are pushed out further from one another and kept from overlapping. In a diatomic molecule, the attractive van der Waals potential is a result of electronic fluctuations polarizing the atoms and inducing dipoles. As the atoms get closer, the polarization starts to create overlap between the valence electrons, but is suppressed by quantum statistics for electrons in the triplet state, thus reducing the attraction. Consequently, while at long range the van der Waals potential is the same for the $^1\Sigma$ and $^3\Sigma$ ground states, at short range $^3\Sigma$ ends up being very shallow, while $^1\Sigma$ is deep (see Fig. 2.4). In H_2 , for example, the $^3\Sigma$ potential is so shallow that no bound state exists. In NaLi, $^3\Sigma$ has a depth of 220 cm^{-1} while for $^1\Sigma$ the depth is 7050 cm^{-1} [Mabrouk and Berriche, 2008].

For a fixed set of quantum numbers $^{2S+1}\Lambda$, there is a manifold of potentials distinguished by the prefixes shown in the right-hand-side labels of Fig. 2.4. For $^1\Sigma$ states, these prefixes

are, in order of energy, X, 1, 2, ... and correspond to different separated atom electronic states in the $R \rightarrow \infty$ limit. For example, Li(2s)+Na(3s), Li(2p)+Na(3s), and Li(2s)+Na(3p) all have $^1\Sigma$ states, and these are written $X^1\Sigma$, $1^1\Sigma$ and $2^1\Sigma$. For $^3\Sigma$ states the prefixes are 1 (or sometimes a), 2, 3, ... For all higher states ($^1\Pi$, $^3\Pi$, etc.) the prefixes are simply 1, 2, 3, ... in order of ascending energy. In some cases, non-standard notation is used, e. g. using purely letters or purely numbers, but whatever the symbols, the important point is simply that they refer to the same angular momentum projections for different separated atom asymptotes.

There is one final quantum number, Ω , that is often omitted from the standard notation for identifying molecular potentials $^{2S+1}\Lambda_\Omega$. It accounts for the relative alignment of orbital and spin angular momentum projections $\Omega = m_L + m_S$. This does not affect the electronic distribution around the molecular axis, and thus does not alter the molecular potential. The magnitude of Ω does become important when considering spin-orbit coupling between states. Also, electronic potentials at large R are labelled by Ω alone, and not $^{2S+1}\Lambda_\Omega$, because there the dominant effect becomes the energy splitting from spin-orbit coupling in the separated atoms, rather than differences in interaction energy arising from Λ or S .

2.5 Inversion Symmetries $+/-$ and g/u

Aside from the quantum numbers specifying electronic angular momentum projections along the molecular axis, there are two more quantum numbers $+/-$ and g/u that label the electronic potentials of a diatomic molecule. These correspond to two different kinds of inversion symmetry: total inversion of all coordinates relative to an origin located at the center of mass of the molecule $+/-$, and inversion of only the coordinates of the nuclei g/u (this second symmetry exists only for homonuclear diatomic molecules, consisting of two identical atoms).

All diatomic molecules possess the first of these symmetries, because an inversion of all coordinates (electronic and nuclear) does not change the energy of the system, meaning

that the inversion (or parity) operator Π commutes with the Hamiltonian of the system. Moreover, two inversion operations will restore the system to its original state $\Pi(\Pi|\psi\rangle) = |\psi\rangle$, meaning that eigenstates $|\psi\rangle$ of the Hamiltonian (Eq. 2.6) can be classified as having + or - parity with respect to total inversion.²

The action of Π on $|\psi\rangle$ can be divided into three separate actions on the vibrational, rotational, and electronic degrees of freedom of the molecule. Inversion leaves the vibrational wave function unchanged, since this depends only on the relative separation between nuclei. Rotational wave functions take the form of spherical harmonics $Y_{JM}(\theta, \phi)$, which transform under inversion according to $\Pi Y_{JM}(\theta, \phi) = Y_{JM}(\pi - \theta, \phi + \pi) = (-1)^J Y_{JM}(\theta, \phi)$. Consequently, adjacent rotational levels $J, J + 1$ always have opposite parity.

The action of Π on the electronic part of the wave function is more complicated, since the inversion occurs in the laboratory frame of reference while the electronic wave functions, in the Born-Oppenheimer approximation, are defined in a rotating molecular frame of reference. However, there is a surprising equivalence between an inversion in the laboratory frame of reference and a reflection in the x-z plane in the rotating molecular frame.³ Some authors thus refer to the +/- symmetry of the molecular state as simply reflection symmetry, for example [Demtröder, 2005], leaving the reader confused about what this has to do with parity, and how one chooses the seemingly arbitrary plane of reflection.

Using the equivalence of inversion in the laboratory frame and reflection in the molecular frame, the electronic orbital angular momentum states $|\Lambda\rangle$ transform under Π according to [Bernath, 2005; Brown and Carrington, 2003]

$$\Pi |\Lambda\rangle = (-1)^\Lambda |-\Lambda\rangle \quad (2.8)$$

It is easy to check, in the limit of separate atoms, that the spherical harmonics for electronic orbital angular momentum transform as such for a reflection in the x-z plane. For $\Lambda > 0$,

²For a detailed discussion of this subject, see [Bernath, 2005], [Demtröder, 2005], and [Brown and Carrington, 2003]

³See Chapter 9.4 of [Bernath, 2005] and a nice derivation in terms of Euler angles in Chapter 6.9 of [Brown and Carrington, 2003]

the properly (anti)symmetrized parity eigenstates are thus $(|\Lambda\rangle \pm |-\Lambda\rangle)/\sqrt{2}$. So the Π potentials in Fig. 2.4 actually contain degenerate pairs of states with + and - parity, with the degeneracy ultimately broken by the different interactions of $\pm\Lambda$ with molecular rotation. Note that, for even Λ , $(|\Lambda\rangle + |-\Lambda\rangle)/\sqrt{2}$ has + parity and $(|\Lambda\rangle - |-\Lambda\rangle)/\sqrt{2}$ has - parity, but for odd Λ the opposite is true.

When $\Lambda = 0$, Eq. 2.8 reduces to $\Pi|0\rangle = |0\rangle$, which seems to imply that all $\Lambda = 0$ states have + parity. However, more accurately, $\Pi|0\rangle = |\tilde{0}\rangle$, because Π may turn one $\Lambda = 0$ state into a different $\Lambda = 0$ state. As an example, consider $|\Lambda = 0\rangle = |p_1p_{-1}\rangle$, where in this notation we are considering, in the limit of separate atoms, one p-electron with $m_l = 1$ and another p-electron with $m_l = -1$. Then $\Pi|p_1p_{-1}\rangle = (-1)(-1)^{-1}|p_{-1}p_1\rangle$, because each individual valence electron state transforms under reflection in the x-z plane in the same way as Eq. 2.8 prescribes for $|\Lambda\rangle$, namely $\Pi|l_m\rangle = (-1)^m|l_{-m}\rangle$. The properly symmetrized parity eigenstates become $|0^\pm\rangle = (|p_1p_{-1}\rangle \pm |p_{-1}p_1\rangle)/\sqrt{2}$, meaning that a Σ potential connecting asymptotically to atoms each with a p-electron contains both + and - parity states. However, Σ potentials asymptotically connecting to s + s or s + p atoms only have + parity states, and because of this ambiguity, the parity of Σ potentials must be denoted explicitly as a superscript Σ^\pm . This corresponds to the parity of the $J = 0$ rotational states for all vibrational states in that potential, with higher J states alternating in parity. Since this alternating parity forms a predictable pattern for increasing J, sometimes the symbols e and f are used to denote the + or - parity of states when the $(-1)^J$ term is ignored [Bernath, 2005].

The second inversion symmetry g/u exists only for homonuclear diatomic molecules, and corresponds to an exchange of the nuclei. For identical nuclei, the system is indistinguishable under this transformation, and thus eigenstates of homonuclear molecules can be labelled by the terms g (gerade, for + symmetry of the wave function under the exchange of nuclei) and u (ungerade, - symmetry). An example of the lowest-lying potentials for the homonuclear molecule Li_2 is shown in Fig. 2.7, in which the g/u labels are added as suffixes to the term symbol $^{2S+1}\Lambda_{g/u}^\pm$. While at first glance it seems like there are twice as many potential curves

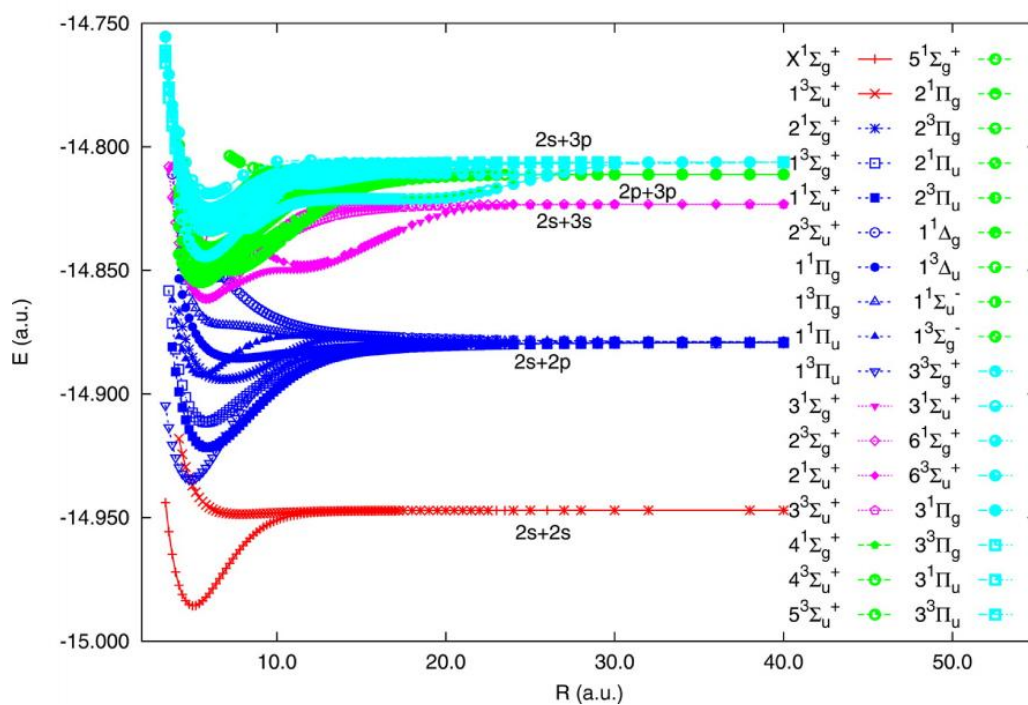


Figure 2.7: Molecular potential curves for Li_2 . For this homonuclear molecule, there is an additional symmetry g/u in the labels for the electronic potentials, corresponding to exchange of identical nuclei. Plots taken from [Musial and Kucharski, 2014]

as for the heteronuclear case, e. g. $2^1\Sigma_g^+$ and $1^1\Sigma_u^+$ are both asymptotic to $\text{Li}(2s)+\text{Li}(2p)$ while only $2^1\Sigma^+$ is asymptotic to $\text{Na}(2s)+\text{Li}(2p)$. The additional multiplicity produced by the g/u label reflects the fact that in homonuclear molecules, there is built-in ambiguity for whether the one unit of excitation comes from one atom or the other. From Section 2.1, in the limit of separate atoms, the properly (anti)symmetrized states with one unit of electronic excitation are $|\Psi^\pm\rangle = (|g_a e_b\rangle \pm |e_a g_b\rangle)/\sqrt{2}$, with the + solution corresponding to g-symmetry, and the – solution corresponding to u-symmetry.

2.6 Electric Dipole Moment

Heteronuclear diatomic molecules are those consisting of two different atoms. In these molecules, the electron is more likely to be near one atom than the other, resulting in an electric dipole moment along the molecular axis. However, in the absence of external fields, the spherical harmonic rotational states of a molecule have no preferred direction, and thus there is no electric dipole moment in the laboratory frame. More concretely, if D is the magnitude of the dipole moment along the molecular axis for a given vibrational and electronic state, and \hat{r} is the unit vector pointing from the smaller atom to the bigger one, then the dipole moment of the molecule in the laboratory frame is $\vec{d} = D \langle \psi_{rot} | \hat{r} | \psi_{rot} \rangle = 0$

To induce an electric dipole moment, an external electric field \vec{E} must be applied to break rotational symmetry. The electric field introduces off-diagonal terms of the form $-E\hat{z} \cdot D\hat{r}$, assuming that \vec{E} is along the z -direction. This term couples, for example, the $(J, m_J) = (0, 0)$ and $(1, 0)$ states, so that the resulting rotational Hamiltonian in the $\{|0, 0\rangle, |1, 0\rangle\}$ basis becomes

$$H_{rot} = \begin{pmatrix} 0 & -ED\hat{z} \cdot \hat{r} \\ -ED\hat{z} \cdot \hat{r} & 2B_\nu \end{pmatrix} \quad (2.9)$$

As E increases, it mixes the rotationally excited $|1, 0\rangle$ state into the ground state $|0, 0\rangle$, resulting in the dipole moment along the molecular axis becoming more and more aligned in the direction of the field. For $E \rightarrow \infty$, the eigenstates of H_{rot} become $|\pm\rangle = (|0, 0\rangle \pm$

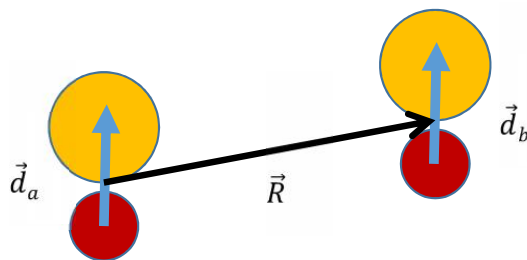


Figure 2.8: Dipole-dipole interactions between a pair of heteronuclear molecules. The dipole moment points from the smaller atom to the bigger one, meaning that the electron spends more time near the smaller atom. This interaction is long-range and anisotropic.

$|1,0\rangle)/\sqrt{2}$, with $|+\rangle$ being the solution for an aligned dipole and $|-\rangle$ being that for an anti-aligned dipole. One can evaluate the magnitude of the aligned dipole moment to be $\vec{d} = D \langle + | \hat{r} | + \rangle = D/\sqrt{3} \approx 0.58D$, using $\psi^\pm = (1 \pm \sqrt{3}\cos\theta)/\sqrt{8\pi}$. This is not the full dipole moment D because we have ignored how \vec{E} will mix in other states besides $|1,0\rangle$. From Eq. 2.9 we can define $E_0 \equiv 2B_\nu/D$ as the threshold field at which there will start to be a significant admixture of the first rotationally excited state of the molecule, corresponding simultaneously to the presence of a sizeable fraction of the full dipole moment. Note that for heteronuclear alkali molecules, the unit vector \vec{e}_r for the dipole moment always points from the smaller atom to the bigger one. This is because the bigger atom is more polarizable, meaning that its valence electron will be more easily pulled towards the smaller atom than vice versa.

The possibility of having an aligned electric dipole moment is one of the most appealing features of heteronuclear molecules, because, as illustrated in Fig. 2.8, it produces long-range interactions between pairs of molecules of the same form as Eq. 2.1, except the resulting interaction energy is first order in \hat{H}_{dip} for aligned dipoles, and scales as $1/R^3$. This dipole-dipole interaction is also anisotropic, being repulsive for dipoles aligned side-by-side, and attractive for dipoles aligned end-to end.

Power law interactions of the form $1/R^n$ are called “long-range” if $n \leq 3$. There are two

senses in which these interactions are long-range. The first is an energetic sense and the second is a collisional one. First, if one considers a dipole \vec{d} interacting with a surrounding uniform density n of other dipoles \vec{d} , the resulting interaction energy of the one dipole can be written as

$$U = \int_0^\infty \int_0^\pi \int_0^{2\pi} \frac{nd^2g(\theta, \phi)}{4\pi\epsilon_0R^n} R^2 \sin\theta \, d\phi \, d\theta \, dR \propto \int \frac{dR}{R^{n-2}} \quad (2.10)$$

with $g(\theta, \phi)$ encapsulating the angular dependence of the dipole-dipole interaction. The integral in R diverges for $n \leq 3$, meaning that up to infinite range the surrounding dipoles still contribute to the interaction energy term. Note that this argument is specific to dipoles interacting in three dimensions. It is easy to see from Eq. 2.10 that dipole-dipole interactions are short-range in the energetic sense in one and two dimensions, because the R -dependence of the volume integral changes [Lahaye *et al.*, 2009].

The second sense in which $1/R^n$ interactions are long-range for $n \leq 3$ is in the context of the two-particle scattering wave function. At zero temperature, two-body scattering from short-range $n > 3$ interactions reduce only to the s-wave term in the partial wave expansion, and can be replaced by zero-range delta function contact interactions. For $n \leq 3$ interactions, this is no longer valid. All partial waves still contribute to the scattering wave function down to $T = 0$, and the potential cannot be replaced by a zero-range one [Lahaye *et al.*, 2009]. This means, for example, that dipolar gases of identical fermions will still collide and thermalize in the $T \rightarrow 0$ limit.

The magnitudes of predicted dipole moments for the possible heteronuclear diatomic molecules formed out of alkali atoms range from 0.47 Debye on the low end for NaLi to 5.5 Debye on the high end for LiCs (1 Debye = $0.4 \, ea_0$ where e is the elementary charge and a_0 is the Bohr radius). Table 2.2 gives the dipole moments D for a representative set of heteronuclear molecules that are currently being studied experimentally⁴, along with their

⁴Values for D are obtained from [Aymar and Dulieu, 2005] and references therein, except for that of KRb, which is obtained from [Ni *et al.*, 2008]

	$^{23}\text{Na}^6\text{Li}$	$^{40}\text{K}^{87}\text{Rb}$	$^{87}\text{Rb}^{133}\text{Cs}$	$^{23}\text{Na}^{40}\text{K}$	$^6\text{Li}^{40}\text{K}$	$^7\text{Li}^{133}\text{Cs}$
D (Debye)	0.47	0.57	1.2	2.7	3.5	5.5
B_0 (cm^{-1})	0.43	0.037	0.016	0.0097	0.30	0.22
E_0 (kV/cm)	110	8	1.6	0.44	11	4.9

Table 2.2: Key properties of a representative set of possible heteronuclear diatomic alkali molecules, given in order of increasing dipole moment along the molecular axis D . The rotational constant B_0 of the absolute ground state (vibrational and electronic) is also given, as is the threshold field $E_0 = 2B_0/D$ for inducing a significant fraction of the full dipole moment of the molecule. Note that the breakdown field in air is 10 kV/cm

ground-state rotational constants B_0 and threshold fields E_0 required to align the dipoles.⁵ This is by no means an exhaustive list of all the possible heteronuclear combinations that can be formed out of the alkalis Li, Na, K, Rb, Cs, and Fr.

For two aligned, side-by-side dipoles, Eq. 2.1 gives an expression for the interaction energy $U_{dd} = d^2/(4\pi\epsilon_0 R^3)$. Assuming that the dipoles are $R = 532$ nm apart in a 1064-nm optical lattice, $U_{dd}/h = 300$ Hz for NaLi and 28 KHz for LiCs. The two orders of magnitude difference between the two is accounted for by the d^2 scaling of U_{dd} . Still, both are still far larger than the magnetic dipole-dipole interaction energy between atoms. Even for dysprosium, which has a magnetic moment $\mu = 10\mu_B$ and is the most magnetic atom, $U_{dd}/h = \mu_0\mu^2/(4\pi R^3) = 10$ Hz, where μ_0 is the permeability of free space, μ_B is the Bohr magneton, and we have again used $R = 532$ nm.

2.7 Electric Dipole Selection Rules

The quantum numbers from Sections 2.4 and 2.5 allow us to define selection rules for the allowed vibrational, rotational and electronic transitions in diatomic molecules. The simplest selection rules have to do with the inversion symmetries of the molecule from Section 2.5. The electric dipole operator \vec{d} has $-$ symmetry under both a total inversion of all coordinates Π , and under exchange of identical nuclei in a homonuclear molecule. Thus,

⁵Values for B_0 obtained from using R_e from [Aymar and Dulieu, 2005] and taking $B_0 = \hbar^2/2\mu R_e^2$, which for KRb is well within 1% of the experimental value from [Ni, 2009], and in general should be accurate to well within 10%

allowed electric dipole transitions must connect states of opposite symmetry, $+ \leftrightarrow -$ and $g \leftrightarrow u$. Transitions between states of the same symmetry are electric-dipole forbidden.

In order to consider further selection rules, we can write the dipole operator more concretely as $\vec{d} = -e \sum \vec{r}_i + Z_1 e \vec{R}_1 + Z_2 e \vec{R}_2$, where \vec{r}_i and \vec{R}_j represent the electronic and nuclear coordinates respectively, and their origin is located at the center of mass of the molecule. We can write this as $\vec{d} = \vec{d}_{el} + \vec{d}_{nuc}$, and the question of allowed transitions becomes a question of initial and final states $|\psi_i\rangle$ and $|\psi_f\rangle$ for which the matrix element $\langle \psi_f | \vec{d} | \psi_i \rangle \neq 0$.

In the Born-Oppenheimer approximation, $|\psi\rangle$ can be separated into electronic and nuclear components $|\psi\rangle = |\psi_{el}\rangle |\psi_{nuc}\rangle \equiv \phi \chi$, and following [Demtröder, 2005], we can write

$$\begin{aligned} \langle \psi_f | \vec{d} | \psi_i \rangle &= \int \int \phi_f^* \chi_f^* (\vec{d}_{el} + \vec{d}_{nuc}) \phi_i \chi_i d^3 \vec{r} d^3 \vec{R} \\ &= \int \chi_f^* \left(\int \phi_f^* \vec{d}_{el} \phi_i d^3 \vec{r} \right) \chi_i d^3 \vec{R} \\ &\quad + \int \chi_f^* \vec{d}_{nuc} \left(\int \phi_f^* \phi_i d^3 \vec{r} \right) \chi_i d^3 \vec{R} \end{aligned} \quad (2.11)$$

This conveniently separates $\langle \psi_f | \vec{d} | \psi_i \rangle$ into two contributions. For transitions within the same electronic potential, $\int \chi_f^* \left(\int \phi_f^* \vec{d}_{el} \phi_i d^3 \vec{r} \right) \chi_i d^3 \vec{R} = 0$ due to the parity of \vec{d}_{el} , while for transitions between different electronic states, $\int \chi_f^* \vec{d}_{nuc} \left(\int \phi_f^* \phi_i d^3 \vec{r} \right) \chi_i d^3 \vec{R} = 0$ because of the orthonormality of ϕ_i and ϕ_f .

In the first case of transitions within the same electronic potential

$$\langle \psi_f | \vec{d} | \psi_i \rangle = \int \chi_f^* \vec{d}_{nuc} \chi_i d^3 \vec{R} \quad (2.12)$$

from which we can immediately see that if the molecule is homonuclear, then $\vec{d}_{nuc} = 0$, implying that there are no allowed ro-vibrational transitions. For heteronuclear molecules, ro-vibrational transitions are allowed. If we separate χ into rotational and vibrational parts $\chi = \xi(R) Y_{JM}(\theta, \phi)$, the angular part of the integral in Eq. 2.12 becomes $\int Y_{J'M'}^* \vec{d}_{nuc} Y_{JM} d\Omega$. The selection rules for such an integral are familiar from the Wigner-Eckart Theorem as

applied to alkali atoms [Steck, 2010], and the result is $\Delta J = \pm 1$ and $\Delta M_J = 0, \pm 1$. Historically, $\Delta J = 1$ transitions have been referred to as belonging to the R-branch, while $\Delta J = -1$ belongs to the P-branch. The $\Delta J = 0$ case is allowed by the Wigner-Eckart theorem, but is forbidden by parity. If the electronic potential were perfectly harmonic, then only $\Delta \nu = \pm 1$ vibrational transitions would be allowed, but since real electronic potentials for molecules are highly anharmonic, no selection rules exist for ν .

For transitions between different electronic potentials, Eq. 2.11 becomes

$$\begin{aligned} \langle \psi_f | \vec{d} | \psi_i \rangle &= \int \chi_f^* \left(\int \phi_f^* \vec{d}_{el} \phi_i d^3 \vec{r} \right) \chi_i d^3 \vec{R} \\ &= \int \chi_f^* \vec{D}_{el}(R) \chi_i d^3 \vec{R} \end{aligned} \quad (2.13)$$

The angular part of this integral gives us the same constraints $\Delta J = 0, \pm 1$, and these are all allowed as long as the parity selection rules $+ \leftrightarrow -$ and $g \leftrightarrow u$ are followed. To give some examples, still only $\Delta J = \pm 1$ are allowed for ${}^1\Sigma^+ \rightarrow {}^1\Sigma^+$ transitions, while only $\Delta J = 0$ is allowed for ${}^1\Sigma^+ \rightarrow {}^1\Sigma^-$. Finally, $\Delta J = 0, \pm 1$ are all allowed for ${}^1\Sigma^+ \rightarrow {}^1\Pi$.

We can go one step beyond this and do a Taylor series expansion of $\vec{D}_{el}(R)$ around some $R = R_0$ and keep only the leading term $\vec{D}_{el}(R_0)$ [Demtröder, 2005; Bernath, 2005]. Then, ignoring rotations, Eq. 2.13 becomes $\langle \psi_f | \vec{d} | \psi_i \rangle = \vec{D}_{el}(R_0) \langle \nu_f | \nu_i \rangle$, with $\vec{D}_{el}(R_0)$ representing the dipole matrix element for the electronic transition at some mean $R = R_0$, and with an additional vibrational wave function overlap term $\langle \nu_f | \nu_i \rangle$. This last term is some times referred to as the Franck-Condon factor of the transition, and is a qualitative way of estimating the magnitude of the matrix elements between different vibrational levels. For larger ν , the weight of the wave function becomes concentrated at the classical turning points of the potential, and having a large Franck-Condon overlap factor becomes equivalent to having the classical turning points of ν_i and ν_f line up. In the semi-classical picture, an electronic excitation happens on a time scale much faster than vibrational motion in a molecule, meaning that the nuclei will essentially have the same positions and velocities before and after the excitation.

2.8 Spin-Orbit Coupling

Thus far, we have treated the electronic, rotational and vibrational states of diatomic molecules in an idealized, Born-Oppenheimer approximation context. However, there exist various additional terms that modify molecular states in significant ways. One of these is the spin-orbit coupling term [Demtröder, 2005; Lefebvre-Brion and Field, 2004]

$$H_{so} = \sum_i a_i \vec{l}_i \cdot \vec{s}_i \quad a_i \vec{l}_i = \sum_{k=1}^2 \frac{\alpha^2}{2} \frac{Z_k^{eff}}{r_{ik}^2} \vec{l}_{ik} \quad (2.14)$$

where \vec{l}_i and \vec{s}_i are the individual electron orbital and spin angular momenta, $\alpha = 1/137$ is the fine-structure constant, r_{ik} is the distance from the i -th electron to the k -th nucleus, \vec{l}_{ik} is the corresponding orbital angular momentum, and Z_k^{eff} is the effective nuclear charge. Spin-orbit coupling is responsible for splitting $^{2S+1}\Lambda_\Omega$ states depending on Ω , which captures the relative alignment between the electronic orbital momentum projection Λ and the spin projection Σ .

The spin-orbit coupling term H_{so} also couples states from different electronic potentials according to $+ \leftrightarrow -$, $g \leftrightarrow u$, $\Delta\Omega = 0$, $\Delta S = 0$ or ± 1 , $\Delta\Lambda = \Delta\Sigma = 0$ or $\Delta\Lambda = -\Delta\Sigma = \pm 1$. For example, among the lowest lying electronic potentials of Li+Na in Fig. 2.4, $2^1\Sigma^+$ and $1^3\Pi$ are coupled by H_{so} . If a bound state in $2^1\Sigma^+$ and another in $1^3\Pi$ fall are separated by less than the scale of the spin-orbit coupling energy $a_i\hbar^2$, they will be mixed by H_{so} and the resulting eigenstate will possess both singlet and triplet wave function components. This is significant because electric dipole transitions do not change the spin of the molecule, so connecting singlet states to triplet states and vice versa requires spin-orbit coupling of these near-degenerate levels.

The spin-orbit coupling energy scale can be estimated by simply taking it to be the spin-orbit splitting in the corresponding atom [Brown and Carrington, 2003]. For instance, in Fig. 2.4, $2^1\Sigma^+$ and $1^3\Pi$ both connect to the Li(2p)+Na(3s) asymptote, so we can estimate the spin-orbit coupling between these two potentials from the fine-structure splitting of

${}^6\text{Li}(2p)$, which is 10 GHz or 0.3 cm^{-1} and ranks as the smallest among the alkali atoms. This means that, given the uncertainty of the best available theoretical potentials, it is extremely challenging to predict where there will be two near-degenerate states that mix via spin-orbit coupling. At present, all efforts to search for such a coupled state as an avenue for transferring singlet molecules to triplet, and vice versa, have been unsuccessful [Steinke *et al.*, 2012].

Chapter 3

Feshbach Resonances and Molecule Formation

The process of two atoms joining together to form a molecule is one of the simplest reactions in chemistry. Under normal conditions, this happens when collisions arising from the random thermal motion of the atoms brings two of them together in just the right way to form a molecule. With ultracold atoms, this random thermal motion is almost completely gone, and atom pairs can be adiabatically converted to a bound-state via something called a Feshbach resonance. The rest of this chapter will explain how this works.

In Section 3.1, we start by reviewing the highlights of the theory of low-energy scattering. This is followed by a treatment of resonant scattering in a simple, square-well model potential in Section 3.2, which introduces many of the concepts involved with Feshbach resonances. Section 3.3 discusses, in the context of two coupled square wells, how Feshbach resonances arise when a bound-state in one molecular potential is tuned to coincide with the zero-energy asymptote of a colliding atom pair. This is followed by an description of the asymptotic bound-state method in Section 3.4, which is a simple yet realistic way of modeling how Feshbach resonances occur. The topic of molecule formation around a Feshbach resonance is treated in detail in Section 3.5, and the chapter concludes with the theory of the BEC-BCS crossover for ultracold fermionic atoms around a Feshbach resonance.

3.1 Scattering at Ultracold Temperatures

From the basic theory of scattering in quantum mechanics [Landau and Lifshitz, 1977], when two atoms undergo an elastic collision, their wave function, far away from the range of the spherically symmetric interaction potential $U(r)$, must be a sum of free particle plane wave and spherical wave solutions in the relative coordinate \vec{r}

$$\psi_k(r, \theta) \sim e^{ikz} + f(\theta) \frac{e^{ikr}}{r} \quad r \rightarrow \infty \quad (3.1)$$

where k is the free atom wave vector, r is the separation in the relative coordinate system, and θ is the angle from the initial collision axis. The function $f(\theta)$ is called the scattering amplitude (Fig. 3.1). The general solution can be written in the partial wave expansion as

$$\psi_k(r, \theta) = \sum_{l=0}^{\infty} a_l P_l(\cos \theta) R_{kl}(r) \quad (3.2)$$

where $P_l(\cos \theta)$ are the Legendre polynomials and $R_{kl}(r)$ satisfies the radial equation

$$\frac{1}{r^2} \frac{d}{dr} \left(r^2 \frac{dR_{kl}}{dr} \right) + \left(k^2 - \frac{l(l+1)}{r^2} - \frac{2\mu}{\hbar^2} U(r) \right) R_{kl} = 0 \quad (3.3)$$

where μ is the reduced mass of the two-atom system. The $l = 0$ term is referred to as s-wave, the $l = 1$ term as p-wave, etc.

The $r \rightarrow \infty$ form of the solution to Eq. 3.3 is

$$R_{kl} \sim \frac{1}{r} \sin(kr - l\frac{\pi}{2} + \eta_l) \quad (3.4)$$

If the scattering potential $U(r) = 0$, then the phase shifts $\eta_l = 0$ as well, and substituting the solution in Eq. 3.4 back into Eq. 3.2 along with the coefficients

$$a_l = \frac{1}{2k} (2l+1) i^l e^{i\eta_l} \quad (3.5)$$

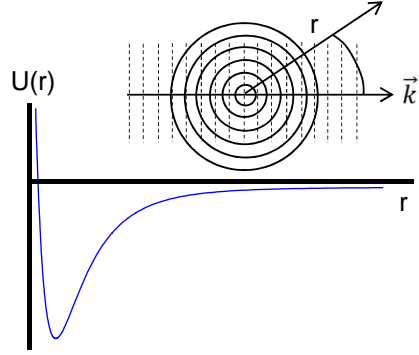


Figure 3.1: Two atom scattering in relative coordinates from a spherically symmetric potential $U(r)$. Far away from the range of the potential, as $r \rightarrow \infty$ and $U(r) \rightarrow 0$, the wave function in the relative coordinate \vec{r} is a sum of free particle plane wave and spherical wave solutions.

recovers the partial wave expansion for e^{ikz} . Thus, the effect of $U(r)$ at short range is seen in the $r \rightarrow \infty$ limit only as phase shifts η_l to the radial wave function.

Combining Eq. 3.4 and 3.5, the scattering amplitude becomes

$$\begin{aligned}
 f(\theta) &= \sum_{l=0}^{\infty} (2l+1) f_l P_l(\cos \theta) & (3.6) \\
 f_l &= \frac{1}{2ik} (e^{2i\eta_l} - 1) \\
 &= k^{-1} e^{i\eta_l} \sin \eta_l \\
 &= \frac{1}{k \cot \eta_l - ik} \\
 &= k^{-1} (\sin \eta_l \cos \eta_l + i \sin^2 \eta_l)
 \end{aligned}$$

which includes several useful and equivalent ways of writing the contribution f_l from each partial wave to $f(\theta)$.

The total scattering cross section is then

$$\sigma = \frac{4\pi}{k^2} \sum_{l=0}^{\infty} (2l+1) \sin^2 \eta_l \quad (3.7)$$

In the zero temperature limit $k \rightarrow 0$, $\tan \eta_l \rightarrow k^{2l+1}$, or more accurately, $\tan \eta_l \rightarrow$

$(ka_l)^{2l+1}$ [Walraven, 2010] where a_l is the scattering length for the l -th partial wave, which will be defined concretely in Section 3.2. To avoid a conflict in notation, the $l = 0$ scattering length is written simply as a to avoid confusion with the Bohr radius a_0 . Thus, at ultracold temperatures, all other partial wave contributions aside from $l = 0$ can be neglected. The limiting temperature can be estimated by requiring $ka_l \ll 1$ for $l \geq 1$, which gives $T \ll T_{\text{lim}} \sim 1$ mK for alkali atoms, with T_{lim} varying somewhat for different atoms according to $T_{\text{lim}} \sim \mu^{-2} a_l^{-1}$. A good estimate for a_l is $\sim 50 - 100 a_0$, although in rare cases, a term a_l might diverge for $l > 0$ due to the presence of a higher-partial-wave scattering resonance, in which case its contribution to $f(\theta)$ and σ can no longer be neglected. The topic of scattering resonances will be treated in greater detail throughout the rest of this chapter.

When the two colliding atoms are identical bosons (or fermions), the scattering wave function must be (anti)-symmetrized with respect to exchange of the atom pair. This is carried out in the scattering amplitude $f(\theta) \rightarrow f(\theta) \pm f(\pi - \theta)$, where the $+$ term corresponds to symmetrization for bosons, and the $-$ term corresponds to anti-symmetrization for fermions. For $l = 0$, $f(\theta)$ is independent of θ , which means that for fermions the anti-symmetrized scattering amplitude is zero. In other words, at ultracold temperatures, s-wave scattering of fermionic atoms is prohibited by quantum statistics.

3.2 The Radial Square Well Potential and Scattering Resonances

The simple example of two atoms scattering from a spherically symmetric square well interaction potential (Fig. 3.2) already captures the key concepts in the theory of Feshbach resonances: phase shifts, resonant enhancement of the scattering cross section, equivalence to a delta function pseudo-potential, presence of a near-dissociation bound state, etc. At ultracold temperatures, where only the s-wave term is important, the scattering problem can be solved in two separate regions, $r < r_0$ and $r > r_0$, followed by connecting the solutions at $r = 0$ in a way that satisfies continuity conditions.

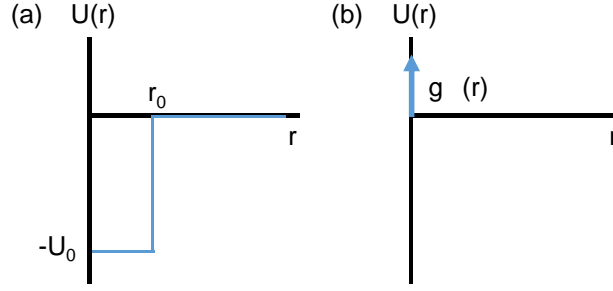


Figure 3.2: Scattering from a radial square well with depth U_0 and range r_0 . In the zero temperature limit, the square well in (a) and the delta potential in (b) give the same s-wave phase shift η_0 at large distances for $g = 4\pi\hbar^2 a/\mu$, where a is the s-wave scattering length

The radial Schrödinger equation (Eq. 3.3) can be solved by substituting $\chi_0(r) = rR_{k0}$

$$-\frac{\hbar^2}{2\mu} \frac{d^2}{dr^2} \chi_0(r) + U(r)\chi_0(r) = E\chi_0(r) \quad (3.8)$$

The separate, un-normalized solutions inside and outside the potential well $U(r)$ are then

$$\begin{aligned} \chi_0(r) &= A \sin(K_+ r) & r < r_0 \\ \chi_0(r) &= B \sin(kr + \eta_0) & r > r_0 \end{aligned} \quad (3.9)$$

where the solution for $r < r_0$ is constrained by the boundary condition $\chi_0(0) = 0$, while the $r > r_0$ solution has η_0 as a free parameter. We have defined the wave vectors K_+ , κ_0 , and k , with $K_+^2 = k^2 + \kappa_0^2$, $U_0 = \hbar^2 \kappa_0^2 / (2\mu)$, and $E = \hbar^2 k^2 / (2\mu) \rightarrow 0$ in the limit of zero temperature.

To connect the solutions in Eq. 3.9 at $r = r_0$, we require $\chi_0(r)$ and $d\chi_0(r)/dr$ to be continuous. Combining these two requirements gives

$$K_+ \cot(K_+ r_0) = k \cot(kr_0 + \eta_0) \quad (3.10)$$

In the $k \rightarrow 0$ limit this becomes $\kappa_0 \cot(\kappa_0 r_0) = 1/(r_0 + \eta_0/k)$, which assumes that $\eta_0 \ll 1$. The s-wave scattering length can be defined in these limits as $a = -\eta_0/k$, or for arbitrary

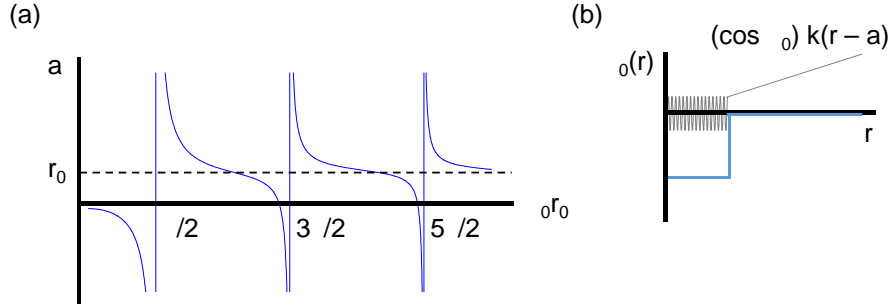


Figure 3.3: Resonant enhancement of scattering length a in a radial square well potential. (a) The scattering length a diverges for discrete values of $\kappa_0 r_0$. (b) At ultracold temperatures, $\kappa r_0 \ll 1$, meaning that on the scale of the potential well $U(r)$ the solution for $r > r_0$ is linear $\chi_0(r) \sim (\cos \eta_0)k(r - a)$, while the solution for $r < r_0$ oscillates rapidly

η_0 as $a = 1 - \tan(\kappa_0 r_0 + \eta_0)/(\kappa_0 r_0)$, resulting in

$$a = r_0 \left(1 - \frac{\tan(\kappa_0 r_0)}{\kappa_0 r_0} \right) \quad (3.11)$$

This implies that for discrete well depths corresponding to $\kappa_0 r_0 = (2n - 1)\pi/2$, $n = 1, 2, 3, \dots$ the scattering length a diverges (Fig. 3.3a). Moreover, since for typical potentials $\kappa_0 r_0 \gg 1$, away from these divergences, the value of a quickly returns to the background scattering length value $a_{bg} = r_0$, which makes sense since a is a measure of the size of the scattering potential.

The solution in Eq. 3.11 for the scattering length completely determines the scattering amplitude and the total scattering cross section of the potential via Eq. 3.6 and 3.7, with the latter of these being $\sigma = 4\pi a^2$ for $ka \ll 1$ and $\sigma = 4\pi/k^2$ for $ka \gg 1$. The limit $ka \gg 1$ is called the unitarity limit, because $\sin^2 \eta_0 = 1$ in Eq. 3.7. Also, as illustrated in Fig. 3.2b, the square well with depth U_0 produces the same phase shift η_0 as a delta function potential with height $g = 4\pi\hbar^2 a/\mu$, which means they have the same scattering properties. The potential $U(r) = g\delta(r)$ is called the s-wave pseudo-potential counterpart to the square well potential. Thus, when a diverges, the square well potential acts like a zero-range contact interaction with diverging interaction strength g .

Finally, the scattering length a also affects the relative amplitudes of the solutions for $r < r_0$ and $r > r_0$. This is shown in Fig. 3.3b. For $r > r_0$, the $k \rightarrow 0$ oscillating solution is linear on the scale of $U(r)$, and a first-order Taylor series expansion at $r = r_0^+$ gives $\chi_0(r) \sim (\cos \eta_0)k(r - a)$. Thus, one can equivalently define the scattering length a as the r -axis intercept of the tangent to $\chi_0(r)$ at $r = r_0$. Note that the slope of the tangent is proportional to $\cos \eta_0$. For small a , $\cos \eta_0 \sim 1$. Since both $\chi_0(r)$ and $d\chi_0(r)/dr$ are required to be continuous at $r = r_0$, it means that the slow oscillations of the wave function for $r > r_0$ will have much higher amplitude than the fast oscillations within the range of the potential well $r < r_0$ (as depicted in Fig. 3.3b). However, whenever a diverges, $\cos \eta_0 = 0$, and the two oscillation amplitudes will be exactly equal. Thus, in the case of diverging a , the scattering wave function within the potential well reaches its maximum amplitude.

The condition $\kappa_0 r_0 = (2n - 1)\pi/2$ for diverging a corresponds to the appearance of a new bound state in the square well potential $U(r)$ at the $E = 0$ dissociation threshold. To see this, we can solve the radial Schrödinger equation (Eq. 3.3) for negative energies $E_b = -\hbar^2 \kappa^2 / (2m)$.

$$\begin{aligned} \chi_0(r) &= A \sin(K_- r) & r < r_0 \\ \chi_0(r) &= B e^{-\kappa r} & r > r_0 \end{aligned} \quad (3.12)$$

where we have defined $K_-^2 = -\kappa^2 + \kappa_0^2$. Imposing the continuity conditions again for $\chi_0(r)$ and $d\chi_0(r)/dr$ gives

$$K_- \cot(K_- r_0) = -\kappa \quad (3.13)$$

In the $k \rightarrow 0$ limit, $\kappa = -\kappa_0 \cot(\kappa_0 r_0)$. From Eq. 3.11, $\kappa = 1/(a - r_0)$, which for diverging scattering length $a \gg r_0$ means the energy of the near-dissociation bound state is $E_b = -\hbar^2 / (2\mu a^2)$. In addition, the wave function of the bound state outside the range of the potential well falls off as $e^{-r/(a-r_0)}$, meaning that for diverging a , the near-dissociation bound state has a very large spatial extent a that stretches far beyond its classical turning point. This two-particle bound state with infinitesimal binding energy and large spatial

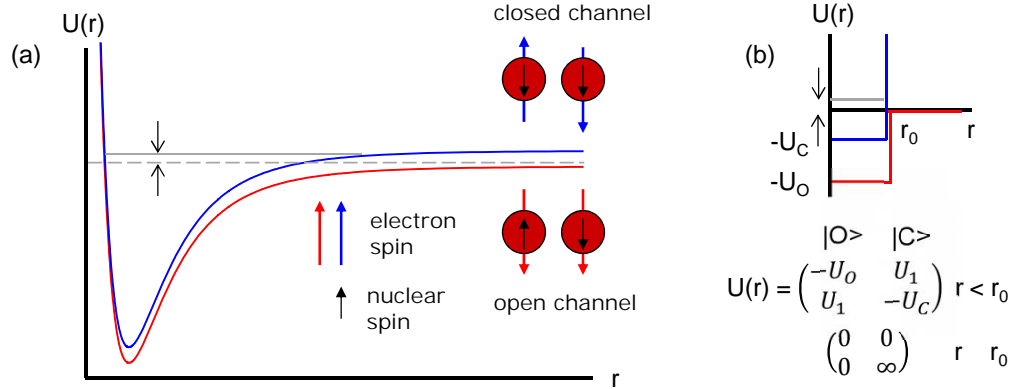


Figure 3.4: Two-channel coupling model for a Feshbach resonance. (a) For an atom pair scattering along the open-channel interaction potential (red), a scattering resonance occurs when a closed-channel potential for the same atom pair with different internal states (blue) has a bound state resonant ($\epsilon = 0$) with the zero-energy asymptote of the open channel. The atom pairs are both in their $n_{aS} + n_{bS}$ electronic ground states, and differ only in their internal electronic and nuclear spin states. The total spin projection m_F of the open-channel atom pair is the same as that of the closed-channel atom pair. (b) A simplified model consisting of an open-channel scattering potential (red), a single bound-state of interest in a closed channel potential (blue), and a coupling term U_1 between the two channels

extent is called a long-range (or halo) dimer.

3.3 Feshbach Resonances

In Section 3.2, scattering resonances in a radial square well potential occurred for discrete well depths at which a new bound state emerged at the dissociation threshold. Yet interaction potentials between real atoms (as described in Section 2.2) do not in general have variable depths. However, a pair of atoms scattering along some interaction potential can experience something analogous called a Feshbach resonance. The model for how this happens is shown in Fig. 3.4a.

The interaction potential along which the atom pair in question scatters is called the open-channel. On its own, this open-channel potential has some existing background scattering length a_{bg} , based on the phase shift it imposes on the scattering wave function. If we consider another nearby interaction potential that dissociates into individual atoms in

different internal states, then a Feshbach resonance can occur whenever one of the bound state in this second, closed-channel potential coincides with the zero-energy asymptote of the open-channel ($\epsilon = 0$ in Fig. 3.4a). When this happens, the scattering length of the open-channel potential diverges, exactly as if its depth had been adjusted to allow a new bound state to appear at the dissociation threshold.

The detuning ϵ between the closed-channel bound state and the open-channel zero-energy asymptote can be tuned by applying an external magnetic field \vec{B} . The open and closed-channel potentials dissociate into atom pairs with different internal states, so they experience a differential Zeeman shift with applied magnetic field, resulting in

$$\epsilon = \epsilon_0 + \Delta\mu B \quad (3.14)$$

where ϵ_0 is the energy offset at zero field, while $\Delta\mu$ is the differential magnetic moment along the field direction between open and closed-channel atom pairs. From Section 2.1 we know that the near-dissociation bound-state spacings for molecular potentials is \sim GHz for the first two states, and rapidly grows for the more deeply bound ones. This is comparable to the hyperfine spacings in alkali atoms [Steck, 2010], which determine the separations between open and closed-channel asymptotes in Fig. 3.4a. Since $\Delta\mu$ for atom pairs with different electronic spins is on the order of the Bohr magneton $\mu_B = 1.4$ MHz/G, this means that with typical laboratory magnetic fields of up to ~ 1000 G, ϵ can be tuned by at most 1 – 2 GHz. Consequently, for most alkali atom pairs such as Li+Na and Li+Li, the only experimentally accessible Feshbach resonances are those produced by the least-bound vibrational state of a closed-channel potential.

The exactly solvable radial square well model for resonant scattering from Section 3.2 can be extended to two coupled square wells (Fig. 3.4b) in a manner that still captures the essential physics of Feshbach resonances [Chin, 2005]. In this simplified two-channel model, the open-channel potential is the same as that of the radial square well from Section 3.2, with a non-resonant U_0 such that the scattering length of the open channel alone is $a_{bg} \approx r_0$.

The closed-channel potential is modelled as an infinite square well with the same radius r_0 and with a single, near-resonant bound state of interest at an energy offset ϵ . Within the range of the two potential wells $r < r_0$, there is a term U_1 that couples the open and closed channels. This term is critical, because without it, scattering in the open channel will be unaffected by the closed-channel bound state.

In the presence of coupling U_1 , there is a Feshbach resonance when the closed-channel bound state approaches the zero-energy asymptote of the open channel, which causes the scattering length a to diverge (Fig. 3.5a) according to

$$a = a_{bg} \left(1 - \frac{\Delta\mu\Delta B}{\epsilon - \epsilon_{res}} \right) = a_{bg} \left(1 - \frac{\Delta B}{B - B_{res}} \right) \quad (3.15)$$

where $\Delta B \sim U_1^2(a_{bg} - r_0)^2/a_{bg}$ parametrizes the width of scattering length enhancement [Chin, 2005]. The U_1 -dependence of ΔB comes from the fact that increasing U_1 increases the mixing between open and closed-channels near resonance, resulting in a larger range over which the closed-channel bound state enhances scattering in the open channel. The a_{bg} dependence comes from the discussion in Section 3.2 of how a larger a_{bg} results in a higher amplitude of the open-channel scattering wave function within the range of the square well $r < r_0$, which again results in a stronger coupling between channels, because the coupling depends on both U_1 and the radial wave function overlap between open and closed channels. A bound state also appears together with scattering length enhancement for $\epsilon < \epsilon_{res}$ (Fig. 3.5b), and behaves near ϵ_{res} exactly like the long-range dimer from Section 3.2, with energy

$$E = \frac{-\hbar^2}{2\mu a^2} = \frac{-\hbar^2}{2\mu a_{bg}^2} \left(\frac{B - B_{res}}{\Delta B} \right)^2 \quad (3.16)$$

and wave function $\psi \sim e^{-r/(a-r_0)}$ in the classically forbidden region $r > r_0$.

Note, however, that the value $\epsilon = \epsilon_{res}$ at which a diverges and the near-dissociation bound state appears is not $\epsilon = 0$, exactly where the closed-channel bound state crosses the open-channel zero-energy asymptote. Instead, the center of the Feshbach resonance ϵ_{res} is shifted by $\Delta\mu\Delta B$ from $\epsilon = 0$. This is because, in the presence of the coupling term Ω ,

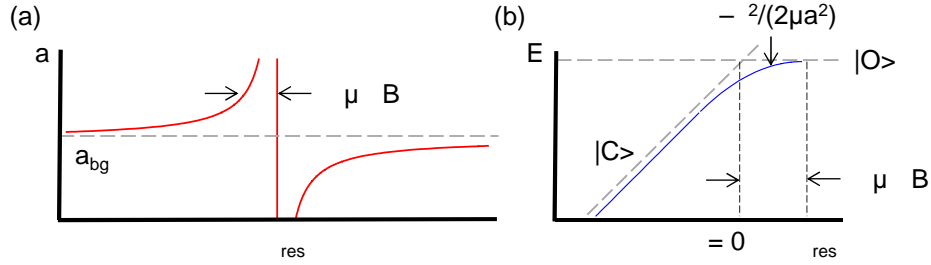


Figure 3.5: Scattering length enhancement and bound-state behaviour in the two coupled square wells model of a Feshbach resonance. (a) Near the resonance ϵ_{res} , a diverges from the background value a_{bg} , with a width of scattering length enhancement parametrized by ΔB . (b) The behaviour of the bound state energy (blue) is analogous to that of a long-range dimer, and arises due to an avoided crossing between the open-channel $|O\rangle$ and closed channel $|C\rangle$

the closed-channel bound state $|C\rangle$ and the open-channel scattering state $|O\rangle$ behave like a two-level system with an avoided crossing (Fig. 3.5b). For $\epsilon \ll \epsilon_{res}$, the bound-state energy becomes asymptotic to the energy of the energy of $|C\rangle$, meaning that, far away from resonance, the bound-state is entirely in the closed-channel. However, near resonance, the bound-state of the two coupled channels is actually a superposition of the open-channel scattering scattering wave function and the closed-channel bound state. Its energy thus becomes quadratic near ϵ_{res} according to Eq. 3.16, and only reaches the $E = 0$ dissociation limit at $\epsilon_{res} = \Delta\mu\Delta B$.

In the limit $\epsilon = \epsilon_0$, the bound-state wave function is actually entirely in the open channel, which makes sense given that the slope of the bound-state energy there is zero. To estimate the range around the avoided crossing over which the closed-channel wave function enters into the superposition, we can calculate the point at which the near-dissociation bound-state energy in Eq. 3.16 has the slope $\Delta\mu$ of the true closed channel bound state with changing B . We can write this as

$$\frac{-\hbar^2}{2\mu a_{bg}^2} \frac{d}{dB} \left(\frac{B - B_{res}}{\Delta B} \right)^2 = \Delta\mu \quad (3.17)$$

which gives $B - B_{res} = -\zeta\Delta B$ or $\epsilon - \epsilon_{res} = -\zeta\Delta\mu\Delta B$, where $\zeta = \Delta B\Delta\mu/\frac{\hbar^2}{\mu a^2}$ is the parameter describing the fraction of ΔB over which the bound-state is open-channel dom-

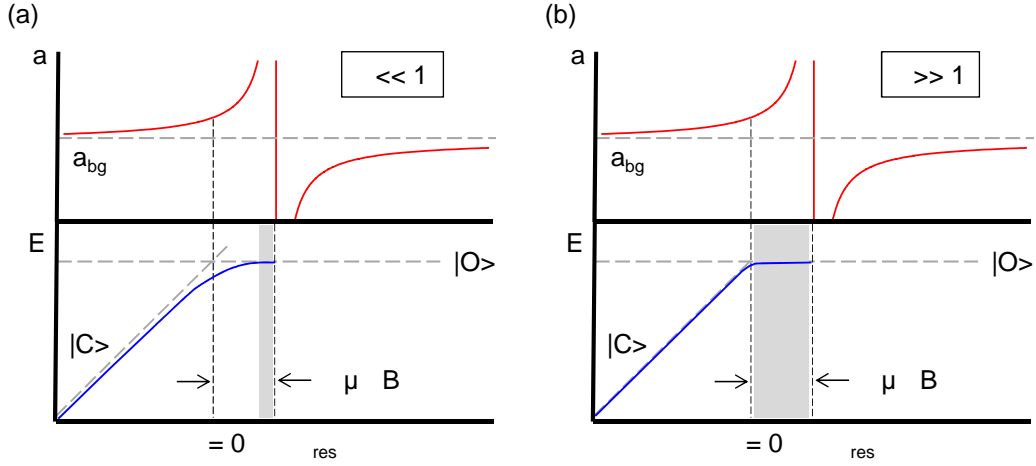


Figure 3.6: Open vs. closed-channel dominated Feshbach resonances. (a) A closed-channel-dominated resonance has $\zeta \ll 1$. The top plot (red) shows the scattering length modification near resonance, while the bottom plot (blue) shows the bound-state energy. The shaded region $\epsilon - \epsilon_{res} \ll \zeta \Delta\mu\Delta B$, where the bound-state energy closely follows that of the open-channel, is much smaller than the range of scattering length enhancement $\Delta\mu\Delta B$. In this region, the bound-state has a vanishing closed-channel admixture. (b) In an open-channel-dominated resonance, $\zeta \gg 1$, and the shaded region essentially spans the entire range of scattering length modification

inated (Fig. 3.6). If we define an energy scale $E_0 = (\Delta B\Delta\mu)^2 / \frac{\hbar^2}{\mu a^2}$, then the open-channel-dominated region is equivalently $\epsilon - \epsilon_{res} \ll E_0$. This is also called the single-channel approximation region because here, both the scattering and the bound-state solutions behave exactly as if the single open-channel potential on its own had been adjusted to allow a new bound-state to appear near dissociation, without any closed-channel potential being involved. Feshbach resonances with $\zeta \gg 1$ are called open-channel dominated, while those with $\zeta \ll 1$ are called closed-channel dominated.

3.4 The Asymptotic Bound-State Model

Even though interaction potentials between real atoms (such as those described in Section 2.2) are much more complicated than the two coupled square wells model from Section 3.3, the question of how Feshbach resonances occur for a given atom pair can still be simplified to

be one that depends on the same three parameters from before: the background scattering length a_{bg} of the open-channel scattering potential, the initial, zero-field energy offset ϵ_0 of the closed-channel bound-state responsible for causing the Feshbach resonance, and the coupling matrix element U_1 between the open and closed channels. These are the ingredients of the asymptotic bound-state model, which is a simple yet accurate way of describing the Feshbach resonances of a particular atom pair.¹

For accurate predictions of Feshbach resonance locations, the only required ingredient is the free parameter ϵ_0 . Then, using the Breit-Rabi formula for the interaction of atoms with an external magnetic field [Steck, 2010], we can immediately predict the magnetic fields at which the closed-channel bound-state will intersect the open-channel asymptote (Fig. 3.7). Here we are assuming that the magnetic field B has a vanishing perturbation on the shape of molecular potentials describing interacting atom pairs, and only shifts their asymptotes in energy. This is a good assumption because Zeeman-shift energy scales are much smaller than those of molecular potentials.

The main difference between the toy model in Fig. 3.7a and the realistic model in Fig. 3.7b is a more elaborate treatment of the closed-channel bound-states that are responsible for producing Feshbach resonances. Taking into account hyperfine structure and shifts with magnetic field, the full interaction Hamiltonian for an atom pair in their electronic ground states can be written as

$$\begin{aligned}
 H &= V(r) + H_{\text{hf}} + H_z & (3.18) \\
 V(r) &= \frac{1}{4} [V_s(r) + 3V_t(r)] + [V_t(r) - V_s(r)] \vec{s}_a \cdot \vec{s}_b \\
 H_{\text{hf}} &= A_{\text{hf},a} \vec{i}_a \cdot \vec{s}_a + A_{\text{hf},b} \vec{i}_b \cdot \vec{s}_b \\
 H_z &= \gamma_e (\vec{s}_a + \vec{s}_b) \cdot \vec{B} - \gamma_{N,a} \vec{i}_a \cdot \vec{B} - \gamma_{N,b} \vec{i}_b \cdot \vec{B} & (3.19)
 \end{aligned}$$

where the complex form of $V(r)$ reduces to the triplet potential $V_t(r)$ for any triplet state,

¹This model is explained in great detail in [Tiecke *et al.*, 2010], [Tiecke, 2009], and [Walraven, 2010], with the latter two sources being more pedagogical in nature

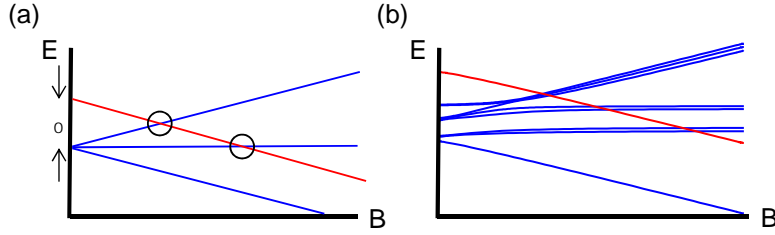


Figure 3.7: Asymptotic bound-state model for Feshbach resonances. The locations of Feshbach resonances for an atom pair can be predicted with only the zero-field energy ϵ_0 of the closed-channel bound-state as a free parameter. (a) In this toy model, two spin-down atoms $m_S = -1$ in the open-channel (red) can be coupled to another spin-triplet closed-channel bound-state with some zero-field energy offset ϵ_0 (blue). The $m_S = 1$ and $m_S = 0$ spin projections of the closed-channel intersect with the open-channel at magnetic field values B that can be predicted with the Breit-Rabi formula for the interaction of atoms with an external magnetic field. (b) A realistic model includes all the hyperfine states within the molecular vibrational level that have the correct quantum numbers to couple to the open-channel. These hyperfine states are also split by couplings to one another. In this model, a measurement of the location of the lowest field resonance immediately fixes ϵ_0 , and thus the locations of all the other resonances

and to the singlet potential $V_s(r)$ for any singlet state. The asymptotic bound-state model considers only the least bound states of $V_t(r)$ and $V_s(r)$ rather than the full potentials. The atomic hyperfine constants are written as $A_{hf,a/b}$, while γ_e and $\gamma_{N,a/b}$ are the electronic and nuclear gyromagnetic ratios respectively.

The hyperfine coupling term H_{hf} is the coupling term connecting open and closed channels. It connects the open-channel scattering state to any closed-channel bound-state that has the same total spin-projection $m_F = m_S + m_{i,a} + m_{i,b}$ [Walraven, 2010]. Thus, within the same least-bound vibrational state in the spin-triplet potential, there are many hyperfine states that can produce Feshbach resonances in the open channel. The energies of these hyperfine states with increasing magnetic field B is described by the usual interplay between H_{hf} and H_z . States from within the spin-singlet potential can also have the same overall projection m_F as the open-channel and be responsible for producing Feshbach resonances. These spin-singlet hyperfine states do not shift in energy with magnetic field B , except at places where they intersect spin-triplet bound states. There, the same coupling term H_{hf} produces avoided crossings between singlet and triplet states, perturbing both in ways must

be accounted for in quantitative predictions of Feshbach resonance locations. Appendix A includes a concrete example of how one takes into account the energy shifts and couplings for all the hyperfine states responsible for producing Feshbach resonances for an atomic pair, and make quantitatively accurate predictions of Feshbach resonance locations.

In addition to predicting the locations of Feshbach resonances, the asymptotic bound-state method can also describe resonance widths. These depend on the coupling matrix element U_1 between open and closed channels. The part of U_1 that depends on the electronic states of the atom pair is fixed by Eq. 3.18. To obtain the radial wave function overlap, the asymptotic bound-state model assumes that the overlap has negligible contribution from the short-range part of the closed-channel wave function. Thus, we can replace the detailed closed-channel wave function with that of a halo dimer $e^{-2\mu\sqrt{\epsilon_b}r/\hbar^2}$, where ϵ_b is the closed-channel binding energy (to be distinguished from ϵ_0). The overlap with the open-channel is then one that depends on the amplitude of the open-channel scattering wave function near $r = 0$, which, as discussed in Section 3.2, depends on a_{bg} . Thus, the strongest Feshbach resonances are the ones with large scattering length already in the open-channel alone.

3.5 Molecule Formation around a Feshbach Resonance

Around a Feshbach resonance, the combination of an adjustable detuning ϵ and a coupling matrix element U_1 between the closed-channel bound-state and the open-channel scattering state means that a separated atom pair in the open-channel can be adiabatically converted into a bound molecular state in the closed-channel in a manner analogous to a Landau-Zener crossing. In a two-level Landau-Zener problem, two states, $|1\rangle$ and $|2\rangle$, are coupled by a matrix element $U_1 = \hbar\Omega$, resulting in the Hamiltonian H given in Fig. 3.8. As the detuning ϵ between the two states is adiabatically varied across the resonance at $\epsilon = 0$, the system follows the dressed eigenstates of H , converting the $|1\rangle$ state to $|2\rangle$, and vice versa. The region in ϵ over which the dressed states contain a significant admixture of both basis states has width $\sim \hbar\Omega$, and the condition for adiabaticity is that ϵ is varied over this region in a

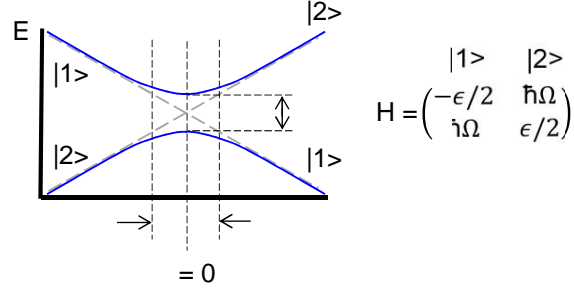


Figure 3.8: In a two-level Landau-Zener crossing, the states $|1\rangle$ and $|2\rangle$ are coupled by Ω . If the detuning ϵ is adiabatically varied across the $\epsilon = 0$ resonance, the system follows the dressed eigenstates (blue), converting $|1\rangle$ to $|2\rangle$, and vice-versa

time much longer than $1/\Omega$, with Ω being referred to as the Rabi frequency. Quantitatively, the probability of conversion is [Steck, 2010]

$$P = 1 - \exp\left(\frac{-\pi}{2} \frac{\hbar\Omega^2}{|d\epsilon/dt|}\right) = 1 - \exp(-2\pi\delta_{LZ}) \quad (3.20)$$

where $\delta_{LZ} = \hbar(\Omega/2)^2/|d\epsilon/dt|$ is called the Landau-Zener parameter, and $d\epsilon/dt$ is adiabatic for $\delta_{LZ} \gg 1$

In the case of a Feshbach resonance, the analogous avoided crossing is between the open-channel separated atom pair and the closed-channel bound-state (as explained in Section 3.3). Thus, when the magnetic field B is adiabatically varied across the resonance, atom pairs are converted into closed-channel bound molecules. The main distinction is that for a Feshbach resonance, the open-channel consists of a continuum of scattering states. This means that, while in the two-level Landau-Zener problem, there is an equal admixture on resonance of the two uncoupled states, for a Feshbach resonance the corresponding eigenstates are entirely open-channel on resonance.

In order to determine what the value of $|dB/dt|$ required for adiabaticity, we need to know the analogous Landau-Zener parameter δ_{LZ} . The Landau-Zener problem for an atom pair near a Feshbach resonance has been solved exactly for homonuclear pairs at zero

temperature [Köhler *et al.*, 2006]. For a pair of atoms in a box of volume V

$$\delta_{\text{LZ}} = \frac{1}{V} \frac{2\pi\hbar}{\mu} \left| \frac{a_{\text{bg}}\Delta B}{dB/dt} \right| \quad (3.21)$$

where μ is the reduced mass of the pair and the $1/V$ factor comes from the normalization of free-particle plane-wave solutions [Chwedeńczuk *et al.*, 2004; Cumby *et al.*, 2013]. This is then generalized to a uniform density of atoms n Köhler *et al.* [2006]

$$\delta_{\text{LZ}} = n \frac{2\pi\hbar}{\mu} \left| \frac{a_{\text{bg}}\Delta B}{dB/dt} \right| \quad (3.22)$$

where $n = N/V$ is the density, and represents the fact that each atom now has N equally likely pairing partners.

For heteronuclear atom pairs at finite temperature, the situation is complicated by reduced phase-space overlap between the different atomic species. At higher temperatures, an atom is less likely to find a partner close enough in phase space to form a molecule [Hodby *et al.*, 2005]. Moreover, for a heteronuclear atom pair, the different trapping frequencies of different atoms further reduces phase space overlap [Deuretzbacher *et al.*, 2008], as does spatial separation in a Bose-Fermi mixture below the condensation temperature T_{BEC} for the bosonic component [Cumby *et al.*, 2013]. However, if we still naively apply Eq. 3.22 to a heteronuclear atom pair and just take n to be the larger of the two component densities, we obtain a generous upper bound on δ_{LZ} for a particular magnetic field sweep dB/dt . In practice, experimental magnetic field sweeps to form molecules fall in the range $\delta_{\text{LZ}} \sim 0.1$ to 1, as shown in Table 3.1,² meaning that the prediction in Eq. 3.22 is useful for providing an initial target dB/dt for successful molecule formation.

²Entries for ΔB and a_{bg} obtained from [Chin *et al.*, 2010], except those for ${}^6\text{Li}{}^{40}\text{K}$, which are obtained from [Wille *et al.*, 2008]. Experimental parameters obtained from [Xu *et al.*, 2003] for Na_2 ; [Greiner *et al.*, 2003] for K_2 ; [Hodby *et al.*, 2005], [Dürr *et al.*, 2004], and [Syassen *et al.*, 2006] for Rb_2 ; [Herbig *et al.*, 2003] for Cs_2 ; [Papp and Wieman, 2006] for ${}^{85}\text{Rb}{}^{87}\text{Rb}$; [Spiegelhalder *et al.*, 2010] for LiK ; and [Zirbel, 2008] for KRb

Resonance	ΔB (G)	a_{bg} (a_0)	n_{exp} (cm^{-3})	dB/dt (G/ms)	E_0 (kHz)	E_F (kHz)	Ω (kHz)	$\delta_{\text{LZ}}^{\text{exp}}$
907 G $^{23}\text{Na}_2$	1	63	1.7×10^{14}	100	180	6.6	14	0.39
202 G $^{40}\text{K}_2$	8	174	1.4×10^{13}	25	3.3×10^4	3.8	33	1.6
155 G $^{85}\text{Rb}_2$	11	440	10^{11}	10	1.5×10^6	1.8	50	0.05
1007 G $^{87}\text{Rb}_2$	0.2	100	5×10^{14}	10	37	1.8	3.5	0.97
20 G $^{133}\text{Cs}_2$	0.005	160	10^{13}	0.05	0.0038	1.1	0.25	0.1
265 G $^{85}\text{Rb}^{87}\text{Rb}$	1	213	7×10^{12}	2.2	2.1×10^3	1.8	9.6	0.66
372 G $^{85}\text{Rb}^{87}\text{Rb}$	6	213	7×10^{12}	14	7.7×10^4	1.8	24	0.63
168 G $^6\text{Li}^{40}\text{K}$	0.08	60	2×10^{12}	0.23	0.13	15	4.2	0.34
546 G $^{40}\text{K}^{87}\text{Rb}$	3	189	8×10^{12}	7	1.3×10^4	2.8	21	1

Table 3.1: Generalized Landau-Zener parameters from various molecule formation experiments. The entries under ΔB , a_{bg} , n_{exp} , and dB/dt are obtained from the sources given in the text. The entries under E_0 , E_F , Ω , and $\delta_{\text{LZ}}^{\text{exp}}$ are calculated based on the outlined theory. For heteronuclear atom pairs, n_{exp} is taken to be the smaller of the two component densities.

The expression in Eq. 3.22 can be rewritten as a combination of energy scales

$$\delta_{\text{LZ}} = \frac{\hbar\Omega^2}{\text{d}\epsilon/\text{d}t} \quad (3.23)$$

where $\Omega = \frac{1}{\hbar}\sqrt{\tilde{E}_F^{3/2}E_0^{1/2}/3\pi}$ is the Rabi frequency for atom-molecule coupling, E_0 is as given in Section 3.3, and $\tilde{E}_F = (6\pi^2n)^{3/2}\hbar^2/\mu$ is the effective Fermi energy, which expresses the atomic density n in energy units for bosons as well as for fermions.

There are a number of additional techniques of forming molecules around a Feshbach resonance that are not directly relevant to the experiments described later in this dissertation. Two of these are radio-frequency association [Zirbel *et al.*, 2008b], and modulation of the magnetic field at a frequency resonant with the molecular binding energy [Thompson *et al.*, 2005]. Both require the target molecular bound-state to be open-channel-dominated. Photoassociation is a third technique for forming molecules out of ultracold atoms [Jones *et al.*, 2006]. I will describe this technique in greater detail in Section 6.2 in the context of future efforts deriving from the work in this dissertation. For now, it is sufficient to mention that the efficiency of photoassociation depends on the overlap of the open-channel scatter-

ing wave function and a short-range electronically excited bound-state wave function. As discussed in Section 3.2, this overlap can be enhanced near a scattering resonance.

3.6 The BEC-BCS Crossover

The first signature of Feshbach resonances in ultracold atoms was dramatically enhanced inelastic collision rates in bosonic ^{23}Na , leading to strong loss at specific magnetic fields [Inouye *et al.*, 1998]. This is because, where the two-body scattering length a is enhanced, three-body inelastic collision rates are enhanced even more [D’Incao and Esry, 2005], leading to rapid loss of the ultracold atom sample near a Feshbach resonance. This loss happens via a process called three-body recombination, in which a collision involving three atoms leaves two of them in a bound state, and the binding energy is released as kinetic energy of the collision products.

Thus, it was only with the arrival of ultracold fermionic atoms that Feshbach resonances became more than just a way of tuning three-body loss [Ketterle and Zwierlein, 2008]. A pair of fermions in different internal states can collide via s-wave scattering. Near a Feshbach resonance, where the scattering length a diverges, the fermion pairs exist in a BCS-like paired state on the $a < 0$ side, where the effective pseudo-potential interaction (given in Section 3.2) is strongly attractive, and as a Bose-Einstein condensate of bound halo dimers on the $a > 0$ side (Fig. 3.9). The entire region near resonance is then called the BEC-BCS crossover.

Three-body recombination is suppressed in such a system, because it would require a collision between at least two fermions in the same internal state. In the limit of zero temperature, this is forbidden by the quantum statistics, and in general the process is suppressed by $(kR_e)^\gamma$, where R_e is characteristic spatial extent of the product bound-state in decay by three-body recombination, and γ is some numerical factor greater than one [Petrov *et al.*, 2004]. Since typical de-Broglie wavelengths are $\sim 1 \mu\text{m}$ for ultracold atoms while $R_e \sim 50a_0$, this means $(kR_e)^\gamma$ is vanishingly small for ultracold fermions. In the case

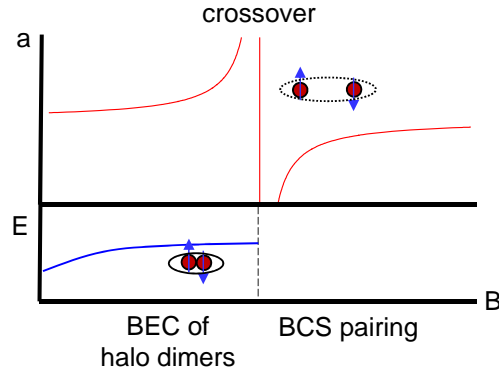


Figure 3.9: The BEC-BCS crossover in an ultracold gas of fermions. A gas consisting of ultracold fermions in two different internal states exists near a Feshbach resonance as a BCS-like paired state on the $a < 0$ side, and as a Bose-Einstein condensate of bound halo dimers on the $a > 0$ side. Decay via three-body recombination is suppressed by quantum statistics even in the presence of diverging a .

of halo dimers on the $a > 0$ side of the Feshbach resonance, their formation is not suppressed by quantum statistics because of their large spatial extent as a diverges. However, decay of these pairs to more deeply bound states by an inelastic collision with another pair or a free atom is still suppressed by the same mechanism as above.

Consequently, in ultracold Fermi gases, Feshbach resonances become a knob that allows interparticle interactions to be tuned to arbitrary values. This has resulted in the demonstration of high-temperature superfluidity of BCS-paired fermions (at a significant fraction of the Fermi temperature T_F) as well as Bose-Einstein condensation of weakly bound halo dimer molecules [Ketterle and Zwierlein, 2008].

Chapter 4

Formation of $^{23}\text{Na}^6\text{Li}$ Molecules

In this chapter I will describe one of the two main scientific contributions of this dissertation, the successful formation of $^{23}\text{Na}^6\text{Li}$ molecules around a Feshbach resonance at 745 G after extensive previous efforts proved to be unsuccessful [Christensen, 2011]. In Section 4.1, I will explain how the previous unsuccessful attempts at molecule formation were due to an incorrect assignment of the Feshbach resonances in the $^6\text{Li}+^{23}\text{Na}$ system. This is followed by a brief description in Section 4.2, of the apparatus used for molecule formation experiments. The procedure for successful molecule formation is explained in Section 4.3, and the chapter concludes in Section 4.4 with a discussion of the lifetime of NaLi molecules against collisional decay. The work described in this chapter has been published in [Heo *et al.*, 2012].

4.1 Revised Assignment of Feshbach Resonances

Feshbach resonances in the $^6\text{Li}+^{23}\text{Na}$ system were the first ever observed between atoms of two different species [Stan *et al.*, 2004]. A characteristic fingerprint of three closely spaced resonances was obtained for magnetic fields of 746 G, 760 G and 796 G, for Li in $|m_s m_i\rangle = |-1/2 1\rangle$ and Na in $|-1/2 3/2\rangle$. These were assigned to be resonances produced by the least-bound vibrational state of the spin-triplet potential with spin projection $m_S = 1$. As described in Appendix A, there are precisely three molecular hyperfine states with the right quantum numbers to couple to the open-channel atoms, and by choosing the triplet

and singlet binding energies to be $E_1 = 5710$ MHz and $E_0 = 4245$ MHz respectively, the locations of the resonances can be reproduced by the asymptotic bound-state model from Section 3.4. This assignment was confirmed by a full coupled-channels calculation [Gacesa *et al.*, 2008], which assigned a background scattering length of $a_{\text{bg}} = 14a_0$ and $\Delta B = 0.04$ G, 0.3 G and 2 G for each of the resonances, or $E_0/h = 3$ Hz, 180 Hz and 8 kHz if we use the energy scale E_0 from Section 3.3 characterizing the width of the open-channel-dominated region around resonance.

An earlier effort to produce NaLi molecules using this assignment of Feshbach resonances was unsuccessful despite an exhaustive search across all experimentally feasible resonance locations and for a wide range of magnetic field sweep rates [Christensen, 2011]. The reason for this turned out to be an incorrect assignment of Feshbach resonances by [Stan *et al.*, 2004] and [Gacesa *et al.*, 2008]. As illustrated in Fig. 4.1, the revised assignment found that the previously observed Feshbach resonances below 800 G were in fact produced by weak dipole-dipole coupling of the unpaired electron spins in the colliding atoms [Schuster *et al.*, 2012]. This dipole-dipole coupling has an angular dependence (Section 2.6) that allows mixing of partial waves, such that the s-wave open-channel wave function can couple to d-wave, or $J = 2$ closed-channel molecular bound states with two units of rotational angular momentum. Under the revised assignment, there is a far greater multiplicity of states with hyperfine and rotational projection quantum numbers to couple to the open-channel. In particular, there are eleven states in total with $m_S = 1$ that intersect in energy with the open-channel near 800 G, and it is sheer coincidence that only three of them can be readily observed experimentally, producing the deceptive fingerprint of resonance locations that mimicked the case of typical hyperfine-induced Feshbach resonances. It was only by identifying the locations of resonances at higher magnetic fields B that a strong discrepancy emerged [Christensen, 2011; Schuster *et al.*, 2012], confirming that the revised assignment does indeed more correctly describe the Feshbach resonances in the system.

Note that there are still Feshbach resonances produced by s-wave, $J = 0$ closed-channel bound states via the more typical mechanism of hyperfine coupling. However, these states

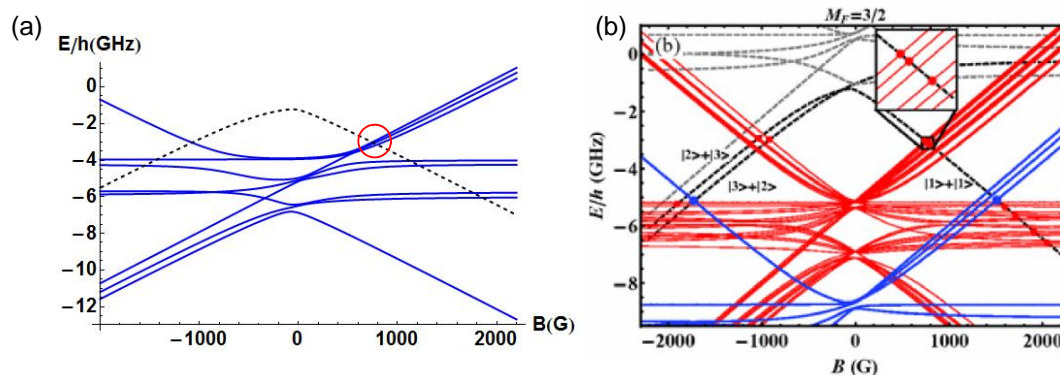


Figure 4.1: Revised assignment of $^6\text{Li}+^{23}\text{Na}$ Feshbach resonances. (a) In the original assignment, the three observed resonances were assigned to the $m_S = 1$ projection of the least-bound vibrational state of the spin-triplet potential, with three hyperfine states having the right quantum numbers to couple to the open-channel (circled). The variation of the open-channel energy with magnetic field B is shown as a black dashed curve, while the bound-state energies are in blue. (b) In the revised assignment, resonances below 1000 G are produced by weak dipole-dipole coupling, which couples the s-wave scattering in the open-channel to d-wave, or $J = 2$ closed-channel molecular bound states with two units of rotational angular momentum. Compared to the typical hyperfine coupling, this results in a much larger multiplicity of states with the right hyperfine and rotational quantum numbers (red) to couple to the open channel (black, dashed). The closed-channel bound states corresponding to the typical, hyperfine coupled Feshbach resonances are still present (blue), but these are much more deeply bound than previously assumed. The plot in (b) was taken from [Schuster *et al.*, 2012]

are much more deeply bound than previously thought, and thus produce resonances at magnetic fields $B > 1000$ G that are at the edge of what our experimental apparatus (Section 4.2) can access. The binding energies for the triplet and singlet states, as derived from the revised resonance assignments, are $E_1 = 9353$ MHz and $E_0 = 9384$ MHz respectively [Schuster *et al.*, 2012]. From Table 2.1, it becomes obvious that the unusual scenario of dipole-dipole coupled Feshbach resonances in Li+Na is specific to systems with small reduced mass μ . For combinations of heavier atoms, such as K+Rb, the near-dissociation vibrational level spacing is small enough such that there will always be the typical, hyperfine-induced Feshbach resonances with range of experimentally achievable fields.

As a result of the revised assignments, the background scattering length is now $a_{\text{bg}} = 76a_0$, with $E_0/h = 6$ Hz, 2×10^{-5} Hz and 0.015 Hz for each of the three resonances at 745 G, 759 G and 795 G. The strongest resonance from the revised assignment is at 746 G, with an $E_0/h = 5$ Hz that is three orders of magnitude smaller than for the earlier assignment, where the strongest resonance at 790 G had $E_0/h = 8$ kHz. This small E_0 results in a uniquely challenging situation for molecule formation. Molecule formation experiments with other comparably weak resonances have been done, but at much lower fields, for example Cs₂ [Herbig *et al.*, 2003] and $^6\text{Li}^{40}\text{K}$ [Spiegelhalder *et al.*, 2010]. Thus, the combination of extraordinarily weak coupling, at high magnetic field, in a mixture of two atomic species makes this perhaps the most difficult Feshbach resonance around which molecule formation has been successful.

The bound-state open-channel character only for magnetic fields B around resonance B_{res} such that $B - B_{\text{res}} < E_0/\Delta\mu = 2 \mu\text{G}$ (Section 3.3). This is impossible to resolve experimentally, and precludes molecule formation via radio-frequency association [Zirbel *et al.*, 2008b] or modulation of the magnetic field at a frequency resonant with the molecular binding energy [Thompson *et al.*, 2005], both of which require a large open-channel contribution for good wave-function overlap between atomic and molecular states. This leaves magnetic field sweeps across resonance as the only feasible approach.

4.2 Experimental Machinery

The machine we use to produce an ultracold mixture of ^6Li and ^{23}Na atoms for molecule formation experiments has been described in great detail elsewhere.¹ In brief, we produce a near-degenerate mixture of ^{23}Na atoms in the $^2S_{1/2} |F, m_F\rangle = |2, 2\rangle$ state and ^6Li atoms in the $^2S_{1/2} |3/2, 3/2\rangle$ state in a cloverleaf magnetic trap, by evaporatively cooling ^{23}Na with radio-frequency spin flips $|2, 2\rangle \rightarrow |1, 1\rangle$ tuned to be in resonance with the Zeeman shifted frequencies of atoms at the very edges of the magnetic trap. The ^6Li atoms are sympathetically cooled by thermalizing collisions with the ^{23}Na . At the end of evaporation, the Li+Na mixture is transferred into a 5-W single-beam optical dipole trap at 1064 nm. In the optical trap we spin-flip both species with simultaneous Landau-Zener radio-frequency sweeps at a small bias field of 15 G to the hyperfine ground states Na $|1, 1\rangle$ and Li $|1/2, 1/2\rangle$. Note that whereas at low fields $|F, m_F\rangle$ is a good basis, at higher fields, when the Zeeman shift becomes larger than the hyperfine splitting, a good basis becomes $|m_s, m_i\rangle$. The hyperfine ground states at high field are thus Na $|-1/2, 3/2\rangle$ and Li $|-1/2, 1\rangle$. These are sometimes written simply as Na $|1\rangle$ and Li $|1\rangle$.

With a Li+Na mixture confined in an optical dipole trap, we use a set of Helmholtz coils to produce the large, uniform magnetic bias fields required to reach the nearest Feshbach resonances. The narrowness of the resonances in Li+Na places stringent demands on magnetic field stability for molecule formation. Experimentally we achieve <10 mG root-mean-square (rms) magnetic field noise. The power supply produces current fluctuations corresponding to 200 mG of noise at 745 G. Active feedback stabilization of the current reduces the noise to < 10 mG rms after synchronizing experimental sequences with the 60-Hz line frequency. Further details on the magnetic field stabilization in our experiment can be found in [Christensen, 2011].

¹The original construction of the ultracold atoms machine as a Na Bose-Einstein condensate experiment is described in [Chikkatur, 2002], with further details found in [Pasquini, 2007] and Shin [2006]. The machine was later upgraded to be a dual-species, $^{23}\text{Na} + ^6\text{Li}$ apparatus, based on the original design in [Hadzibabic, 2003]. Details for the various components of the upgraded machine can be found in [Jo, 2010], [Christensen, 2011], [Lee, 2012], and [Notz, 2014]

For the rest of the experiments described in this chapter, we work around the strongest of the experimentally accessible Feshbach resonances, at 745 G. From low magnetic field, we first jump far above resonance to 752 G, and after waiting 200 ms the mixture is evaporatively cooled by lowering the intensity of the trapping beam, leaving 1×10^6 each of Na and Li at a temperature of $1.2 \mu\text{K}$. Here, the weak magnetic field curvature along the optical dipole trap provides additional axial confinement, giving radial and axial trap frequencies (ν_r, ν_z) of (920 Hz, 13 Hz) for Na, and (2.0 kHz, 26 Hz) for Li. The temperature of the mixture is near the onset of condensation for the bosonic Na, with $T/T_c = 1.2$, and $T/T_F = 0.3$, where for our trap parameters the condensation temperature for Na is $T_c = 1.0 \mu\text{K}$ and the Fermi temperature for Li is $T_F = 4.1 \mu\text{K}$. The peak in-trap densities are $2.5 \times 10^{13} \text{ cm}^{-3}$ for Na and $1.4 \times 10^{13} \text{ cm}^{-3}$ for Li.

The precise location of the 745 G resonance is determined by jumping down to 745.9 G, waiting 15 ms for the field to stabilize, and then sweeping the magnetic field down at a constant rate of 50 mG/ms but with a variable end-point. The total atom number remaining after the sweep drops sharply as the end-point crosses the Feshbach resonance (Fig. 4.2). This measurement determines the location of the Feshbach resonance to be 745.38 ± 0.04 G, providing a precise target field for molecule formation sweeps. Note the 40 mG width from Fig. 4.2 is not directly related to E_0 , Ω or ΔB , but is composed of a number of contributions, including three-body loss due to scattering length enhancement, adiabatic molecule formation, and limitations in magnetic field control.

4.3 Molecule Formation

The experimental sequence we used for successful formation of NaLi is shown in Fig. 4.3. The start and end points of the magnetic field sweep are chosen to be as close to resonance as possible while still being outside the region of atom-molecule coupling defined by Ω in Section 3.5. This maximizes the formation efficiency, because molecules form and begin to decay immediately after crossing the coupling region around resonance. The initial sweep

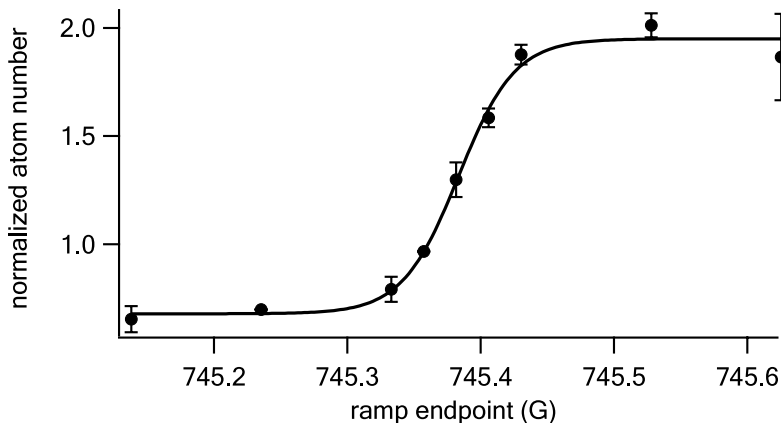


Figure 4.2: Determination of Feshbach resonance location. Shown is the remaining atom number as a function of the endpoint of a downward magnetic field sweep across resonance. Results are fitted to a hyperbolic tangent function (solid line) with center 745.38 G and width 40 mG. The normalized atom number along the vertical axis is a sum of Na and Li atom numbers, each normalized to 1.

rate was chosen to correspond to $\Delta_{LZ} = 0.1$, which is large enough to result in significant adiabatic conversion of atom pairs into molecules, but not too large such that in the time it takes to complete the sweep, molecules will already decay and be lost via collisional processes.

At the end of the sweep, laser pulses resonant with the $589\text{ nm } ^2S_{1/2} | -1/2, 3/2 \rangle \rightarrow ^2P_{3/2} | -3/2, 3/2 \rangle$ transition in Na and the $671\text{ nm } ^2S_{1/2} | -1/2, 1 \rangle \rightarrow ^2P_{3/2} | -3/2, 1 \rangle$ transition in Li remove essentially all of the remaining free atoms from the trap. For closed-channel Feshbach molecules, the excitation spectrum is sufficiently different from free atoms, so NaLi molecules are mostly unaffected if the laser pulses are not too long. After a variable hold time for molecule lifetime measurements, the field is switched above resonance, where bound molecules rapidly dissociate [Mukaiyama *et al.*, 2004]. Imaging the free atoms gives us a measure of the molecule number, which for our optimized sweep parameters gives a formation fraction of 5%. This corresponds to a molecule number of 5×10^4 .

To confirm that the detected atomic signal is indeed from dissociated molecules, we check that imaging while keeping the magnetic field below resonance gives a negligible signal

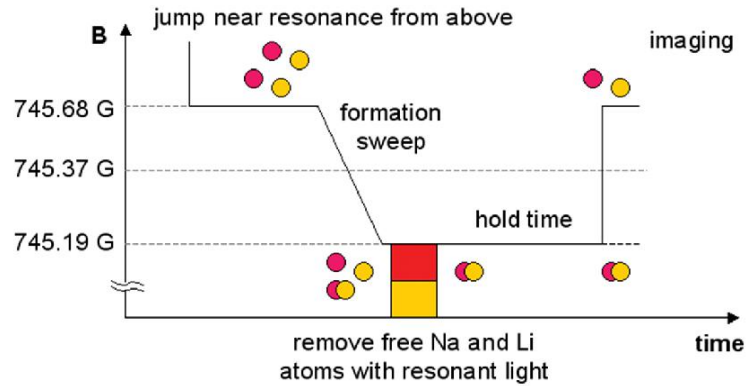


Figure 4.3: Experimental sequence for molecule formation. After waiting for the magnetic field B to stabilize at 745.68 G, we sweep the field across resonance to $B = 745.19$ G in $800 \mu\text{s}$, at a constant rate of 600 mG/ms. At the end of the sweep, simultaneous pulses of resonant light remove Na and Li atoms from the trap within $100 \mu\text{s}$ while leaving molecules unaffected. After a variable hold time for lifetime measurements, molecules are detected by jumping back above resonance and imaging dissociated atoms. The magnetic field can also be kept below resonance to confirm that bound molecules are invisible to the imaging light.

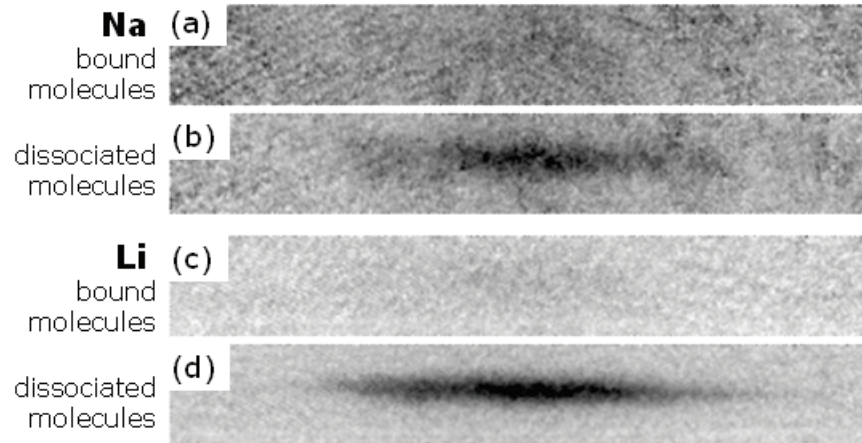


Figure 4.4: Absorption imaging of molecular clouds using dissociated Na (a, b) and Li atoms (c, d). The lower images in each pair (b, d) are taken after switching above resonance and dissociating molecules into free atoms. The upper images (a, c) are reference images with the field below resonance, where free atoms have been removed from the trap and the molecules are invisible to the imaging light.

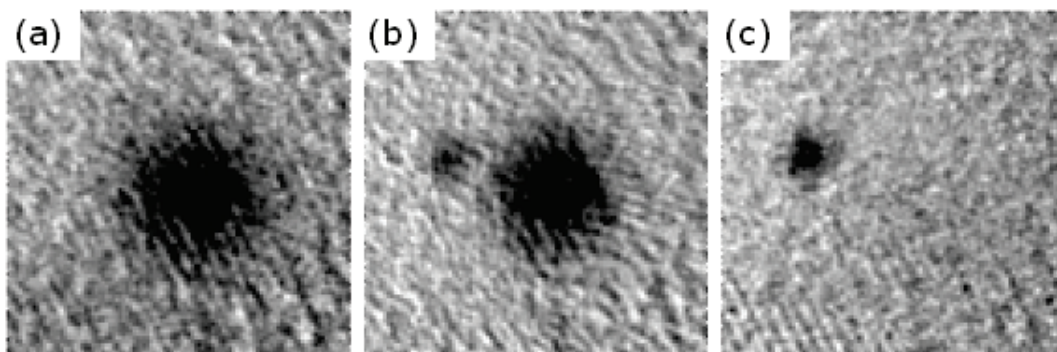


Figure 4.5: Separation of atoms and molecules in a magnetic field gradient. Absorption images of (a) free Li atoms, (b) separated clouds of atoms and dissociated molecules, and (c) molecules with free atoms removed, taken 3 ms after release from the crossed optical dipole trap in a 6 G/cm gradient.

(Fig. 4.4). Below resonance, bound molecules have a vanishing absorption cross section σ and are invisible to the imaging light, while for free atoms σ is nearly identical to above resonance because the Zeeman shift produced by magnetic field changes of ~ 500 mG is much smaller than the atomic linewidth. A second, independent confirmation of the molecular signal comes from releasing the trapped mixture in a magnetic field gradient, and demonstrating that the expanding atomic and molecular clouds separate from one another (Fig. 4.5) because of their differential magnetic moment $\Delta\mu$. To observe this separation, we added additional optical confinement along the magnetic field gradient direction, using a second beam to form a crossed-beam optical dipole trap.

The Landau-Zener parameter in our experiment is estimated from Eq. 3.23 to be $\delta_{\text{LZ}} = 0.13$ by choosing n to be the larger of n_{Na} and n_{Li} . This corresponds to a formation efficiency of 56%. The discrepancy with the observed molecule fraction of 5% has several explanations. The simplified Landau-Zener picture in Section 3.5 assumes full phase space overlap between the atoms involved in molecule formation, which is only true in a Bose-Einstein condensate at $T = 0$ Hodby *et al.* [2005]; Williams *et al.* [2006]. In a Bose-Fermi mixture like NaLi, the phase space overlap is lower, reaching a maximum around the boson condensation temperature T_c because at lower T the Na condensate begins to have less spatial overlap with the fermionic Li Zirbel *et al.* [2008b]. The phase-space overlap between

Na and Li is further reduced because of their different trapping potentials Deuretzbacher *et al.* [2008]. Finally, NaLi molecules will form and begin to decay as soon as the magnetic field crosses resonance. However, due to limitations in magnetic field control, we must take 800 μs to complete the sweep, meaning that a significant fraction of the molecules formed after crossing resonance will be lost in the remainder of the sweep. We will discuss the lifetime of NaLi molecules in Section 4.4.

4.4 Optimizing Decay Lifetime

The lifetime of trapped NaLi molecules (Fig. 4.6) can be measured by varying the hold time before switching the magnetic field above resonance for dissociation and imaging. With $> 90\%$ of both species of remaining atoms removed, the molecular lifetime is 1.3 ms. This lifetime appears to be limited by collisions with other molecules or leftover atoms rather than by photon scattering, since it does not increase significantly with reduced intensity of the trapping laser. It can be enhanced by suppressing molecule-molecule collisions in a 3D optical lattice Chotia *et al.* [2012] and fully removing residual free atoms from the trap. The molecular lifetime drops to 270 μs when keeping free Na and Li atoms trapped with the molecules. Finally, if only Li atoms are removed before the hold time and not Na, the lifetime is 550 μs (not shown in Fig. 4.6).

The presence of free atoms increases the molecular decay rate because of inelastic collisions with molecules. Our lifetime measurements show that Na and Li each give comparable contributions to this increased decay, which is consistent with the constituent atoms in the closed-channel NaLi molecule being distinguishable from free Na and Li atoms, meaning that quantum statistics does not play a role in collisions. In contrast, experiments with open-channel KRb molecules [Zirbel *et al.*, 2008a] showed a sharp dependence of lifetime on the quantum statistics of the atomic collisional partner. The lifetimes above can also be reported as two-body loss-rate constants $\beta_{\text{NaLi+Na}} \sim 1 \times 10^{-10} \text{ cm}^3/\text{s}$ and $\beta_{\text{NaLi+Li}} \sim 4 \times 10^{-10} \text{ cm}^3/\text{s}$. We will treat two-body collisional loss of molecules in greater detail in Section 5.4.

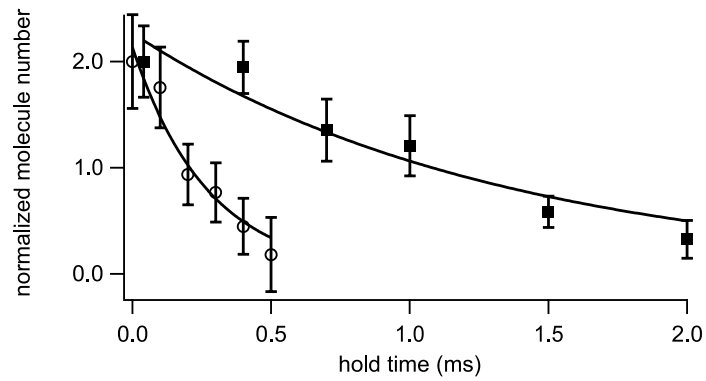


Figure 4.6: Lifetime of trapped NaLi molecules after removing remaining free Na and Li atoms from the trap (solid squares). Fitting to an exponential gives a decay time constant of 1.3 ms. For comparison, the lifetime without removing remaining free atoms from the trap is 270 μs (open circles). The normalized molecule number along the vertical axis is a sum of Na and Li atom numbers, each normalized to 1 at zero hold time, detected from dissociating bound NaLi molecules.

Chapter 5

Molecules of ${}^6\text{Li}_2$ Around a Narrow Feshbach Resonance

The contents of this chapter highlight the second scientific contribution of this thesis. Using the expertise in forming molecules around narrow Feshbach resonances from Chapter 4, we turned our attention to the narrow 543 G Feshbach resonance in ${}^6\text{Li}$. As explained in Section 5.1, there had been a decade-long puzzle about unexpectedly long-lived molecules formed around this resonance. Our experimental work, described in Section 5.2, conclusively resolved this puzzle. However, further measurements in Section 5.3 raised a new question of unexpected behaviour of Li_2+Li collisions, which, as discussed in Section 5.4, deviated sharply from the simple predictions of the quantum Langevin model. This observation is explained in Section 5.5, and represents the first example of collisions involving ultracold molecules explained by physics beyond universal long-range van der Waals interactions. The work described in this chapter has been published in [Wang *et al.*, 2013].

5.1 A Long-Standing Puzzle in ${}^6\text{Li}$

Before the experimental work described in this chapter, there had been a decade-long puzzle of unexpectedly long lifetimes of closed-channel ${}^6\text{Li}_2$ molecules formed around the narrow 543 G Feshbach resonance [Strecker *et al.*, 2003]. There are two experimentally accessible Feshbach resonances between fermionic ${}^6\text{Li}$ atoms in their two lowest hyperfine states (Fig. 5.1). One is an extremely wide, open-channel-dominated resonance at 832 G, with

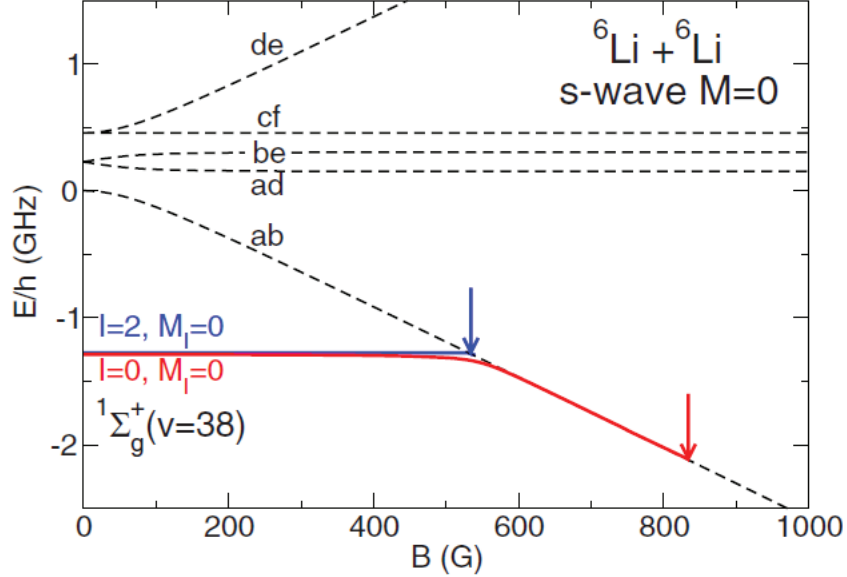


Figure 5.1: Feshbach resonances in ${}^6\text{Li}_2$. One resonance at 832 G (red) is extremely strong, with an open-channel-dominated region for the bound state that spans the entire 300-G range of scattering length enhancement. A second resonance at 543 G is much more modest, and arises from a bound-state that is only weakly coupled to the open-channel. This figure was taken from [Chin *et al.*, 2010]

$a_{\text{bg}} = -1405a_0$, $\Delta B = 300$ G, and an enormous $E_0/h = 10^{12}$ Hz, meaning that for $B < B_{\text{res}}$ the bound-state is open-channel dominated for the entire 300 G range of scattering length enhancement [Chin *et al.*, 2010]. The exceptional properties of this resonance arises from the very large background scattering length a_{bg} , indicating that the open-channel spin-triplet scattering potential is already near-resonant, being almost deep enough to have a new bound-state appear at dissociation. This produces the extremely strong coupling between the open and closed channels. The second resonance at 543 G is more modest, with $a_{\text{bg}} = 60a_0$, $\Delta B = 0.1$ G and $E_0/h = 240$ Hz. This is a closed-channel-dominated resonance, with there being a significant closed-channel component to the bound-state within 0.1 G of B_{res} .

The 832 G resonance in fermionic ${}^6\text{Li}$ is almost the perfect realization of the BEC-BCS crossover described in Section 3.6 [Ketterle and Zwierlein, 2008], with an open-channel-dominated region that spans essentially the entire 300-G range of scattering length enhance-

ment. The first, seminal reports of long lifetimes of bound fermion pairs near this resonance [Cubizolles *et al.*, 2003; Jochim *et al.*, 2003] were quickly explained, as in Section 3.6, in terms of Pauli suppression of collisions [Petrov *et al.*, 2004]. The other report, around the same time, of similarly long-lived bound ${}^6\text{Li}_2$ molecules around the narrow 543 G Feshbach resonance [Strecker *et al.*, 2003], outside the open-channel-dominated region, had remained unexplained in the decade since. Around such a narrow resonance, outside the small range in which the closed-channel bound-state is negligible, there should no longer be any Pauli suppression of collisions between fully closed-channel molecules. Having previously demonstrated the ability to form molecules around an exceptionally narrow Feshbach resonance in Chapter 4, we decided to revisit the work done around this comparatively much easier 543 G narrow resonance in ${}^6\text{Li}$. The idea was that if the closed-channel molecules were indeed long-lived for some as-of-yet unexplained reason, then they can be evaporatively cooled to achieve the first example of Bose-Einstein condensation of true closed-channel bound molecules, rather than of long-range halo dimers.

5.2 Molecule Formation Around the 543 G Narrow Resonance

The experimental apparatus used to perform molecule formation experiments in ${}^6\text{Li}$ is the same as the one highlighted in Section 4.2. We leave only a pure sample of ${}^6\text{Li}$ atoms at the end of evaporative cooling in the magnetic trap by ejecting all remaining Na atoms. The Li atoms are, as before, transferred into a single-beam optical dipole trap (ODT) with power 5 W and wavelength 1064 nm. In the ODT we spin-flip Li ($|F, m_F\rangle = |3/2, 3/2\rangle \rightarrow |1/2, 1/2\rangle$) with a Landau-Zener radio-frequency (rf) sweep at 15 G. Following this, an equal superposition of the two lowest Li hyperfine states $|1\rangle$ and $|2\rangle$ (corresponding to $|1/2, 1/2\rangle$ and $|1/2, -1/2\rangle$ at low field) is prepared by two partially adiabatic rf sweeps at 300 G, separated by 10 ms. After holding for a further 500 ms, the superposition becomes an incoherent mixture of $|1\rangle$ and $|2\rangle$. We then further evaporatively cool the Li to $T/T_F = 0.2$, and transfer the atoms into a second, more weakly confining single-beam ODT parallel to

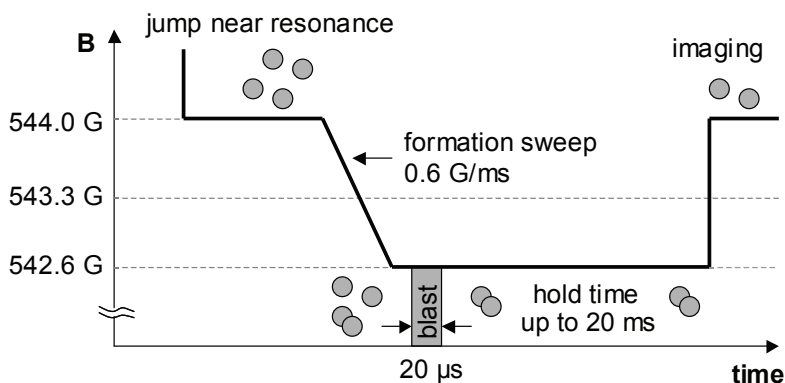


Figure 5.2: Experimental sequence for molecule formation. After jumping near the $B = 543$ G resonance from above, we sweep B at 0.6 G/ms across a region 1.4 G wide. Immediately after the sweep, a blast of resonant imaging light removes free Li from the trap, leaving a pure gas of Li_2 . After a variable hold time, remaining molecules are detected by jumping back above resonance and imaging dissociated free atoms. B can also be kept below resonance to confirm that Li_2 is invisible to imaging light.

the first one, with trap frequencies $(\nu_z, \nu_r) = (21, 480)$ Hz. Optimized formation of Li_2 is done in this second trap.

Molecules formed out of an incoherent mixture of Li $|1\rangle$ and $|2\rangle$ around the narrow 543 G resonance are in the highest vibrational state of the spin-singlet potential [Chin *et al.*, 2010]. The initial number in each of $|1\rangle$ and $|2\rangle$ states is 2×10^6 , corresponding to a peak density of $4 \times 10^{12} \text{ cm}^{-3}$. A magnetic field sweep across resonance (Fig. 5.2) converts the atoms into diatomic molecules.

As in Chapter 4, we unambiguously observe the signature of molecule formation by applying a short blast of resonant imaging light to remove free Li in the $|1\rangle$ state from the trap. The small mass of Li means that it will be ejected from the ODT after a single recoil, and moreover at 543 G the imaging transition is cycling, so a pulse duration of $20 \mu\text{s}$ is sufficient to leave no trace of $|1\rangle$ atoms in the trap. After the blast, imaging the $|1\rangle$ state while keeping B below resonance gives a negligible signal, since Li_2 is invisible to the imaging light here. After switching B above resonance to dissociate Li_2 , we image atoms in the $|1\rangle$ state as a measure of the molecule number, which for our optimized sweep parameters gives a formation fraction of 10% or a molecule number of 2×10^5 . A second,

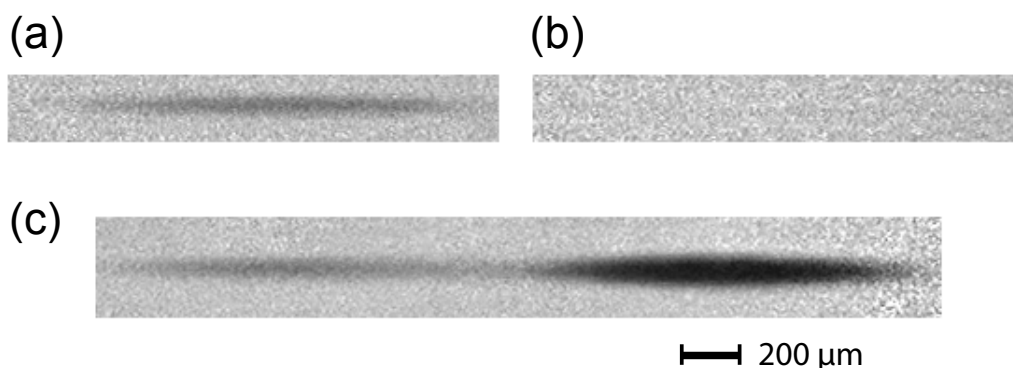


Figure 5.3: Absorption images of ${}^6\text{Li}_2$ molecules. Images of (a) molecules dissociated into free atoms above the 543 G Feshbach resonance, (b) molecules held below resonance where they are invisible to the imaging light, and (c) separation of molecules and atoms in magnetic field gradient.

independent confirmation of molecule formation is obtained by turning on a magnetic field gradient of 10 G/cm for 6 ms while holding in-trap below resonance, which pushes free Li atoms away while leaving the spin-singlet molecules unaffected (Fig. 5.3).

For molecule decay measurements, we use two consecutive blasts of imaging light, resonant with $|1\rangle$ and $|2\rangle$ respectively, to remove free atoms in both hyperfine states from the trap immediately after the molecule formation sweep. This leaves a pure sample of Li_2 molecules, which undergoes rapid initial decay from their vibrationally excited state, slowing down with increasing hold time in a way that is consistent with two-body decay from molecule-molecule collisions (Fig. 5.4). The non-exponential nature of the observed decay rules out that our lifetimes are limited by off-resonant excitations from the trapping laser, and we have also checked, by holding molecules in trap at up to 8 G below resonance, that decay rates outside the coupling region around resonance are independent of magnetic field, as expected.

Our measurements demonstrate conclusively that the lifetime of these closed-channel molecules is in fact short, as expected in the absence of the effects of quantum statistics. Compared to the previous work, our experiment features magnetic gradient separation as an unambiguous signal for molecule formation (Fig. 5.3), as well as the ability to remove free

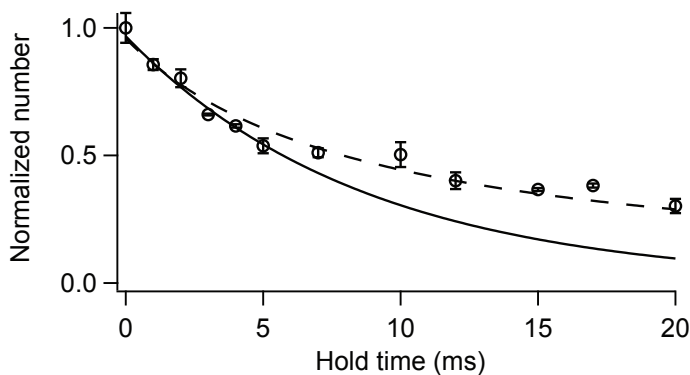


Figure 5.4: Lifetime of a pure sample of Li_2 molecules without free atoms present. The solid line is an exponential fit up to 5 ms hold time, giving decay time constants of 8.7(5) ms, while the dashed line is a fit to a full two-body decay function.

Li atoms to leave a pure gas of Li_2 , both of which were absent from the earlier experiments [Strecker *et al.*, 2003]. The atomic densities and temperatures from our two experiments are comparable, and thus cannot account for the discrepancy in observed lifetimes.

5.3 Collisions of ${}^6\text{Li}_2$ with Li and Na atoms

The lifetimes in Section 5.2 were limited by the rate of Li_2 molecules colliding with one another. The molecules are formed in the least-bound vibrational state of the spin-singlet potential, and any Li_2+Li_2 collision that results in vibrational decay of one of the collision partners will release enough kinetic energy to eject both from the trap. For the sake of completeness, we also measured how the presence of additional free atoms would affect the molecule decay lifetime. Applying the $|1\rangle$ and $|2\rangle$ -state blast beams (Fig. 5.3) at the end of the hold time instead of immediately after the molecule formation sweep allows us to measure molecule decay in the presence of free Li atoms. The small molecule formation efficiency of 10% means that the density of free Li atoms remaining after the sweep is much larger than the molecule density, and thus we expect that the resulting molecular decay lifetime will be significantly shortened because of the higher density of available collision partners.

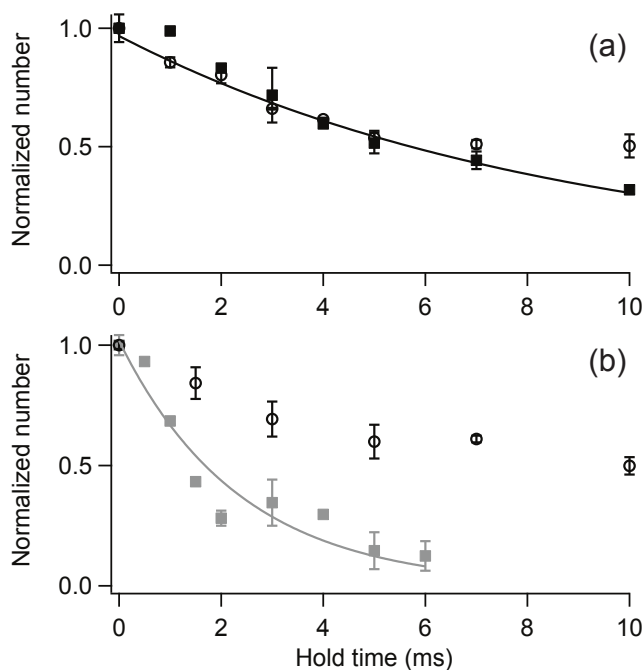


Figure 5.5: Lifetime of Li_2 in the presence of free atoms. (a) Decay with Li (solid squares) is almost identical to the decay of the pure Li_2 gas (open circles). (b) Decay with a similar initial density of Na (solid squares) is significantly faster than the decay of the pure Li_2 gas (open circles).

Surprisingly, we instead found that the addition of free Li atoms as collision partners had only a very small effect on the Li_2 lifetime (Fig. 5.5a), as compared to the decay of the molecular sample alone in Fig. 5.4. There should be no Pauli suppression of collisions for closed-channel Li_2 molecules with free Li atoms [Petrov *et al.*, 2004; Regal *et al.*, 2004]. We confirm this by checking that there is no enhancement of the decay after spin-flipping one component of Li from $|2\rangle$ to $|3\rangle$ ($|F, m_F\rangle = |3/2, -3/2\rangle$).

When Na instead of Li atoms are trapped with Li_2 , significant enhancement of the loss rate is observed (Fig. 5.5b), as expected, for initial Na densities similar to those of Li. The Na atoms can be included in the atomic mixture by interrupting the evaporatively cooling sequence near the very end, before all the remaining Na atoms are ejected (Section 5.2). Na and Li only interact weakly in a mixture, with $a_{\text{bg}} = 14a_0$ around the 543 G Li Feshbach resonance Schuster *et al.* [2012]. Thus, the presence of Na has a negligible effect on Li_2 molecule formation. The mixture is also produced with comparable temperature and initial

Li_2 density as in decay measurements done without Na.

5.4 The Quantum Langevin Model for Collisional Loss

In order to better understand the anomalous collision measurements from Section 5.3, we must consider a more concrete model for how collisions involving molecules happen at ultracold temperatures. There exists a simple, universal description for two-body inelastic collisions and chemical reactions of an ultracold molecule with another molecule or atom [Gao, 2010; Julienne *et al.*, 2011; Quéméner *et al.*, 2011]. This quantum Langevin model assumes a large number of available exit channels in the short-range part of the interaction potential, leading to a unit probability of loss there, and leaving the decay rate dependent on only the C_6 coefficient for the long-range van der Waals interaction between collision partners (Fig. 5.6). In particular, for standard two-body decay parametrized by a coefficient β

$$\frac{dn_j}{dt} = -\beta_{j+k} n_j n_k \quad (5.1)$$

where j is an ultracold molecule like Li_2 , k is its collision partner (another Li_2 molecule, a free atom of Li, or a free atom of Na), and n is the density. The coefficients β for different partial waves are

$$\begin{aligned} \beta_{s\text{-wave}} &= g \frac{4\pi\hbar}{\mu} R_{\text{vdW}} \\ \beta_{p\text{-wave}} &= g \frac{24\pi k_B T}{\hbar} R_{\text{vdW}}^3 \end{aligned} \quad (5.2)$$

with the van der Waals length $R_{\text{vdW}} = \frac{2\pi}{\Gamma(1/4)^2} \left(\frac{2\mu C_6}{\hbar^2} \right)^{1/4}$, and where the prefactor $g = 1$ or 2 depending on whether the collision partners are distinguishable or indistinguishable.

The quantum Langevin model has been validated in various experimental settings [Quéméner and Julienne, 2012], involving heavier alkali molecules like Rb_2 [Wynar *et al.*, 2000], Cs_2 [Staanum *et al.*, 2006; Zahzam *et al.*, 2006], KRb [Ospelkaus *et al.*, 2010], RbCs [Hudson *et al.*, 2008], and LiCs [Deiglmayr *et al.*, 2011]. We can apply it to the case of collisions

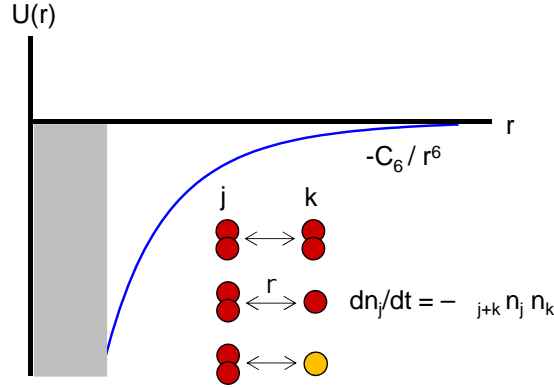


Figure 5.6: Quantum Langevin model for collisions between an ultracold molecule j and another molecular or atomic collision partner k . Assuming there was such a large number of available decay states in the short-range part of the interaction potential such that the probability of loss there is unity, then two-body loss coefficients β_{j+k} reduce to being simple, universal functions of the C_6 coefficient of the long-range part of the potential

Collision Partners	C_6 (a.u.)	$\beta_{s\text{-wave}}^{\text{th}}$ (cm^3/s)	$\beta_{s\text{-wave}}^{\text{exp}}$ (cm^3/s)
Li_2+Li_2	5580	7.1×10^{-10}	$6(2) \times 10^{-10}$
Li_2+Li	2970	3.0×10^{-10}	$< 5 \times 10^{-11}$
Li_2+Na	4253	2.5×10^{-10}	$4(1) \times 10^{-10}$

Table 5.1: Two-body decay coefficients for Li_2 with different collision partners Li_2 , Li , and Na . The theoretical value $\beta_{s\text{-wave}}^{\text{exp}}$ is taken from the quantum Langevin theory while the experimental values come from the measurements described in this chapter

involving Li_2 by approximating C_6 for each pair of collision partners as being the sum of the corresponding C_6 coefficients for all combinations of atom pairs involved Deiglmayr *et al.* [2011]. Thus, $C_6^{\text{Li}_2+\text{Li}_2} = 4 C_6^{\text{Li}+\text{Li}}$, $C_6^{\text{Li}_2+\text{Li}} = 2 C_6^{\text{Li}+\text{Li}}$ and $C_6^{\text{Li}_2+\text{Na}} = 2 C_6^{\text{Li}+\text{Na}}$. Using atomic C_6 coefficients taken from calculations [Derevianko *et al.*, 2001; Mitroy and Bromley, 2003], we can summarize the results of the quantum Langevin calculations in Table 5.1 and compare against the experimental results from Sections 5.2 and 5.3. The Li_2+Li collision shows a striking deviation from the predictions of the quantum Langevin model, and the reason for this will be explained in Section 5.5.

In our experiment, two-body decay of Li_2 molecules is described by adding the contri-

butions from Eq. 5.1

$$\frac{\dot{n}_{\text{Li}_2}}{n_{\text{Li}_2}} = -\beta_{\text{Li}_2+\text{Li}_2}n_{\text{Li}_2} - \beta_{\text{Li}_2+\text{Li}}n_{\text{Li}} - \beta_{\text{Li}_2+\text{Na}}n_{\text{Na}} \quad (5.3)$$

Experimentally, we measure the decay of total molecule number N_{Li_2} rather than n_{Li_2} , so Eq. 5.1 can be written, assuming separate Gaussian density distributions for Li_2 , Li and Na

$$2^{3/2}\frac{\dot{N}_{\text{Li}_2}}{N_{\text{Li}_2}} = -\beta_{\text{Li}_2+\text{Li}_2}\tilde{n}_{\text{Li}_2} - \beta_{\text{Li}_2+\text{Li}}\tilde{n}_{\text{Li}} - \beta_{\text{Li}_2+\text{Na}}\tilde{n}_{\text{Na}} \quad (5.4)$$

with \tilde{n} denoting peak in-trap densities. The various two-body decay coefficients β can thus be extracted from the measurements in Fig. 5.4 and 5.5 by fitting exponential decay rates at short hold times and normalizing by the initial peak densities. The factor $2^{3/2}$ accounts for the variation of density across the trap. The effect of deviations of density profiles from Gaussian is much smaller than the quoted uncertainties for β .

Full expressions for trapped ideal Bose(Fermi) gases in the local density approximation are used to calculate peak densities $\tilde{n}_{\text{Na(Li)}} = \pm(\frac{mk_B T}{2\pi\hbar^2})^{3/2}\text{Li}_{3/2}(\pm z)$, where m is the mass of the Na(Li) atom, T is the temperature of the gas, and $\text{Li}_n(z)$ is the n -th order Polylogarithm [Ketterle and Zwierlein, 2008]. We determine T before the molecule formation sweep by fitting Li time-of-flight expanded 2D column density profiles with the fugacity $z = e^{\beta\mu}$ as a free parameter, giving $T/T_F = 0.2$ or $T = 400$ nK. After the molecule formation sweep, \tilde{n}_{Li} is lower by a factor of two compared to before the sweep, despite a molecule conversion efficiency of only 10%, because many more atoms are associated into molecules that are lost via collisions with other molecules in the time it takes to complete the sweep.

For the Li_2 density, the simplest assumption is that the density distribution is proportional to the Li density profile before the sweep, meaning that \tilde{n}_{Li_2} can be estimated from the ratio of total numbers

$$\tilde{n}_{\text{Li}_2} = \tilde{n}_{\text{Li}}N_{\text{Li}_2}/N_{\text{Li}} \quad (5.5)$$

and likewise for the reduced \tilde{n}_{Li} after the sweep. This is valid if we neglect the complicated

density-dependence of molecule formation efficiency [Köhler *et al.*, 2006] and assume that Li atoms are selected at random from the Fermi sea to form molecules that do not have time to reach thermal equilibrium. We improve on this by accounting for the effect of equilibration. Molecules form with the same average center-of-mass kinetic energy as the free atoms, but twice the potential energy (due to their larger polarizability). Assuming that equilibration distributes this excess energy among all the degrees of freedom (according to the Virial theorem applied to harmonic traps), the cloud width is rescaled by $\sqrt{3/4}$. In our experiment, Li_2 does not equilibrate along the weak axial trapping direction, so the radial cloud diameter is instead rescaled by $\sqrt{7/10}$. This implies that Eq. (5.5) underestimates the peak Li_2 density by about 30%, which is within the quoted uncertainty of our results, but we nevertheless include the correction in the analysis. This correction does not apply to \tilde{n}_{Li} after the sweep ¹.

5.5 Quantum Depletion and Deviation from Universality

The observed deviation from the predictions of the quantum Langevin model in Li_2+Li collisions can be explained using a full close-coupling quantum calculation that predicts a two-body coefficient of $5 \times 10^{-11} \text{ cm}^3/\text{s}$ for Li_2 in the least bound triplet state [Quéméner *et al.*, 2007]. A similarly low value can be inferred for the least bound singlet state in our experiment from the same mechanism [Quéméner, 2012]. This effect is called quantum depletion, and can be explained in terms of the least-bound vibrational state of a molecule having by far the worst spatial overlap with lower-lying states due to its large spatial extent (Fig. 5.7). In the Li_2 molecule, the large vibrational level spacings results in a suppression of decay in collisions with free Li atoms by quantum depletion. This suppression is absent for collisions involving heavier alkali molecules, which have smaller vibrational level spacing. It also is not present in collisions of Li_2+Na and Li_2+Li_2 , because these both a higher density of available decay states in the exit channel [Quéméner and Julienne, 2012; Quémeéner *et al.*,

¹Random loss from a Fermi-Dirac distribution leaves the root-mean-square size of equilibrated cloud unchanged

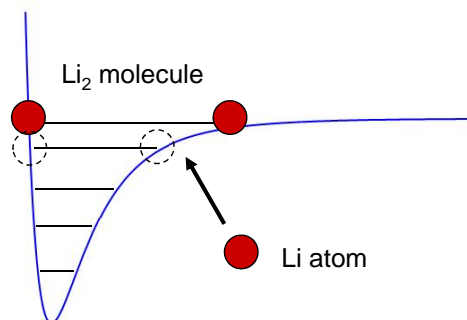


Figure 5.7: Quantum depletion of vibrational decay in molecules. The least-bound vibrational state of a molecule, due to its large spatial extent, has the worst spatial overlap with lower-lying states. For most molecules, however, the density of these lower-lying states is so large that the molecules still undergo rapidly decay when colliding with free atoms. In the case of Li_2 , its exceptionally large vibrational spacing means there is a very sparse set of decay states, and vibrational decay from the least-bound state in a collision with a free Li atom is in fact suppressed by quantum depletion

2007; Quéméner, 2012].

In summary, Li_2+Li collisions represent the first example of collisions involving ultracold molecules determined by physics beyond the simple, long-range van der Waals interactions. The significance of this is that universal collisions described only by the quantum Langevin model do not depend on details of the short-range part of the interaction potential, because loss is assumed to be unity there. From a chemistry standpoint, it is thus interesting to search for examples of collisions like Li_2+Li that deviate from universality, because a number of phenomena involving ultracold molecules, such as scattering resonances or reactivity determined by matrix elements between quantum states, that do depend on the short-range part of the interaction potential.

Chapter 6

Future Directions

To bring this dissertation to its conclusion, I will highlight in this final chapter some of the future directions that the experimental work in this dissertation has laid the foundations for. Specifically, I will introduce in Section 6.1 the possibility of transferring the NaLi molecule to what is anticipated to be the most long-lived spin-triplet ground state among the heteronuclear alkali atoms. Following this, in Section 6.2 I will briefly describe the technique of stimulated Raman adiabatic passage (STIRAP) for transferring weakly-bound NaLi molecules formed using a Feshbach resonance to their spin-triplet ground state, and then consider in greater detail the first step of doing photoassociation spectroscopy to map out the completely unknown electronically excited spin-triplet potentials, in order to find a suitable intermediate state for STIRAP. The chapter will end with Section 6.3 by considering two scientific opportunities that NaLi molecules in their triplet ground states can unlock: magnetic-field tunability of collisions, and the realization of arbitrary spin Hamiltonians mediated by spin-rotation coupling in molecules.

6.1 A Long-Lived $^{23}\text{Na}^6\text{Li}$ Spin-Triplet Ground State

For diatomic molecules consisting of alkali atoms, the ground-state of the spin-triplet potential is a metastable one, and can decay to lower lying spin-singlet states (Fig. 6.1). Whereas for other molecules this happens too rapidly for the triplet ground-state to be experimentally

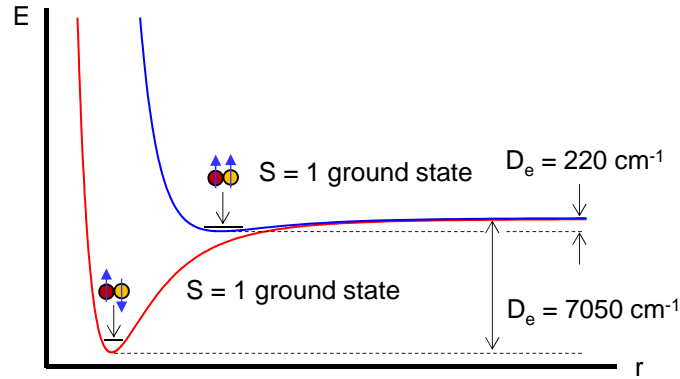


Figure 6.1: Spin-triplet and singlet ground states of NaLi. The $S = 1$ spin-triplet ground state can decay to lower lying spin-singlet $S = 0$ states, since the singlet potential is so much deeper. The dissociation energies D_e of the potentials are 7050 cm^{-1} for the singlet and 220 cm^{-1} for the triplet [Mabrouk and Berriche, 2008]. The triplet ground state has an unpaired total electron spin, which can have projections 0 or ± 1 , while the singlet ground state has no unpaired electron spins.

useful [Ni, 2009], in NaLi the triplet ground-state is expected to have a considerably longer lifetime. This triplet ground-state is appealing because of possibility of having a magnetic moment coming from the unpaired electron spins, along with a small but significant electric dipole moment of ~ 0.2 Debye [Aymar and Dulieu, 2005; Mabrouk and Berriche, 2008].

Decay of the spin-triplet ground-state to lower-lying spin-singlet states requires flipping of the electron spin. This can happen via dipolar relaxation or second-order spin-orbit coupling. Both of these spin-flip terms are common to the collision Hamiltonians of both molecules and atoms. Dipolar relaxation arises from dipole-dipole coupling between the magnetic dipole moments in each collision partner, and is a negligible contribution to loss in the smaller alkali atoms, with $\beta_{\text{dip}} \sim 10^{-14} \text{ cm}^3/\text{s}$ [Gerton *et al.*, 1999]. Since the magnetic dipole of a triplet ground-state molecule is the same order of magnitude as that of an alkali atom ($S = 1$ vs. $S = 1/2$), dipolar relaxation in molecules will also be similarly slow [Krems *et al.*, 2009]. Second-order spin-orbit coupling produces spin-flips indirectly through intermediate excited states with electronic orbital angular momentum. In atoms it is an effect that grows with increasing nuclear charge Z [Bernath, 2005], and is weaker than dipolar relaxation in the small alkali atoms [Mies *et al.*, 1996]. Since in NaLi the closest

excited state with electronic orbital angular momentum is $\text{Na}(3s)+\text{Li}(2p)$, we expect that second-order spin-orbit coupling will, as in the case of the bare Li atom, have a negligibly small effect.

We can estimate the lower-bound for the triplet ground-state lifetime by using the quantum Langevin model from Section 5.4. This assumes the worst-case scenario, that dipolar relaxation and second-order spin-orbit coupling are still large enough effects to result in unit probability of loss at short-range. For heteronuclear molecules, there are two contributions to C_6 . The first is the same induced dipole-dipole interactions as in atoms, via second-order coupling to electronic excited states. The second is a $d^4/(6B_\nu)$ term that comes from the dipole moment of the molecule, where d is the dipole moment and B_ν is the rotational constant [Julienne *et al.*, 2011]. Whereas for bigger molecules this second term becomes the dominant contribution to C_6 , for NaLi, with its moderate d and large B_0 , its C_6 of 3900 a.u. comes mainly from second-order coupling to electronic excited states, and is the smallest among the heteronuclear alkali molecules [Julienne *et al.*, 2011; Quémener *et al.*, 2011]. Since NaLi is a composite fermion, we can use the quantum Langevin model from Section 5.4 to estimate the temperature-dependent p-wave universal two-body loss rate. At 1 μK , this gives an exceptionally small $\beta = 2 \times 10^{-13} \text{ cm}^3/\text{s}$, corresponding to a lifetime of $> 1 \text{ s}$ at densities of $\sim 10^{12} \text{ cm}^{-3}$.

6.2 Photoassociation Spectroscopy of $^{23}\text{Na}^6\text{Li}$

The plan for transferring NaLi molecules from the least-bound triplet vibrational state with two units of rotational angular momentum to the rotational and vibrational ground-state of the triplet potential is to use two-photon stimulated Raman adiabatic passage (STIRAP) [Ni, 2009]. As shown in Fig. 6.2, STIRAP requires detailed knowledge of both the electronic ground and excited states involved. The Rabi frequencies Ω_1 and Ω_2 of each leg of the STIRAP process depend on the corresponding dipole matrix elements [Steck, 2010], which, as described in Section 2.7, scale with the vibrational Franck-Condon over-

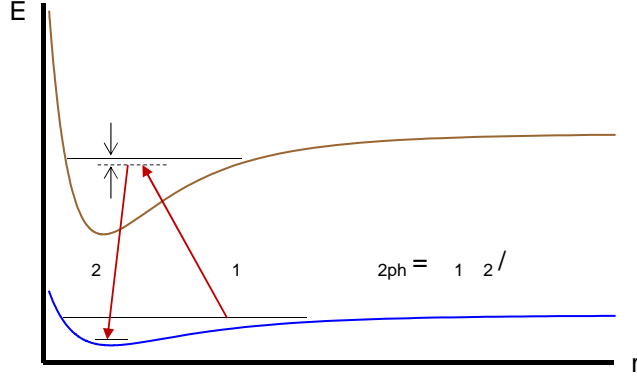


Figure 6.2: Stimulated Raman adiabatic passage is a two-photon process for molecular state transfer. Two laser beams with Rabi frequencies Ω_1 and Ω_2 connect the initial and final states respectively to an intermediate state. Both lasers are detuned from the intermediate state by $\Delta \gg \Omega_1, \Omega_2$, and the resulting two-photon Rabi frequency is $\Omega_{2ph} = \Omega_1 \Omega_2 / \Delta$

laps between the pairs of states involved. The two-photon Rabi frequency thus becomes $\Omega_{2ph} \sim (\langle \nu_i | \nu_{int} \rangle) (\langle \nu_f | \nu_{int} \rangle) \sqrt{I_1 I_2}$, where ν_i , ν_f and ν_{int} are the initial, final, and intermediate vibrational states, while I_1 and I_2 are the intensities of each of the two STIRAP beams.

Before performing STIRAP, we must identify a suitable intermediate state with sufficient Franck-Condon overlaps with both initial and final states $\langle \nu_i | \nu_{int} \rangle$ and $\langle \nu_f | \nu_{int} \rangle$ such that for experimentally available laser intensities I_1 and I_2 , Ω_{2ph} is sufficiently large, in the \sim kHz range, to accomplish the molecular state transfer during the ~ 1 ms lifetime of NaLi molecules formed around a Feshbach resonance (Section 4.4). Note that the choice of Δ depends on having sufficiently small off-resonant population of the excited state $(\Omega_1 / \Delta)^2$ such that the decay rate $\Gamma (\Omega_1 / \Delta)^2$ does not limit the lifetime of molecules in the initial state. To a good approximation, Γ for the molecular excited state is just the spontaneous emission rate of the excited bare atom. For comparison, STIRAP to the triplet ground-state in $^{40}\text{K}^{87}\text{Rb}$ was accomplished with moderate laser powers in $25 \mu\text{s}$ [Ni, 2009]. The main caveat is that vibrational levels in NaLi are more sparse, as discussed in Section 2.1 and 2.3, which will make it more challenging to find a suitable intermediate state with good overlap with both initial and final states. Also, note that since the initial molecular state formed using a Feshbach resonance has two units of rotational angular momentum,

the intermediate state must necessarily have one unit of rotational angular momentum to connect to the final, ro-vibrational ground-state in the triplet potential in a way that satisfies electric-dipole selection rules (Section 2.7).

There is currently no existing experimental data on the electronically excited triplet states in NaLi that might be candidates for an intermediate state in STIRAP. Prior to the experimental work described in Chapter 4, the only available NaLi molecules have been absolute ground-state spin singlet ones, and as mentioned in Section 2.8, efforts using these to explore the spin-triplet potential via spin-orbit mixing of singlet and triplet electronically excited states have thus far been unsuccessful [Steinke *et al.*, 2012]. As a result, in order to identify suitable candidates for an intermediate state in STIRAP, we must perform spectroscopy of the NaLi triplet potentials for the first time.

Based on Section 2.1, we expect the least-bound triplet excited state to be within ~ 3 GHz of dissociation, with another ~ 20 GHz to the next bound-state. An initial approach for finding the first of these states might be photoassociation spectroscopy [Jones *et al.*, 2006; Ulmanis *et al.*, 2012] to associate free atom pairs directly into a molecule in an electronically excited triplet state, thus bypassing the short ~ 1 ms lifetime of triplet molecules formed using a Feshbach resonance. Once the first excited state is found, the LeRoy-Bernstein formula from Section 2.1 constrains the locations of the more deeply-bound near dissociation states. The entire set of bound-states in a particular triplet potential can thus be iteratively mapped out, with the observation of each state providing updated parameters to the theoretical potential, which then leads to a more precise prediction for the location of the next state. The ground-state triplet potential can likewise be mapped out by two-photon spectroscopy. With the first photoassociation laser for the upward leg Ω_1 (Fig. 6.2) fixed on resonance ($\Delta=0$) with a triplet excited state, the frequency of the second laser for the downward leg Ω_2 can be varied. When this second laser is resonant with a vibrational level in the triplet ground-state potential, Autler-Townes splitting of the intermediate state [Steck, 2010] will result in a reduction of the photoassociation signal from the first laser [Ni, 2009].

The search procedure for detecting the first photoassociation line might involve holding a Li+Na mixture in a trap, and sweeping the photoassociation laser in frequency at some constant rate $d\nu/dt$ for a time t that is limited by the trap lifetime. In our cloverleaf magnetic trap, where the trap lifetime is limited only by collisions with residual background gas atoms, a sweep lasting as long as ~ 10 s is feasible. The frequency range over which one can sweep in a single search is thus determined by $d\nu/dt$, which in turn is fixed by the duration one must spend within the natural linewidth Γ_0 of the transition to produce a measurable loss of the atomic sample to photoassociation. For simplicity one can just take $\Gamma_0 = 6$ MHz, which is the natural linewidth of the bare ${}^6\text{Li}$ atom. This means that if we want to produce 50% loss of atoms in a single frequency sweep, then $\frac{\Gamma_{\text{PA}}\Gamma_0}{d\nu/dt} = \frac{1}{2}$, where Γ_{PA} is the photoassociation rate, in units of 1/s. Note that we are assuming with this estimate that the transition Γ_0 is not power-broadened, which is the same as staying below the saturation threshold. This is a good estimate because going beyond the saturation threshold requires using more photoassociation laser power with diminishing returns.

Consequently, we must understand Γ_{PA} for the Li+Na system in order to devise the appropriate frequency-sweep search procedure. The theoretical maximum for this rate is [Jones *et al.*, 2006]

$$\Gamma_{\text{PA}}^{\text{max}} \approx \frac{nv_{\text{rel}}\pi}{k^2} \quad (6.1)$$

where n is the atomic density, k is the scattering wave vector in relative coordinates, and v_{rel} is the relative speed. For photoassociation in a mixture of two different atoms, n can be taken to be the larger of the two densities. $\Gamma_{\text{PA}}^{\text{max}}$ is sometimes called the unitarity limit, because it assumes that photoassociation is only limited by the collision rate of the atoms, and with unlimited laser power, every atom pair that collides is converted to an electronically excited molecule. For Li+Na, if we take $k \sim \sqrt{2m_{\text{Li}}k_B T}/\hbar$, $v_{\text{rel}} = \hbar k/m_{\text{Li}}$, and $n = 10^{12} \text{ cm}^{-3}$, then at $T = 1 \text{ } \mu\text{K}$, $\Gamma_{\text{PA}}^{\text{max}} \sim 7000 \text{ s}^{-1}$ or $\Gamma_{\text{PA}}^{\text{max}}/n = K_{\text{PA}}^{\text{max}} \sim 7 \times 10^{-9} \text{ cm}^3/\text{s}$. This $\Gamma_{\text{PA}}^{\text{max}}$ corresponds to a very large $d\nu/dt = 80 \text{ GHz/s}$. The terms k and v_{rel} were approximated as ones corresponding to Li alone, because Li is the lighter atom and therefore

the much faster moving one on average.

In general, Γ_{PA} depends on the density n , the laser intensity $I_1 \propto \Omega_1^2$, and the dipole matrix element between the initial scattering state and the electronically excited bound-state. The last of these depends on a_{bg} , which from Section 3.2 determines the amplitude of the scattering wave function within the range of the interaction potential, and in turn affects the Franck-Condon vibrational wave-function overlap part of the dipole matrix element. The dipole matrix element for heteronuclear atom pairs is also significantly smaller than for homonuclear atom pairs, because from the discussion in Section 2.1, the near-dissociation electronically excited states of homonuclear atom pairs have much larger spatial extent due to the $1/r^3$ form of the potential there, as compared to heteronuclear atom pairs with their $1/r^6$ potential. Finally, the dipole matrix element is expected to increase for molecules like NaLi with smaller reduced mass μ [Pillet *et al.*, 1997; Azizi *et al.*, 2004]. This is because if we sum the modulus squares of the Franck-Condon factors, $\sum_j \langle \nu_i | \nu_j \rangle \langle \nu_j | \nu_i \rangle = 1$. For molecules with smaller μ and hence larger spacings of ro-vibrational states, this means that the fixed total weight of the Franck-Condon factors will be distributed over a smaller number of states.

The Li+Na system has a modest, negative background scattering length $a_{\text{bg}} = -76a_0$ [Schuster *et al.*, 2012]. In many ways it is comparable to the Li+Rb system, which also has a modest negative background scattering length for various isotope combinations [Marzok *et al.*, 2009; Deh *et al.*, 2010], and moreover has a similarly small reduced mass μ dominated by the contribution from Li, meaning that the LiRb molecule also has large ro-vibrational level spacings. Thus, without more detailed knowledge of the dipole matrix elements in Li+Na, we can use photoassociation experiments with Li+Rb as a benchmark. The main qualitative difference between the two systems is that the first electronically excited state of LiRb corresponds to Li(2s)+Rb(5p), which has stronger spin-orbit coupling due to the larger nuclear charge Z of Rb.

Recent work on photoassociation of ${}^7\text{Li}+{}^{85}\text{Rb}$ at ~ 1 mK found a photoassociation rate Γ_{PA} comparable to the theoretical maximum in Eq. 6.1 for a state with binding energy

of 15 GHz, with atomic densities of $5 \times 10^9 \text{ cm}^{-3}$ for both components and a saturation laser intensity of 60 W/cm^2 [Dutta *et al.*, 2014]. Moreover, in the low-intensity regime, they found that the slope of K_{PA} with intensity I_1 was $2 \times 10^{-12} (\text{cm}^3/\text{s})/(\text{W/cm}^2)$. For a given atom pair, this slope is independent of temperature [Jones *et al.*, 2006]. At different temperatures, with the same initial, low-intensity slope, the saturated, unitarity-limited $K_{\text{PA}}^{\text{max}}$ scales as $T^{-1/2}$, and the saturation intensity correspondingly has the same $T^{-1/2}$ scaling.

In our case of $^6\text{Li}+^{23}\text{Na}$, the atomic densities are $\sim 10^{12} \text{ cm}^{-3}$. If we make the one vital assumption of comparable dipole matrix elements between Li+Na and Li+Rb, then using the previous slope of $2 \times 10^{-12} (\text{cm}^3/\text{s})/(\text{W/cm}^2)$ as obtained by [Dutta *et al.*, 2014] for Li+Rb photoassociation, we find that the saturation intensity at $1 \mu\text{K}$ as opposed to 1 mK is 2000 W/cm^2 . This corresponds to focusing a 1-W beam down to a radius of $100 \mu\text{m}$ to obtain the maximum 80 GHz/s unitarity-limited sweep rate. Suppose we decided to be far more conservative, and sweep by 800 MHz/s . This would assume that the actual, temperature-independent slope of K_{PA} with I_1 is actually a factor of 100 smaller for Li+Na as compared to for Li+Rb, and consequently the dipole matrix element is also 100 times smaller. As summarized in [Dutta *et al.*, 2014], for most other heteronuclear alkali atom pairs studied thus far, the maximum measured K_{PA} has been well within two-orders of magnitude of the unitarity limit $K_{\text{PA}}^{\text{max}}$.

Photoassociation near the dissociation threshold is a competition between the rate of molecule formation and the rate of atom loss from off-resonant excitations. The latter of these has a rate $\Gamma_{\text{atom}} = \Gamma_0 (\Omega_0/\Delta_0)^2$, where Ω_0 is the Rabi frequency derived from the free atom dipole matrix element, and Δ_0 is the detuning from the free atom transition. The relative rate $\Gamma_{\text{PA}}/\Gamma_{\text{atom}}$ increases for photoassociation targeting the more deeply bound states. One semi-classical model for this considers the fact that as the bond length R_e shrinks for the more deeply bound levels, the photoassociation rate decreases as R_e^2 if one imagines that, in a gas with uniform density, each atom looks for a binding partner on a sphere with surface area $4\pi R_e^2$ [Ulmanis *et al.*, 2012]. For a $1/r^6$ van der Waals potential,

this means $\Gamma_{\text{PA}} \propto R_e^2 \propto \Delta_0^{-1/3}$, meaning that it decreases more slowly with increasing Δ_0 as compared to Γ_{atom} . Despite its simplicity, this model is fairly robust, since we could have assumed a much stronger power-law scaling of Γ_{PA} with R_e and still obtained the same conclusion. The two drawbacks of going to more deeply bound states are, of course, a necessarily smaller frequency sweep rate $d\nu/dt$ for the same density and laser intensity due to a smaller dipole matrix element for the transition, as well as significantly larger spacing between adjacent levels.

6.3 New Possibilities with Triplet Ground-State Molecules

The realization of a spin-triplet ground state molecule of NaLi will open up at least three distinct scientific opportunities. The first of these is the exploration of whether collisions involving ultracold molecules can be tuned in the same manner as Feshbach resonances for atoms in Chapter 3 [Tscherbul *et al.*, 2009]. Due to the high density of available decay states in collisions involving molecules, it is possible that quantum scattering resonances will overlap, leading to an averaged-over, featureless overall scattering dependence on magnetic field [Mayle *et al.*, 2013]. However, as we demonstrated in Chapter 5, it is precisely in the smallest molecules, with the most sparse density of states, that collisional behaviour can deviate from the assumption of there being an essentially infinite density of available decay states. For example, collisions of NH and ND molecules with ^3He may already be influenced by the presence of scattering resonances [Campbell *et al.*, 2009].

A second direction comes from the proposal of [Micheli *et al.*, 2006], that molecules possessing both magnetic and electric dipole moments can be used to access a rich landscape of spin-Hamiltonians in optical lattices. The novel effective spin-spin couplings are due to spin-rotation coupling within each molecule, together with dipole-interaction-mediated coupling of the rotational states of molecules in adjacent lattice sites. The main experimental challenge of this proposal is that even for the most dipolar molecules, the dipolar interaction energy scale in a typical optical lattice $U_{\text{dd}} \sim 10$ kHz is still orders of magnitude smaller

than typical spin-rotation energy scales $\gamma \sim 10$ MHz, although according to [Micheli *et al.*, 2006], one can still realize designer spin models far away from the strong-coupling condition $U_{\text{dd}} = \gamma$, but the effective coupling coefficients, and consequently the resulting splittings, will be significantly smaller.

The third possibility for future experiments with the NaLi molecule in its spin-triplet ground state arises from its large rotational constant B . An initially spin-polarized gas of such molecules will become collisionally depolarized via dipole-dipole mixing with rotationally-excited states that have spin-rotation coupling, with a depolarization rate that scales as $1/B^2$ [Campbell *et al.*, 2009]. Spin-triplet ground state NaLi molecules can serve as a test-bed for collisional stability of $^3\Sigma$ molecules in general, illuminating the effects of rotational excitation, induced electric dipole moment, etc. on the depolarization rate. The stability of spin-aligned molecules against collisional depolarization has far-reaching implications for the ability to magnetically trap and cool a large variety of chemically interesting molecules down to quantum-degenerate temperatures.

However, one should keep in mind that, from the recent history of the field of matter at ultracold temperatures, and in the realm of science in general, the true extent of exciting possibilities for a new form of matter lies not with what researchers anticipate in advance, but what they discover after its realization. One can only hope the same is true in the field of ultracold molecules, and in particular with NaLi, the smallest of the heteronuclear alkali molecules.

Appendix A

Asymptotic Bound State Model

In this Appendix we include an example Mathematica worksheet for predicting Feshbach resonance locations in the ${}^6\text{Li}+{}^{23}\text{Na}$ system using the asymptotic bound-state method. The open-channel state consists of the atom pair in their lowest hyperfine states, $|m_s, m_I\rangle = |-\frac{1}{2}, 1\rangle$ and $|-\frac{1}{2}, \frac{3}{2}\rangle$ for Li and Na respectively. The total spin projection m_F of this atom pair is $3/2$, so there are a total of eight closed-channel bound states with $m_F = \frac{3}{2}$ that can produce Feshbach resonances in the open channel. Six of these are triplet states $|S m_S m_I^{Li} m_I^{Na}\rangle = |1 1 -1 \frac{3}{2}\rangle, |1 1 0 \frac{1}{2}\rangle, |1 1 1 -\frac{1}{2}\rangle, |1 0 1 \frac{1}{2}\rangle, |1 0 0 \frac{3}{2}\rangle,$ and $|1 -1 1 \frac{3}{2}\rangle$, while two of them are singlet states $|0 0 0 \frac{3}{2}\rangle$ and $|0 0 1 \frac{1}{2}\rangle$.

The Hamiltonian from Eq. 3.18 has matrix elements given in [Walraven, 2010]. The hyperfine constants and gyromagnetic ratios of the atoms are known [Arimondo *et al.*, 1977], while the triplet and singlet vibrational state binding energies E_1 and E_0 are left as free parameters. The worksheet uses a brute-force search method to find the combination of E_1 and E_0 that best matches experimentally observed Feshbach resonance locations. The result is $E_1 = 5710$ MHz and $E_0 = 4245$ MHz, which gives the locations of the three lowest-field Feshbach resonances as 744.5 G, 763.0 G and 794.7 G. These match up well with the predictions from full coupled-channel calculations in [Gacesa *et al.*, 2008] of 746.13 G, 759.69 G and 795.61 G, as well as the experimental values from [Stan *et al.*, 2004].

However, despite being in good agreement with the three lowest-field resonances, this

model for Feshbach resonances is actually incorrect [Schuster *et al.*, 2012], and in particular the locations of the next observed resonance is ~ 400 G away from its predicted location Christensen [2011]. The reason, as discussed in Section 4.1, is that the Feshbach resonances around 800 G are not produced by the traditional hyperfine coupling of the least-bound closed-channel state to the open-channel, but by weak dipole-dipole coupling of a $J = 2$ closed-channel rotating molecular state to the open-channel (J here refers to the rotational quantum number of the molecule, not the total orbital and spin angular momenta of the atoms). This pathological case is not present in other alkali atom pairs, and thus the worksheet below is still a good example how the simple asymptotic bound-state model can reproduce the results of a much more elaborate coupled-channel calculation.

This worksheet can be adapted for other atom pairs by changing the atomic constants, as well as the basis of bound states involved in producing Feshbach resonances in the open-channel. It has been successfully applied to the initial search for Feshbach resonances in $^{23}\text{Na}+^{40}\text{K}$, for which the discovery of one resonance location enabled one to constrain the binding energies, and thus predict where nearby resonances would be. The nearby resonances were quickly located based on these predictions, avoiding time consuming searches over wide magnetic field ranges, and further validating the values chosen for the binding energies E_1 and E_0 . The full description of resonances in $^{23}\text{Na}+^{40}\text{K}$ required including coupling between the bound states and the continuum scattering states in the closed channel, due to the large a_{bg} of the triplet potential [Wu *et al.*, 2012]. Including this additional coupling is possible in the asymptotic bound state model, but goes beyond the scope of the example worksheet included below.

```

(* Feshbach resonances Li |1> and Na |1> states *)
(* Based on asymptotic bound state model
   treated in Elements of Quantum Gases by JTM Walraven *)
uB := 1.4; (* Bohr magneton in units of MHz / G *)
InNa := 3 / 2; (* Nuclear spins of Na and Li *)
InLi := 1;
EhfNa := 1771.626 (* Hyperfine splittings *)
EhfLi := 228.2053
AhfNa := EhfNa / (InNa + 1 / 2) (* Corresponding hyperfine constants *)
AhfLi := EhfLi / (InLi + 1 / 2)
ye := 2.00232 * uB (* Gyromagnetic ratios *)
gammaNa := 0.00080461 * uB
gammaLi := 0.00044765 * uB
ETrip := -E1 (* Singlet and triplet binding energies *)
ESing := -E0
(* Matrix element of raising operator <j m2| J+ |j m1>/hbar *)
Raise[j_, m2_, m1_] := If[j == m1, 0, Sqrt[(j - m1) (j + m1 + 1)] KroneckerDelta[m2, m1 + 1]]
(* Matrix element of lowering operator <j m2| J- |j m1>/hbar *)
Lower[j_, m2_, m1_] := If[j == -m1, 0, Sqrt[(j + m1) (j - m1 + 1)] KroneckerDelta[m2, m1 - 1]]
(* Multivariable Kronecker delta function *)
KrDelta[{x1_, y1_}, {x2_, y2_}, {x3_, y3_}] :=
  KroneckerDelta[x1, y1] KroneckerDelta[x2, y2] KroneckerDelta[x3, y3]
(* Simplified Franck-Condon vibrational wave function
   overlap for two near dissociation halo dimer states *)
FranckCondon[E0_, E1_] := 2 (E0 E1) ^ (1 / 4) / (Sqrt[-E0] + Sqrt[-E1])
In[208]:= (* Term in Hamiltonian coupling singlet S=
   0 and triplet S=1 closed-channel bound states *)
(* Using total electron spin / projection,
   individual nuclear spin / projection basis | S mS mI1 mI2 > *)
HCrossCoup[{S2_, mS2_, mLi2_, mNa2_}, {S1_, mS1_, mLi1_, mNa1_}] :=
  (* (S1z - S2z) (ahf1/2 I1z - ahf2/2 I2z) *)
  (KrDelta[{S2, 1}, {mS2, 0}, {1, 1}] KrDelta[{S1, 0}, {mS1, 0}, {1, 1}] +
   KrDelta[{S2, 0}, {mS2, 0}, {1, 1}] KrDelta[{S1, 1}, {mS1, 0}, {1, 1}])
  (AhfNa / 2 mNa1 KrDelta[{mNa1, mNa2}, {mLi1, mLi2}, {1, 1}] -
   AhfLi / 2 mLi1 KrDelta[{mNa1, mNa2}, {mLi1, mLi2}, {1, 1}]) +
  (* (S1+ - S2+) (ahf1/2 I1- - ahf2/2 I2-) *)
  Sqrt[2] (-KrDelta[{S2, 1}, {mS2, 1}, {1, 1}] KrDelta[{S1, 0}, {mS1, 0}, {1, 1}] +
   KrDelta[{S2, 0}, {mS2, 0}, {1, 1}] KrDelta[{S1, 1}, {mS1, -1}, {1, 1}])
  (AhfNa / 4 Lower[InNa, mNa2, mNa1] KrDelta[{1, 1}, {mLi1, mLi2}, {1, 1}] -
   AhfLi / 4 Lower[InLi, mLi2, mLi1] KrDelta[{mNa1, mNa2}, {1, 1}, {1, 1}]) +
  (* (S1- - S2-) (ahf1/2 I1+ - ahf2/2 I2+) *)
  Sqrt[2] (KrDelta[{S2, 1}, {mS2, -1}, {1, 1}] KrDelta[{S1, 0}, {mS1, 0}, {1, 1}] -
   KrDelta[{S2, 0}, {mS2, 0}, {1, 1}] KrDelta[{S1, 1}, {mS1, 1}, {1, 1}])
  (AhfNa / 4 Raise[InNa, mNa2, mNa1] KrDelta[{1, 1}, {mLi1, mLi2}, {1, 1}] -
   AhfLi / 4 Raise[InLi, mLi2, mLi1] KrDelta[{mNa1, mNa2}, {1, 1}, {1, 1}])

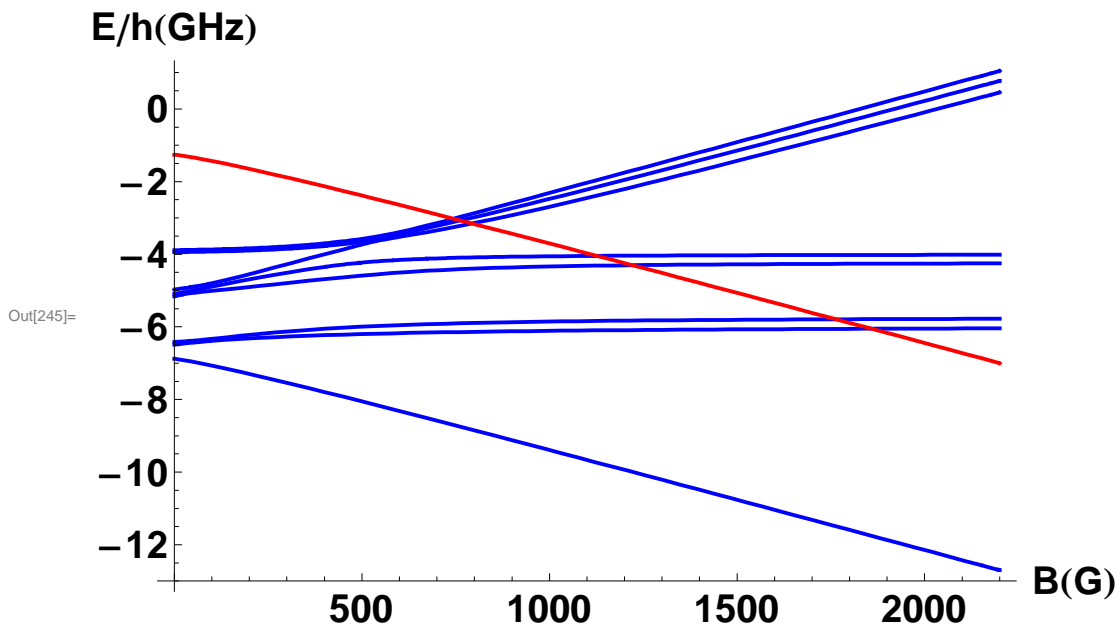
```



```

E1 = 5710; (* Set singlet binding energy based on results of search code below *)
E0 = 4245; (* Set triplet binding energy *)
(* Before starting executing search below,
play around with E1 and E0 to see what values are sensible *)
HamiltMatrix := Table[MatElem[MatrixConv[n1], MatrixConv[n2]], {n1, 1, 8}, {n2, 1, 8}];
EigenEnergy = Eigenvalues[HamiltMatrix];
(* Visualize where intersections between closed-channels and open-channel are *)
Plot[{EigenEnergy / 1000, energNa[Bf] / 1000 + energLi[Bf] / 1000},
{Bf, 0, 2200}, AxesLabel -> {"B(G)", "E/h(GHz)"},
PlotStyle -> {{Blue, Thick}, {Blue, Thick}, {Blue, Thick}, {Blue, Thick},
{Blue, Thick}, {Blue, Thick}, {Blue, Thick}, {Blue, Thick}}, {Red, Thick}},
BaseStyle -> {FontFamily -> "Arial", FontWeight -> "Bold", FontSize -> 20},
AxesOrigin -> {0, -13}]

```



```

(* Solve for where intersections occur *)
(* Predicted triplet resonances from M Gacesa: 746, 760, 796 G *)
FindRoot[EigenEnergy[[8]] == energNa[Bf] + energLi[Bf], {Bf, 750}]
FindRoot[EigenEnergy[[7]] == energNa[Bf] + energLi[Bf], {Bf, 760}]
FindRoot[EigenEnergy[[6]] == energNa[Bf] + energLi[Bf], {Bf, 800}]

```

Out[228]= {Bf -> 744.516}

FindRoot::lstol :

The line search decreased the step size to within tolerance specified by AccuracyGoal and PrecisionGoal but was unable to find a sufficient decrease in the merit function. You may need more than MachinePrecision digits of working precision to meet these tolerances. >>

Out[229]= {Bf -> 763.024}

Out[230]= {Bf -> 794.688}

```
In[231]:= (* Locations of two singlet resonances *)  
          (* Predicted resonances from M Gacesa: 1097, 1186 *)  
          FindRoot[EigenEnerg[[5]] == energNa[Bf] + energLi[Bf], {Bf, 1100}]  
          FindRoot[EigenEnerg[[4]] == energNa[Bf] + energLi[Bf], {Bf, 1200}]
```

```
Out[231]= {Bf -> 1127.83}
```

FindRoot::lstol :

The line search decreased the step size to within tolerance specified by AccuracyGoal and PrecisionGoal but was unable to find a sufficient decrease in the merit function. You may need more than MachinePrecision digits of working precision to meet these tolerances. >>

```
Out[232]= {Bf -> 1222.33}
```

```

(* Code for optimizing triplet and singlet binding energies E1, E0 *)
MinRef = 9999; (* Initial value for minimization variable *)
ETrip0 = 5700; (* Initial values for binding energies *)
ESing0 = 4200;
(* Optimization function *)
(* Elc,
E0c: search range center for triplet and singlet binding energies respectively *)
(* Step1, Step0: number of steps to search in each case *)
(* Range1, Range0: range of search in each case *)
(* These two define the optimization mesh *)
BindEnergOpt[Elc_, E0c_, Step1_, Step0_, Range1_, Range0_] :=
  For[x = -Step1, x < Step1, x++,
    For[y = -Step0, y < Step0, y++,
      E1 = Elc + Range1 / Step1 x;
      E0 = E0c + Range0 / Step0 y;
      HamiltMatrix := Table[MatElem[MatrixConv[n1], MatrixConv[n2]], {n1, 1, 8}, {n2, 1, 8}];
      EigenEnerg = Eigenvalues[HamiltMatrix];
      (* For each point in mesh (E1, E0),
      check how far away the three known resonances are *)
      MinVar = ((Bf /. FindRoot[EigenEnerg[[8]] == energNa[Bf] + energLi[Bf], {Bf, 750}]) - 746) ^
        2 +
        ((Bf /. FindRoot[EigenEnerg[[7]] == energNa[Bf] + energLi[Bf], {Bf, 760}]) - 760) ^ 2 +
        ((Bf /. FindRoot[EigenEnerg[[6]] == energNa[Bf] + energLi[Bf], {Bf, 800}]) - 796) ^ 2;
      (* Keep a record of which variable led
      to solutions that are closest to experimental resonances*)
      If[MinVar < MinRef, MinRef = MinVar; ETrip0 = Elc + Range1 / Step1 x;
        ESing0 = E0c + Range0 / Step0 y;
        , MinVar = 0]
    ]
  ]
(* Run optimization function and print results *)
BindEnergOpt[5700, 4200, 10, 10, 50, 50]
Print[{ETrip0, ESing0}];
Print[MinRef];

```

FindRoot::lstol :

The line search decreased the step size to within tolerance specified by AccuracyGoal and PrecisionGoal but was unable to find a sufficient decrease in the merit function. You may need more than MachinePrecision digits of working precision to meet these tolerances. >>

FindRoot::lstol :

The line search decreased the step size to within tolerance specified by AccuracyGoal and PrecisionGoal but was unable to find a sufficient decrease in the merit function. You may need more than MachinePrecision digits of working precision to meet these tolerances. >>

FindRoot::lstol :

The line search decreased the step size to within tolerance specified by AccuracyGoal and PrecisionGoal but was unable to find a sufficient decrease in the merit function. You may need more than MachinePrecision digits of working precision to meet these tolerances. >>

General::stop : Further output of FindRoot::lstol will be suppressed during this calculation. >>

{5710, 4245}

13.0314

Appendix B

Temperature and Density Measurements

In this Appendix, I will explain the procedure for measuring the temperature T and density n of trapped atoms in our experiment. We infer the temperature of trapped ${}^6\text{Li}$ atoms by measuring the two-dimensional, column-integrated density profile after time-of-flight, following [DeMarco, 2001]. The temperature of any ${}^{23}\text{Na}$ atoms trapped together with ${}^6\text{Li}$ is assumed to be the same, since the two atoms form a very favourable mixture with rapid thermalization and slow inelastic losses [Hadzibabic *et al.*, 2002]. Given T , the peak density as well as the density variation across trap can be calculated, assuming that the total atom number and trap frequencies are known.

The ${}^6\text{Li}$ column-integrated density profile in time-of-flight can be written as

$$\tilde{n}(x, y) \propto -\text{Li}_2 \left(-e^{\beta\mu} e^{-\frac{x^2}{\sigma_x^2} - \frac{y^2}{\sigma_y^2}} \right) \quad (\text{B.1})$$

where $\beta = (k_B T)^{-1}$, μ is the chemical potential, and $\text{Li}_2(x, y)$ is the second-order polylogarithm function [Ketterle and Zwierlein, 2008]. The expanded atomic density profile is assumed to have different widths σ_x and σ_y along the x and y-directions. In the high-temperature limit, $z = 1$ and Eq. B.1 reduces to an expression for the classical Maxwell-Boltzmann distribution. Thus, measuring the temperature of a degenerate Fermi gas corresponds to measuring the effect of the fugacity $e^{\beta\mu}$ on the density distribution.

Experimentally, we obtain time-of-flight absorption images as shown in Fig. B.1a. These

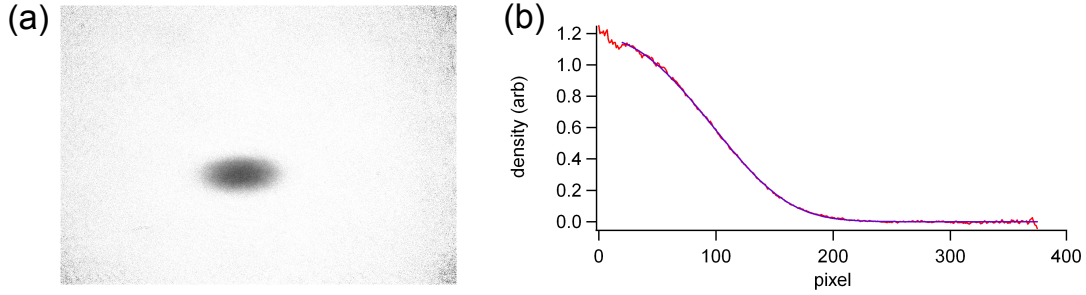


Figure B.1: Temperature measurement of a ${}^6\text{Li}$ cloud. (a) Absorption image of Li atoms after time-of-flight from an optical dipole trap. This image is converted to a two-dimensional column-integrated density profile, and then fit to a Gaussian to obtain the aspect ratio of the expanded cloud of atoms. This Gaussian fit is used to perform quadrant and elliptical averaging of the cloud. (b) The resulting column-integrated density as a function of scaled radius is plotted (red) and fit to the Polylogarithm function (blue) to obtain the fugacity

are converted to column-integrated density profiles \tilde{n} by taking the logarithm of each pixel value, and rejecting pixels whose values are too close to zero. The two-dimensional profiles are then fit to Gaussians to obtain the aspect ratio of the expanded cloud. This Gaussian fit is used to average the density profiles in two ways. First, based on the center of the Gaussian fit, each density distribution is averaged by reflecting along the x and y axes of symmetry to obtain four identical, averaged quadrants. Second, using the aspect ratio from the Gaussian fit, we can obtain elliptical contours along which $x^2/\sigma_x^2 + y^2/\sigma_y^2$ in Eq. B.1 is constant. The values of \tilde{n} are averaged along each of these ellipses and plotted as a function of the coordinate along the major axis of the ellipses. The resulting plots are fitted to the function $\tilde{n}(r) = A \text{Li}_2(e^{\beta\mu} e^{-r^2/\sigma_r^2})$ to obtain the fugacity $e^{\beta\mu}$, where r can be thought of as an effective radius for the ellipse, scaled to the major axis.

An example of such a fit is shown in Fig. B.1b, corresponding to $\beta\mu = 3.54$. From the low temperature expansion $\beta\mu = \left(\frac{T_F}{T}\right) \left(1 - \frac{\pi^2}{12} \left(\frac{T}{T_F}\right)^2 + \dots\right)$ [Lee, 2012], we can solve for $T/T_F = 0.27$, where T_F is the Fermi temperature corresponding to the density at the center of the trap. Note that at these low temperatures, the zeroth-order approximation $T/T_F \approx (\beta\mu)^{-1} = 0.28$ is already quite good. The temperature T can be calculated from the fugacity $e^{\beta\mu}$, the total atom number N , and the mean trap frequency $\bar{\omega} = (\omega_x\omega_y\omega_z)^{1/3}$

[Ketterle and Zwierlein, 2008]

$$N_f = - \left(\frac{k_B T}{\hbar \bar{\omega}} \right)^3 \text{Li}_3(-e^{\beta \mu}) \quad (\text{B.2})$$

with the subscript f indicating that the equation is valid for fermionic atoms. All the ingredients of the in-trap density distribution $n(\vec{r})$ in the local-density approximation are thus accounted for [Ketterle and Zwierlein, 2008]

$$n_f(\vec{r}) = - \frac{1}{\lambda_{\text{dB}}} \text{Li}_{3/2} \left(-e^{\beta \mu - V(\vec{r})} \right) \quad (\text{B.3})$$

where the de Broglie wavelength $\lambda_{\text{dB}} = \sqrt{\frac{2\pi\hbar^2}{mk_B T}}$ and $V(\vec{r})$ is the trap potential that is zero for $\vec{r} = 0$ and grows as one goes out from the center of the trap.

In the case of bosonic ^{23}Na , its temperature T can be assumed to be the same as that of the fermionic ^6Li . Then from the bosonic counterparts of Eq. B.2 $N_b = \left(\frac{k_B T}{\hbar \bar{\omega}} \right)^3 \text{Li}_3(e^{\beta \mu})$ we can infer the fugacity $e^{\beta \mu}$, and this gives the in-trap density distribution via the bosonic counterpart to Eq. B.3 $n_b(\vec{r}) = \frac{1}{\lambda_{\text{dB}}} \text{Li}_{3/2} \left(e^{\beta \mu - V(\vec{r})} \right)$ [Ketterle and Zwierlein, 2008]. Obviously, the trapping potential $V(\vec{r})$ and frequencies $(\omega_x, \omega_y, \omega_z)$ will be different for ^{23}Na vs. ^6Li because of their different dipole matrix elements.

Appendix C

The Breit-Rabi Formula

The Breit-Rabi formula is an exact expression for hyperfine state energies of $J = 1/2$ states of atoms, in particular the electronic ground states. It is especially useful for calibrating the magnetic field B in an experiment. Different fields B shift the hyperfine states such that transition frequencies between them change. Finding the resonant frequency that drives transitions between a particular pair of states thus becomes a measure of the field B experienced by the atom.

The Breit-Rabi formula is written as [Steck, 2010]

$$E_{|J=1/2, m_J; I, m_I\rangle} = -\frac{E_{\text{hfs}}}{2(2I+1)} + g_I \mu_B m B \pm \frac{E_{\text{hfs}}}{2} \left(1 + \frac{4mx}{2I+1} + x^2 \right)^{1/2} \quad (\text{C.1})$$

where $x = \mu_B(g_J - g_I)B/E_{\text{hfs}}$, E_{hfs} is the hyperfine splitting, $m = m_I \pm m_J$, g_J is the g-factor for total electronic angular momentum, g_I is the nuclear g-factor, and the \pm corresponds to whether a particular state belongs in the $F = I \pm 1/2$ manifold at zero field. The constants in Eq. C.1 can be obtained for each atom by consulting [Arimondo *et al.*, 1977]

In the next pages I include Mathematica worksheets for the Breit-Rabi formula for ${}^6\text{Li}$, followed by those for ${}^{23}\text{Na}$.

```

In[35]= (* Exact Breit-Rabi calculation for 6Li including nuclear terms *)
(* (+) or (-) root depends on whether state belongs to F=
  I+1/2 or F=I-1/2 manifold at zero field *)
state1[x_] := -ehf / 6 - gI uB x / 2 - ehf / 2 Sqrt[1 + 2 / 3 b[x] + b[x]^2];
(* mJ,mI = -1/2,1 *)
state2[x_] := -ehf / 6 + gI uB x / 2 - ehf / 2 Sqrt[1 - 2 / 3 b[x] + b[x]^2];
(* mJ,mI = -1/2,0 *)
state3[x_] := -ehf / 6 + 3 gI uB x / 2 + ehf / 2 (1 - b[x]); (* mJ,mI = -1/2,-1 *)
state4[x_] := -ehf / 6 + gI uB x / 2 + ehf / 2 Sqrt[1 - 2 / 3 b[x] + b[x]^2];
(* mJ,mI = 1/2,-1 *)
state5[x_] := -ehf / 6 - gI uB x / 2 + ehf / 2 Sqrt[1 + 2 / 3 b[x] + b[x]^2];
(* mJ,mI = 1/2,0 *)
state6[x_] := -ehf / 6 - 3 gI uB x / 2 + ehf / 2 (1 + b[x]); (* mJ,mI = 1/2,
1 *) (* mI order reversed - HFS more important than  $\gamma I$  *)
b[x_] := (ge + gI) * uB * x / ehf;
gI := 4.47654 * 10^-4 (* Nuclear g-factor for 6Li *)
ge := 2 * 1.001596521869; (* Electronic g-factor *)
uB := 1.39983 (* Bohr magneton in units of MHz/G *)
ehf := 228.20527 (* Hyperfine splitting for 6Li *)

(* Energy differences of various ground hyperfine states in MHz *)
diff12[x_] := state2[x] - state1[x];
diff13[x_] := state3[x] - state1[x];
diff23[x_] := state3[x] - state2[x];
diff16[x_] := state6[x] - state1[x];

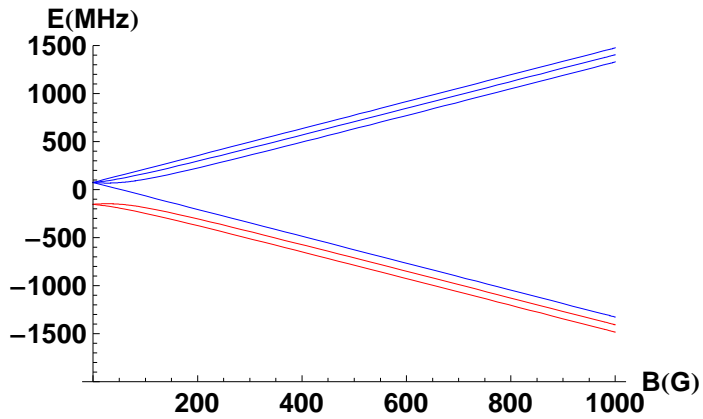
(* Calibration of magnetic field in B based
  on Li state 1 to 2 RF transition frequency in MHz *)
Solve[diff12[x] == 75.6575, x]
{{x -> 542.557}}

(* Check approximately what field Li spin flip is done at *)
Solve[diff16[x] == 262.6, x]
{{x -> -297648.}, {x -> 17.269}}

diff12[550.0]
75.6821

Plot[{state1[x], state2[x], state3[x], state4[x], state5[x], state6[x]},
  {x, 0, 1000}, PlotStyle -> {Red, Red, Blue, Blue, Blue, Blue},
  AxesLabel -> {"B(G)", "E(MHz)"}, PlotRange -> {-2000, 1500},
  BaseStyle -> {FontFamily -> "Arial", FontWeight -> "Bold", FontSize -> 14},
  AxesOrigin -> {0, -2000}]

```



```
(* Frequencies for imaging from ground states to 2P_{3/2} mJ = -3/2 *)
(* Excited state hyperfine splitting very small *)
state2p[x_] := -2 uB x (* Excited state shift in MHz *)
freq[x_] :=
  state2p[x] - state1[x] (* Difference in ground and excited state shifts *)
```

```
In[50]:= j1 := 3 / 2
s1 := 1 / 2
l1 := 1
(* Calculation of gJ for 2P_{3/2} state *)
(1 + (j1 (j1 + 1) + s1 (s1 + 1) - l1 (l1 + 1)) / (2 j1 (j1 + 1))) * 3 / 2
```

Out[53]= 2

```
freq[790]
-1022.5
```

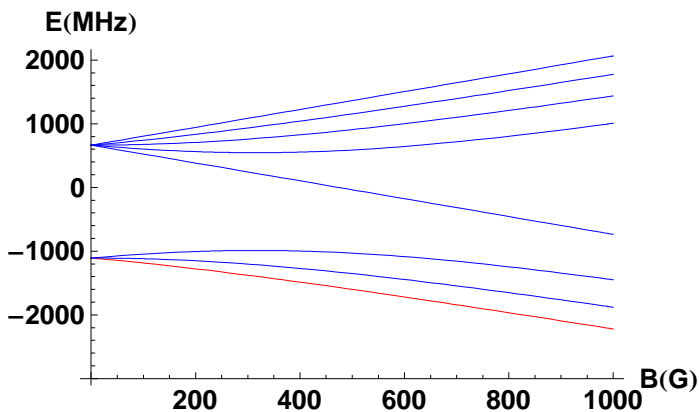
```
(* Mainly useful to obtain how much imaging
  frequency changes between different fields *)
(freq[907] - freq[795]) / 2
-78.5294
```

```

In[75]:= (* Exact Breit-Rabi calculation for 23Na including nuclear terms *)
(* Hyperfine state energies in MHz *)
state1[x_] := -ehf / 8 - gI uB x - ehf / 2 Sqrt[1 + b[x] + b[x]^2];
(* mJ,mI = -1/2,3/2 *)
state2[x_] := -ehf / 8 - ehf / 2 Sqrt[1 + b[x]^2]; (* mJ,mI = -1/2,1/2 *)
state3[x_] := -ehf / 8 + gI uB x - ehf / 2 Sqrt[1 - b[x] + b[x]^2];
(* mJ,mI = -1/2,-1/2 *)
state4[x_] := -ehf / 8 + 2 gI uB x + ehf / 2 (1 - b[x]); (* mJ,mI = -1/2,-3/2 *)
state5[x_] := -ehf / 8 + gI uB x + ehf / 2 Sqrt[1 - b[x] + b[x]^2];
(* mJ,mI = 1/2,-3/2 *)
state6[x_] := -ehf / 8 + ehf / 2 Sqrt[(1 + b[x]^2)]; (* mJ,mI = 1/2,-1/2 *)
state7[x_] := -ehf / 8 - gI uB x + ehf / 2 Sqrt[(1 + b[x] + b[x]^2)];
(* mJ,mI = 1/2,1/2 *)
state8[x_] := -ehf / 8 - 2 gI uB x + ehf / 2 (1 + b[x]); (* mJ,mI = 1/2,3/2 *)
b[x_] := (ge + gI) * uB * x / ehf;
gI = 8.04611 * 10^-4; (* Nuclear g-factor for Na *)
ge = 2 * 1.001596521869; (* Electron spin g-factor *)
uB = 1.39983; (* Bohr magneton in units of MHz/G *)
ehf = 1771.62615 (* Hyperfine splitting of Na in MHz *);

Plot[{state1[x], state2[x], state3[x], state4[x],
      state5[x], state6[x], state7[x], state8[x]}, {x, 0, 1000},
      PlotStyle -> {Red, Blue, Blue, Blue, Blue, Blue, Blue, Blue},
      AxesLabel -> {"B(G)", "E(MHz)"},
      BaseStyle -> {FontFamily -> "Arial", FontWeight -> "Bold", FontSize -> 14},
      AxesOrigin -> {0, -3000}]

```



```

In[85]:= (* Excited state energies easily in Paschen-
Back regime described by (7.138) of Steck Quantum and Atom Optics text *)
Ahfex = 18.534; (* Excited state hyperfine constants in MHz *)
Bhfex = 2.724;
gJex = 1.334 (* Excited state electron total angular momentum g-factor *);

```

```

In[88]:= (* Variation of excited state energy with magnetic field *)
ExState[Jt_, mJ_, It_, mI_, x_] := Ahfex mI mJ +
    Bhfex 
$$\frac{9 (mI mJ)^2 - 3 Jt (Jt + 1) mI^2 - 3 It (It + 1) mJ^2 + It (It + 1) Jt (Jt + 1)}{4 Jt (2 Jt - 1) (2 It - 1)} +$$

    uB (gJex mJ + gI mI) x;

```

References

- Aikawa, K., A. Frisch, M. Mark, S. Baier, A. Rietzler, R. Grimm, and F. Ferlaino (2012), Phys. Rev. Lett. **108**, 210401.
- Arimondo, E., M. Inguscio, and P. Violino (1977), Rev. Mod. Phys. **49**, 31.
- Aymar, M., and O. Dulieu (2005), J. Chem. Phys. **122** (204302), 204302.
- Azizi, S., M. Aymar, and O. Dulieu (2004), The European Physical Journal D - Atomic, Molecular, Optical and Plasma Physics **31** (2), 195.
- Bernath, P. F. (2005), *Spectra of Atoms and Molecules, 2nd Ed.* (Oxford Univ. Press).
- Bloch, I., J. Dalibard, and W. Zwerger (2008), Rev. Mod. Phys. **80**, 885.
- Brown, J. M., and A. Carrington (2003), *Rotational Spectroscopy of Diatomic Molecules* (Cambridge Univ. Press, Cambridge; New York).
- Bussery, B., Y. Achkar, and M. Aubert-Frécon (1987), Chem. Phys. **116**, 319.
- Campbell, W. C., T. V. Tscherbul, H.-I. Lu, E. Tsikata, R. V. Krems, and J. M. Doyle (2009), Phys. Rev. Lett. **102**, 013003.
- Chikkatur, A. P. (2002), *Colliding and Moving Bose-Einstein Condensates: Studies of Superfluidity and Optical Tweezers for Condensate Transport*, Ph.D. thesis (Massachusetts Institute of Technology).
- Chin, C. (2005), arXiv:cond-mat/0506313v2 .
- Chin, C., R. Grimm, P. Julienne, and E. Tiesinga (2010), Rev. Mod. Phys. **82**, 1225.
- Chotia, A., B. Neyenhuis, S. A. Moses, B. Yan, J. P. Covey, M. Foss-Feig, A. M. Rey, D. S. Jin, and J. Ye (2012), Phys. Rev. Lett. **108**, 080405.
- Christensen, C. A. (2011), *Ultracold Molecules from Ultracold Atoms: Interactions in Sodium and Lithium Gas*, Ph.D. thesis (Massachusetts Institute of Technology).
- Cubizolles, J., T. Bourdel, S. J. J. M. F. Kokkelmans, G. V. Shlyapnikov, and C. Salomon (2003), Phys. Rev. Lett. **91**, 240401.
- Cumby, T. D., R. A. Shewmon, M.-G. Hu, J. D. Perreault, and D. S. Jin (2013), Phys. Rev. A **87**, 012703.

- Dalibard, J., F. Gerbier, G. Juzeliūnas, and P. Öhberg (2011), *Rev. Mod. Phys.* **83**, 1523.
- Deh, B., W. Gunton, B. G. Klappauf, Z. Li, M. Semczuk, J. Van Dongen, and K. W. Madison (2010), *Phys. Rev. A* **82**, 020701.
- Deiglmayr, J., M. Repp, R. Wester, O. Dulieu, and M. Weidemuller (2011), *Phys. Chem. Chem. Phys.* **13**, 19101.
- DeMarco, B. (2001), *Quantum Behaviour of an Atomic Fermi Gas*, Ph.D. thesis (University of Colorado).
- Demtröder, W. (2005), *Molecular Physics* (Wiley-VCH, Weinheim).
- Derevianko, A., J. F. Babb, and A. Dalgarno (2001), *Phys. Rev. A* **63**, 052704.
- Derevianko, A., W. R. Johnson, M. S. Safronova, and J. F. Babb (1999), *Phys. Rev. Lett.* **82**, 3589.
- Deuretzbacher, F., K. Plassmeier, D. Pfannkuche, F. Werner, C. Ospelkaus, S. Ospelkaus, K. Sengstock, and K. Bongs (2008), *Phys. Rev. A* **77**, 032726.
- D’Incao, J. P., and B. D. Esry (2005), *Phys. Rev. Lett.* **94**, 213201.
- Dürr, S., T. Volz, and G. Rempe (2004), *Phys. Rev. A* **70**, 031601.
- Dutta, S., J. Lorenz, A. Altaf, D. S. Elliott, and Y. P. Chen (2014), *Phys. Rev. A* **89**, 020702.
- Gacesa, M., P. Pellegrini, and R. Côté (2008), *Phys. Rev. A* **78**, 010701.
- Gao, B. (2010), *Phys. Rev. Lett.* **105**, 263203.
- Gerton, J. M., C. A. Sackett, B. J. Frew, and R. G. Hulet (1999), *Phys. Rev. A* **59**, 1514.
- Greiner, M., C. A. Regal, and D. S. Jin (2003), *Nature* **426**, 537.
- Griffiths, D. J. (1999), *Introduction to Electrodynamics, Third Edition* (Prentice Hall, New Jersey).
- Hadzibabic, Z. (2003), *Studies of a Quantum Degenerate Fermionic Lithium Gas*, Ph.D. thesis (Massachusetts Institute of Technology).
- Hadzibabic, Z., C. A. Stan, K. Dieckmann, S. Gupta, M. W. Zwierlein, A. Görlitz, and W. Ketterle (2002), *Phys. Rev. Lett.* **88**, 160401.
- Heo, M.-S., T. T. Wang, C. A. Christensen, T. M. Rvachov, D. A. Cotta, J.-H. Choi, Y.-R. Lee, and W. Ketterle (2012), *Phys. Rev. A* **86**, 021602.
- Herbig, J., T. Kraemer, M. Mark, T. Weber, C. Chin, H.-C. Nägerl, and R. Grimm (2003), *Science* **301** (5639), 1510.
- Hodby, E., S. T. Thompson, C. A. Regal, M. Greiner, A. C. Wilson, D. S. Jin, E. A. Cornell, and C. E. Wieman (2005), *Phys. Rev. Lett.* **94**, 120402.

- Hudson, E. R., N. B. Gilfoy, S. Kotochigova, J. M. Sage, and D. DeMille (2008), Phys. Rev. Lett. **100**, 203201.
- Inouye, S., M. R. Andrews, J. Stenger, H.-J. Miesner, D. M. Stamper-Kurn, and W. Ketterle (1998), Nature **392**, 151.
- Israelachvili, J. N. (2011), *Intermolecular and Surface Forces, Third Edition* (Elsevier).
- Jo, G. B. (2010), *Quantum Coherence and Magnetism in Bosonic and Fermionic Gases of Ultracold Atoms*, Ph.D. thesis (Massachusetts Institute of Technology).
- Jochim, S., M. Bartenstein, A. Altmeyer, G. Hendl, S. Riedl, C. Chin, J. Hecker Denschlag, and R. Grimm (2003), Science **302** (5653), 2101.
- Jones, K. M., E. Tiesinga, P. D. Lett, and P. S. Julienne (2006), Rev. Mod. Phys. **78**, 483.
- Julienne, P. S., T. M. Hanna, and Z. Idziaszek (2011), Phys. Chem. Chem. Phys. **13**, 19114.
- Ketterle, W., and M. W. Zwierlein (2008), Riv. Nuovo Cimento **31**, 247.
- Köhler, T., K. Góral, and P. S. Julienne (2006), Rev. Mod. Phys. **78**, 1311.
- Krems, R. V., W. C. Stwalley, and B. Friedrich, Eds. (2009), *Cold Molecules: Theory, Experiment, Applications* (CRC Press, Boca Raton, FL).
- Lahaye, T., C. Menotti, L. Santos, M. Lewenstein, and T. Pfau (2009), Rep. Prog. Phys. **72** (12), 126401.
- Landau, L. D., and E. M. Lifshitz (1977), *Quantum Mechanics: Non-Relativistic Theory, Third Edition* (Elsevier Butterworth-Heinemann, Oxford).
- Lee, Y. R. (2012), *Ultracold Fermi Gas with Repulsive Interactions*, Ph.D. thesis (Massachusetts Institute of Technology).
- Lefebvre-Brion, H., and R. W. Field (2004), *The Spectra and Dynamics of Diatomic Molecules* (Elsevier, San Diego, CA).
- LeRoy, R. J., and R. B. Bernstein (1970), The Journal of Chemical Physics **52** (8), 3869.
- Lu, M., N. Q. Burdick, S. H. Youn, and B. L. Lev (2011), Phys. Rev. Lett. **107**, 190401.
- Mabrouk, N., and H. Berriche (2008), Journal of Physics B: Atomic, Molecular and Optical Physics **41** (15), 155101.
- Marzok, C., B. Deh, C. Zimmermann, P. W. Courteille, E. Tiemann, Y. V. Vanne, and A. Saenz (2009), Phys. Rev. A **79**, 012717.
- Mayle, M., G. Quéméner, B. P. Ruzic, and J. L. Bohn (2013), Phys. Rev. A **87**, 012709.
- Micheli, A., G. K. Brennen, and P. Zoller (2006), Nature Phys. **2**, 341.
- Mies, F. H., C. J. Williams, P. S. Julienne, and M. Krauss (1996), J. Res. Natl. Inst. Stand. Technol. **101**, 521.

- Mitroy, J., and M. W. J. Bromley (2003), *Phys. Rev. A* **68**, 052714.
- Mukaiyama, T., J. R. Abo-Shaeer, K. Xu, J. K. Chin, and W. Ketterle (2004), *Phys. Rev. Lett.* **92**, 180402.
- Musial, M., and S. A. Kucharski (2014), *Journal of Chemical Theory and Computation* **10** (3), 1200.
- Chwedeńczuk, J., K. Góral, T. Köhler, and P. S. Julienne (2004), *Phys. Rev. Lett.* **93**, 260403.
- Ni, K.-K. (2009), *A Quantum Gas of Polar Molecules*, Ph.D. thesis (University of Colorado).
- Ni, K.-K., S. Ospelkaus, M. H. G. de Miranda, A. Pe'er, B. Neyenhuis, J. J. Zirbel, S. Kotochigova, P. S. Julienne, D. S. Jin, and J. Ye (2008), *Science* **322** (5899), 231.
- Notz, P. M. (2014), *Development of Experimental Tools for Photoassociation Spectroscopy of Ultracold LiNa Molecules*, Master's thesis (Technische Universität Darmstadt).
- Ospelkaus, S., K.-K. Ni, D. Wang, M. H. G. de Miranda, B. Neyenhuis, G. Quéméner, P. S. Julienne, J. L. Bohn, D. S. Jin, and J. Ye (2010), *Science* **327** (5967), 853.
- Papp, S. B., and C. E. Wieman (2006), *Phys. Rev. Lett.* **97**, 180404.
- Pasquini, T. A. (2007), *Quantum Reflection of Bose-Einstein Condensates*, Ph.D. thesis (Massachusetts Institute of Technology).
- Petrov, D. S., C. Salomon, and G. V. Shlyapnikov (2004), *Phys. Rev. Lett.* **93**, 090404.
- Pillet, P., A. Crubellier, A. Bleton, O. Dulieu, P. Nosbaum, I. Mourachko, and F. Masnou-Seeuws (1997), *Journal of Physics B: Atomic, Molecular and Optical Physics* **30** (12), 2801.
- Quéméner, G. (2012), private communication .
- Quéméner, G., J. L. Bohn, A. Petrov, and S. Kotochigova (2011), *Phys. Rev. A* **84**, 062703.
- Quéméner, G., and P. S. Julienne (2012), *Chemical Reviews* **112** (9), 4949.
- Quéméner, G., J.-M. Launay, and P. Honvault (2007), *Phys. Rev. A* **75**, 050701.
- Regal, C. A., M. Greiner, and D. S. Jin (2004), *Phys. Rev. Lett.* **92**, 083201.
- Saffman, M., T. G. Walker, and K. Mølmer (2010), *Rev. Mod. Phys.* **82**, 2313.
- Schuster, T., R. Scelle, A. Trautmann, S. Knoop, M. K. Oberthaler, M. M. Haverhals, M. R. Goosen, S. J. J. M. F. Kokkelmans, and E. Tiemann (2012), *Phys. Rev. A* **85**, 042721.
- Shin, Y. I. (2006), *Experiments with Bose-Einstein Condensates in a Double-Well Potential*, Ph.D. thesis (Massachusetts Institute of Technology).
- Spiegelhalder, F. M., A. Trenkwalder, D. Naik, G. Kerner, E. Wille, G. Hendl, F. Schreck, and R. Grimm (2010), *Phys. Rev. A* **81**, 043637.

- Staanum, P., S. D. Kraft, J. Lange, R. Wester, and M. Weidemüller (2006), Phys. Rev. Lett. **96**, 023201.
- Stan, C. A., M. W. Zwierlein, C. H. Schunck, S. M. F. Raupach, and W. Ketterle (2004), Phys. Rev. Lett. **93**, 143001.
- Steck, D. A. (2010), *Quantum and Atom Optics* (available online at <http://steck.us/teaching>).
- Steinke, M., H. Knöckel, and E. Tiemann (2012), Phys. Rev. A **85**, 042720.
- Strecker, K. E., G. B. Partridge, and R. G. Hulet (2003), Phys. Rev. Lett. **91**, 080406.
- Syassen, N., T. Volz, S. Teichmann, S. Dürr, and G. Rempe (2006), Phys. Rev. A **74**, 062706.
- Thompson, S. T., E. Hodby, and C. E. Wieman (2005), Phys. Rev. Lett. **95**, 190404.
- Tiecke, T. G. (2009), *Feshbach resonances in ultracold mixtures of the fermionic quantum gases ^6Li and ^{40}K* , Ph.D. thesis (University of Amsterdam).
- Tiecke, T. G., M. R. Goosen, J. T. M. Walraven, and S. J. J. M. F. Kokkelmans (2010), Phys. Rev. A **82**, 042712.
- Tscherbul, T. V., Y. V. Suleimanov, V. Aquilanti, and R. V. Krems (2009), New J. Phys. **11**, 055021.
- Ulmanis, J., J. Deiglmayr, M. Repp, R. Wester, and M. Weidemüller (2012), Chemical Reviews **112** (9), 4890, pMID: 22931226, <http://dx.doi.org/10.1021/cr300215h>.
- Walraven, J. T. M. (2010), *Elements of Quantum Gases* (University of Amsterdam, available online at <http://staff.science.uva.nl/walraven/walraven/Education.htm>).
- Wang, T. T., M.-S. Heo, T. M. Rvachov, D. A. Cotta, and W. Ketterle (2013), Phys. Rev. Lett. **110**, 173203.
- Weimer, H., M. Müller, I. Lesanovsky, P. Zoller, and H. P. Büchler (2010), Nature Phys **6**, 382.
- Wille, E., F. M. Spiegelhalder, G. Kerner, D. Naik, A. Trenkwalder, G. Hendl, F. Schreck, R. Grimm, T. G. Tiecke, J. T. M. Walraven, S. J. J. M. F. Kokkelmans, E. Tiesinga, and P. S. Julienne (2008), Phys. Rev. Lett. **100**, 053201.
- Williams, J. E., N. Nygaard, and C. W. Clark (2006), New J. Phys. **8**, 150.
- Wu, C.-H., J. W. Park, P. Ahmadi, S. Will, and M. W. Zwierlein (2012), Phys. Rev. Lett. **109**, 085301.
- Wynar, R., R. S. Freeland, D. J. Han, C. Ryu, and D. J. Heinzen (2000), Science **287** (5455), 1016.

- Xu, K., T. Mukaiyama, J. R. Abo-Shaeer, J. K. Chin, D. E. Miller, and W. Ketterle (2003), Phys. Rev. Lett. **91**, 210402.
- Zahzam, N., T. Vogt, M. Mudrich, D. Comparat, and P. Pillet (2006), Phys. Rev. Lett. **96**, 023202.
- Zirbel, J. J. (2008), *Ultracold Fermionic Feshbach Molecules*, Ph.D. thesis (University of Colorado).
- Zirbel, J. J., K.-K. Ni, S. Ospelkaus, J. P. D’Incao, C. E. Wieman, J. Ye, and D. S. Jin (2008a), Phys. Rev. Lett. **100**, 143201.
- Zirbel, J. J., K.-K. Ni, S. Ospelkaus, T. L. Nicholson, M. L. Olsen, P. S. Julienne, C. E. Wieman, J. Ye, and D. S. Jin (2008b), Phys. Rev. A **78**, 013416.